Deliverable D5.7: Final technical report on redox reactivity of radionuclides on mineral surfaces

Work Package WP5-FUTURE

The project leading to this application has received funding from the European Union's Horizon 2020 research and innovation programme under grant agreement No 847593.

http://www.ejp-eurad.eu/

EURAD Deliverable D5.7 – Final technical report on redox reactivity of radionuclides on mineral surfaces.

Document information

Project Acronym	**EURAD**
Project Title	**European Joint Programme on Radioactive Waste Management**
Project Type	**European Joint Programme (EJP)**
EC grant agreement No.	**847593**
Project starting / end date	**1st June 2019 – 30 May 2024**
Work Package No.	**WP5**
Work Package Title	**Fundamental understanding of radionuclide retention**
Work Package Acronym	**FUTURE**
Deliverable No.	**D5.7**
Deliverable Title	Final technical report on redox reactivity of radionuclides on mineral surfaces
Lead Beneficiary	**BRGM**
Contractual Delivery Date	**December 2023**
Actual Delivery Date	
Type	
Dissemination level	
Authors	**Sylvain Grangeon, Maria Marques, Ursula Alonso de los Ríos, Laurent Charlet, Sergey Churakov, Maria Crina Bucur, Romain Dagnelie, Ana María Fernandez, Horst Geckeis, Jasper Griffioen, Miguel García Gutiérrez, Alwina Hoving, Francisco Javier Leon, Tiziana Missana, Augusto Oliveira, Mirela Olteanu, Agnieszka Poulain, Yanting Qian, Jean-Charles Robinet, Sébastien Savoye, Bianca Schacherl, Andreas Scheinost, Christophe Tournassat, Tonya Vitova**

To be cited as:

Grangeon S., Marques, M., Alonso de los Ríos U., Charlet L., S. Churakov, Bucur M.-C., Dagnelie R., Fernandez A.-M., Geckeis H., Griffioen J., García Gutiérrez M., Hoving A., Javier Leon F., Missana T., Oliveira A., Olteanu M., Poulain A., Qian Y., Robinet J.-C., Savoye S., Schacherl B., Scheinost A., Tournassat C., Vitova T. (2024): Final technical report on redox reactivity of radionuclides on mineral surfaces. Final version as of 08.02.2024 of deliverable D5.7 of the HORIZON 2020 project EURAD. EC Grant agreement no: 847593.

Disclaimer

Acknowledgement

This document is a deliverable of the European Joint Programme on Radioactive Waste Management (EURAD). EURAD has received funding from the European Union's Horizon 2020 research and innovation programme under grant agreement No 847593.

Status of deliverable		
	By	Date
Delivered (Lead Beneficiary)	Sylvain Grangeon (Andra/BRGM) Maria Marques (PSI)	11.12.2023
Verified (WP Leader)	Sergey Churakov (PSI)	17.01.2024
Reviewed (Reviewers)	Rainer Dähn	19.01.2024
Approved (PMO)	Bernd Grambow	19.02.2024
Submitted to EC	Andra (Coordinator)	20.02.2024

Executive Summary

Quantification of redox processes is one of the most challenging tasks in WP FUTURE from methodological and modelling points of view.

This document summarizes and compiles the main results that were obtained in the frame of the Eurad project with regards to the synthesis of Fe-bearing minerals of interest for radwaste storage, their morphological, mineralogical, and crystallographic characterization, as well as the characterization of clay-rocks, and of the study of their reactivity towards redox-sensitive elements.

Thanks to intensive collaboration between partners, major scientific advances were obtained in the frame of this project, including synchrotron beamline upgrades or developments and ground-breaking scientific results. In particular:

- Instrumental developments at CAT-ACT (KIT light source) and at the Rossendorf (BM20 at ESRF) beamlines, which enabled improved resolution for the detection and speciation of chemical elements, e.g., Np, and thus the investigation of (redox) phenomena under conditions (dilute systems) that are relevant for in situ conditions.
- Reliable protocols and synthesis methods have been developed or improved to produce or condition clays (nontronite) and iron oxides (magnetite, goethite, green rust) with controlled properties, such as the size, density of structural defects, or Fe content and Fe(II)/Fe(III) ratio. In addition, (electro)chemical protocols have been developed and applied to quantitatively monitor changes in the redox state of Fe in solids. These solid samples were subsequently characterized, and several samples were shared with the partners involved and used for further sorption experiments. In addition, samples of clay rocks were shared for characterization and use in sorption experiments.
- Sorption experiments involving redox-sensitive elements relevant for radioactive waste disposal (Se, Np, U, Tc – and Re used as analogies in some studies) and the relevant minerals described above (Fe-poor and Fe-rich clays, iron oxides, green rust) were successfully conducted. The detailed results are described in the main part of the experimental report, and only two major examples discussed in the summary. The first example is Se: when interacting with clay minerals, no Se(IV) reduction is observed, when it is contacted with a sample that does not contain redox-active Fe(II). In the presence of redox-active Fe, Se(IV) is reduced to Se(0), with the nature of the product (grey or red Se(0)) being kinetically controlled. The effects of chemical conditions (e.g., pH) could also be quantified. Upon contact with Fe oxides (magnetite and green rust with Cl interlayer), Se reduction to Se(0) is also observed, with pH playing an important role. The second example is Tc/Re: It was also observed that structural redox-active Fe(II) is necessary for the reduction and that the adsorption of Fe(II) on clay minerals further enhances the reduction. The effects of chemical conditions (pH, oxic or anoxic, presence of reducing agents) on sorption and reaction kinetics could also be quantified. Theoretical quantum mechanical calculations were used to investigate and determine the nature of the reaction product.
- The interaction of redox-sensitive elements with mineralogical assemblages (dispersed or compacted) and with compacted clay rock was investigated. Thus, it was possible, for example, to analyse the diffusion of U(VI) in an intact, compacted, Callovian-Oxfordian sample for ~600 d and to both determine a retention coefficient and investigate redox disequilibria due to U complexation with carbonates.

In summary, and in line with the original objectives of this task, significant new insights have been gained with respect to the quantitative and mechanistic understanding of the sorption of redox-sensitive elements by Fe-containing minerals, which can for example be present in the pristine clay rock (e.g., Fe phyllosilicates), or neoformed due to corrosion or oxidation processes (e.g., magnetite, green rust). This achievement benefited from extensive exchanges between partners (e.g., informal collaborations, shared PhD students, sharing of samples, Eurad mobility program).

Table of content

List of figures

List of Tables

1. Context, aims, relation to existing literature [**All groups**]

A sound understanding of the retention mechanisms of chemical species by mineral surfaces is a fundamental prerequisite for quantifying, modelling, and ultimately predicting the migration of solutes in geological media. “Sorption” is an ill-defined term that lumps a variety of different molecular-scale phenomena, including reversible and irreversible processes. Reversible phenomena, termed as adsorption, implies the solid phase is not modified when the species is sorbed, and that when the species return to the solution, its speciation remains unchanged. One example of an adsorption mechanism is cation sorption in clay interlayer, through cation exchange mechanism. In contrast, irreversible phenomena lead to modifications of the solid and (or) of the speciation of the adsorbed elements. Examples of irreversible mechanisms are recrystallization, epitaxial growth at mineral surfaces, or heterogeneous redox reaction – hereafter referred to as “redox reactions”.

Surface induced redox reactions are defined by electron transfer between the solid phase and the sorbed element. Therefore, both the chemical speciation of the element and the nature of the solid phase (e.g., its permanent structural charge) are modified. Such reaction can have antagonistic effects concerning element solubility and (or) mobility, depending on the element considered. For example, chromium has lower solubility when present as Cr(III), while it is much more soluble as Cr(VI). Hence a redox reaction that would lead to reduction of Cr(VI) to Cr(III) would slow down its migration due to a decrease in aqueous Cr concentration. Migration can also be influenced by a change in the affinity of the element for the solid phase. For example, As(V) has a much higher affinity for iron oxides than As(III). For a redox reaction to occur with a redox-sensitive element, the solid must have the ability to readily exchange electrons.

In the context of deep geological storage, the probably most important type of minerals capable of participating in heterogeneous redox reactions are probably iron bearing minerals. This includes iron-containing phyllosilicates (either naturally present in the geological formation or neo-formed *in situ*), iron oxides (e.g., magnetite, which can for example form during canister corrosion), and green rust (corrosion product formed in anoxic conditions). Determining their potential influence on the sorption, speciation, and hence mobility requires a sound multi-scale understanding of its structure, of the link between structure, proportion of redox-active iron to total iron, and sorption mechanisms. It also requires quantifying the reactivity of synthetic and natural rocks containing these phases.

The present report, which is built from the contributions of all participants to the “redox” task of the Eurad/Future work package, aims at providing new insights into the redox reactions occurring between redox-sensitive elements and iron-containing minerals of relevance to geological disposal. For this purpose, a multi-scale and multi-technique work plan was adopted and is schematized in Figure 1.

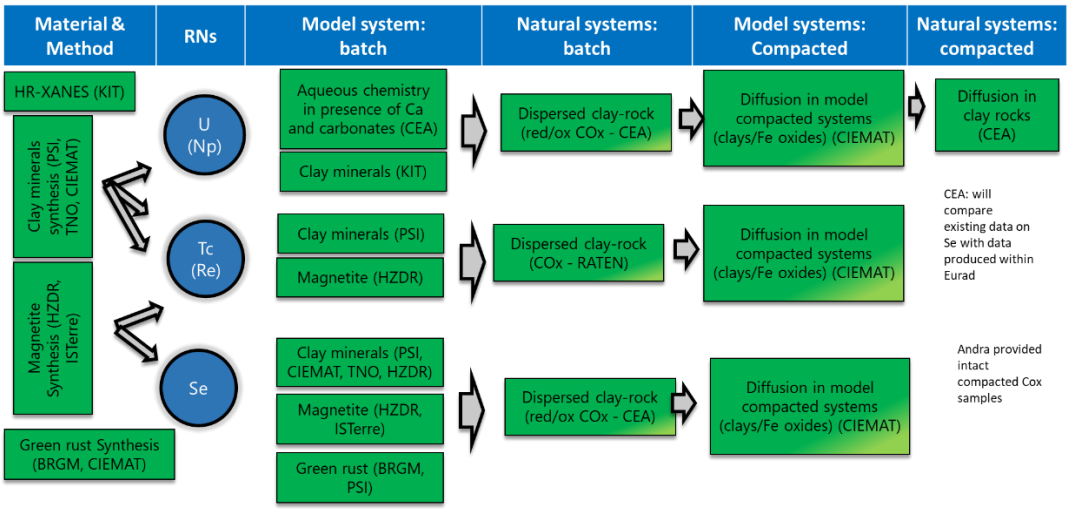

Figure 1. Scheme of the work plan adopted in the presently discussed task of the Eurad program.

Briefly, analytical methods were applied or developed, to produce a variety of samples ranging from pure minerals with well-controlled structure and sufficient structural variation [e.g., Fe(II)/Fe(III) ratio] within a given mineral group to mineral assemblages to compacted rock samples. The exact structure of the solids was characterized with several state-of-the-art techniques, including but not limited to wet chemistry, X-ray scattering, electron microscopy, Mossbauer and XPS spectrometry, electrochemical methods. In parallel, new developments made on synchrotron beamlines allowed for an improved capacity to detect and quantify trace elements speciation at high dilutions. These solids and methods were then used to study their reactivity towards radioelements (or their stable analogues) sorption, including determination of the mechanism of interaction, speciation change (both element of interest and of Fe), and nature of the reaction product. With regards to this latter point, DFT methods provided new insights into the nature of Tc nanoparticulate phases. To check for the relative role played by the different mineral phases of interest for this project, and to reach mineralogical conditions closer to real-site conditions, sorption was then tested on dispersed systems made of an assemblage of several phases. In a third step, and still with the aim of approaching real site conditions, sorption was tested on compacted samples, and element diffusion within actual clay-rocks was also studied.

2. Materials [All groups]

The selection of materials was intended to promote redox processes in radionuclides, mainly favoured by the Fe(III)/Fe(II) pair, present in different fractions: (a) in clay structure, (b) as accessory mineral in clays, (c) as iron oxides (from steel canister corrosion). Natural clays with Fe(II)/Fe(II) content (i.e., nontronites) have been selected and additionally, clay samples have been synthesized in the laboratory, to tune and control the Fe content in both oxidation states, from ferric to ferrous. Iron oxides with different sorption and redox properties were synthetized and fully characterised. Natural clay rocks, representative of repository host rocks in different countries has been also considered. In this part, extensive experimental characterization work was performed on the materials, as fundamental support for radionuclide retention assays and modelling tasks.

2.1 Reference mono-mineral samples/materials

2.1.1 Nontronite [PSI, BRGM, CIEMAT]

2.1.1.1 Purification and tuning of natural nontronite (NAu-1 and NAu-2) properties [PSI, BRGM, CIEMAT]

[CIEMAT] carried out three specific purification and tuning procedures to natural smectites to evaluate the role of Fe location on the overall radionuclide retention in smectite clays: (i) Obtaining of ferrous and ferric nontronite fractions, (ii) synthesis of Fe(II/III) nontronites, (iii) Treatment of smectite clays to eliminate accessory Fe mineral and oxides.

For these purposes, [CIEMAT] selected NAu-1 and NAu-2 nontronite samples, were acquired from the Clay Mineral Society (CMS) Source Clay Repository. Bulk samples of NAu-1 and NAu-2 nontronites correspond to bright-green clay (Munsell colour 5GY6/6) and dark-brown clay (Munsell colour 10YR2/1), respectively. They were collected from the Uley graphite mine, South Australia (Keeling et al., 1980). NAu-1 clay samples for CMS were collected from the pit floor in kaolinized schist in the central area of the open cut. NAu-2 was collected from weathered amphibolite exposed near the base of the eastern pit wall in a 3-m deep drain excavated at the perimeter of the pit floor. These clay minerals, and other iron oxide minerals, were originated from the weathering of the silicate minerals from the crystalline basement rocks (prior to Middle Eocene times).

Complete characterisation of all clay fractions was carried out by different techniques. The structure of natural, purified, and treated clay fractions was characterized by XRD, Far-, Mid-IR, TEM, BET, XPS and Mössbauer techniques. Physical-chemical properties, such as BET and CEC were also determined on all clay fractions, to better describe their sorption behaviour.

The mineralogy of both raw samples is shown in Table 1. NAu-1 sample has a 97 wt.% of phyllosilicates (88 % nontronite and 9 % kaolinite), whereas NAu-2 has 95 wt.% of phyllosilicates (100% of nontronite

clay mineral type). The chemical analyses of main oxides and trace elements from the bulk material determined by XRF are shown in

Table 2, whereas the main physico-chemical properties can be found in Table 3. Raw NAu clays are mainly di-octahedral calcium-magnesium nontronites (Table 4). SEM analyses revealed that apart from nontronite clay mineral, NAu-1 sample contains kaolinite, Fe-oxy(hydroxides) and graphite flakes (Figure 2); whereas in NAu-2, nontronite is the only clay mineral (Figure 3), and contains remnants of primary minerals (feldspars), and a higher amount of Fe-oxy(hydroxides), such as goethite. This is reflected in the structural formula of the nontronites, in which NAu-1 contains more aluminium than silica at octahedral sites, and less iron (

Table 2). In the ideal structural formula for nontronite, the octahedral cations consist entirely of Fe^{3+} ions, with the layer charge arising from Al^{3+} for Si^{4+} in the tetrahedral sheet. As any dioctahedral smectite, Mg^{2+} substitution in the octahedral sheet occurs. The layer charge of NAu-1 is higher than of NAu-2.

Table 1. Mineral content (in wt.%) of the samples obtained from XRD.

Samples	Total Phyllosilicates	Quartz	K-Feldspar	Plagioclase	Calcite	Goethite	Biotite	Cristobalite
NAu-1	97(*)	1	Tz	--	1	Tz	Tz	--
NAu-2	95(**)	1	--	1	1	2	Tz	Tz

(*) Tot. Phyllosilicates: 88% nontronite, 9% kaolinite; (**) Tot. Phyllosilicates: 100% nontronite

Table 2. Chemical composition of the main oxides in the total fraction (in wt.%, ignited at 1050°C).

Samples	SiO_2	Al_2O_3	Fe_2O_3	MnO	MgO	CaO	Na_2O	K_2O	TiO_2	P_2O_5	SrO	BaO	SO_2
NAu-1	48.89	10.87	36.94	0.05	0.93	1.63	0.16	0.16	0.27	0.04	0.01	0.01	0.01
NAu-2	56.08	2.91	37.39	<d.l.	0.98	1.56	0.62	0.09	0.33	0.02	0.01	<d.l.	0.01

Table 3. Main properties of the raw NAu-1 and NAu-2 nontronites

Sample	CEC(meq/100g) (*)	BET / Total External SA(m^2/g)(**)	TOTAL SA(m^2/g)
NAu-1	85 ± 1	58 / 63	729 ± 4
NAu-2	82 ± 3	44 / 47	541 ± 2

(*) CEC: measured with 0.01 M copper triethylenetetramine (Cu-Trien or $[Cu(trien)]^{2+}$ solution (Amman et al., 2005);
(**) BET external surface area: from N_2 adsorption isotherms according to the BET method (Brunauer et al., 1938; Gregg and Sing, 1982); Total External SA: t-plot treatment of the N_2 adsorption branch (de Boer et al., 1966); Total surface charge (SA): *w*ater vapour gravimetric adsorption measurements at a constant 75% relative humidity atmosphere (Keeling et al., 1980).

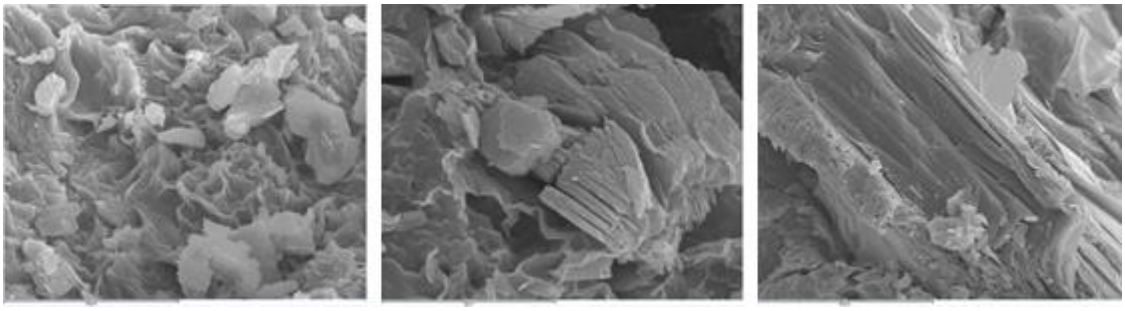

Figure 2. SEM photomicrographs of the NAu-1 sample; a) nontronite clay particles; b) kaolinite clay particles; c) graphite flakes.

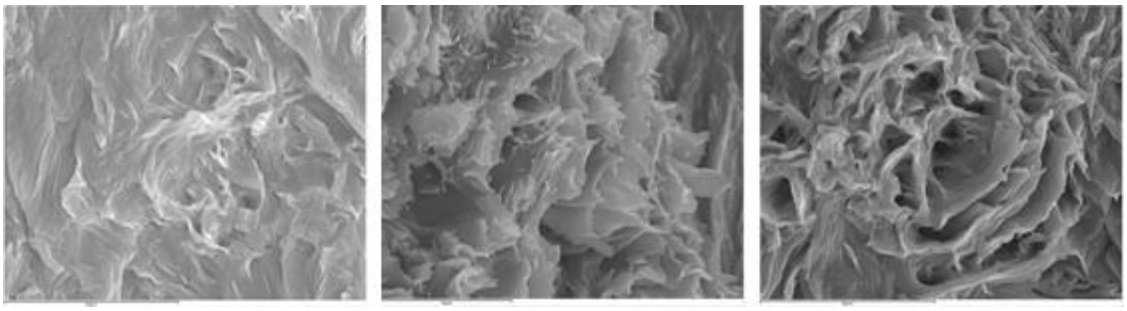

Figure 3. SEM photomicrographs of the NAu-2 sample; clay mineral structure of nontronite.

Table 4. Cation exchange occupancies of the raw NAu-1 and NAu-2 clays and the ferric Fe(III)-NAu-2 sample which was reduced.

Sample	Na	K	Mg	Ca	Sr	Ba	Σcations
	(meq/100g)						
NAu-1	0.78 ±0.03	1.18 ±0.04	30.82 ±1.66	50.52 ±0.06	0.140 ±0.02	0.005 ±0.001	83.5 ±1.8
NAu-2	0.90 ±0.01	0.43 ±0.02	27.73 ±0.52	43.18 ±0.94	0.13 ±0.01	0.004 ±0.001	72.4 ±1.4
Ferric-NAu-2	28.72	0.38	14.92	26.62	0.06	0.003	70.7

Still at CIEMAT, NAu-2 samples were selected for purification procedures, to obtain ferrous and ferric nontronite fractions, and for sorption tests, because NAu-1 nontronite contained kaolinite.

Ferric nontronite: Raw NAu-2 nontronite was conditioned to produce two clay batches with different Fe(II)/Fe(III) ratios. Nontronite clay particles, < 0.2 µm size fraction, were separated by sedimentation in 1 L water column, after ultrasonic dispersion in deionized water. Afterwards, the clay suspension was successively treated with a sodium acetate buffer (NaOAc 1N) at pH 5.0 to remove carbonates, and then with a dithionite-citrate-bicarbonate solution (DCB method) to remove mineral impurities, such as Fe-oxi(hydroxides). The final suspensions were washed six times with a 50:50 mixture of deionized water and ethanol as described in (Jackson, 2005). The solid phase was separated by centrifugation for 1 hour at 15000 rpm, air dried during several days and homogenized by using an agate mortar. This batch was referenced as Ferric-NAu2 nontronite and fully characterized.

This Ferric-NAu2 nontronite was used for ^{75}Se(IV), ^{233}U(VI) and ^{99}Tc(VII) sorption experiments, whereas another portion was used for obtaining reduced ferrous-NAu2 nontronite as follows.

Ferrous nontronite: Part of the ferric-NAu2 nontronite (~60 g) was reduced applying the method citrate bicarbonate dithionite method (Stucki et al., 1984). The level of reduction was controlled by varying the amount of sodium dithionite ($Na_2S_2O_4$) in the range of 0–3 g per 40 mg of clay, or by altering the reaction time within a span of 0–240 min. In the end, for complete reduction of all structural Fe, the amount of sodium dithionite was three times the mass of the clay mineral (1.5 g of dithionite per 0.5 g clay).

The procedure for clay reduction was the following:

1. 500 mg was added to a centrifuge tube of 60 mL.
2. The sample was mixed with 25 mL of the citrate-bicarbonate buffer and diluted with 40 mL of deionized water; the suspension being stirred overnight.
1. The temperature was brought to 75 °C in a water bath.
2. Sodium dithionite was slowly added to the mixture and stirred at the same temperature.
3. After the digestion period, the solid was washed three times with deoxygenated solution $5 \cdot 10^{-3}$ M NaCl followed by two washes with deoxygenated/deionized water for removing the excess of solutes from the sample.
4. The supernatant solution of each washing was collected into a separate 50 mL polyethylene bottle and Fe, Si, Al and Na were analysed.

5. Reduced solid was air-dried in the anoxic glove box (N_2, O_2< 0.1 ppm), and pulverized for measurements. The state of oxidation of the solid was determined with the phenanthroline spectroscopic method and by Mössbauer spectroscopy.
6. The reduced solid sample was analysed: CEC, IR, TG-DSC.

The characteristics of the Fe(III)- and Fe(II)-NAu2 samples can be seen in Figure 2 (XRD), Figure 5 (FTIR) and Figure 6, as well as in Table 4 and Table 5.

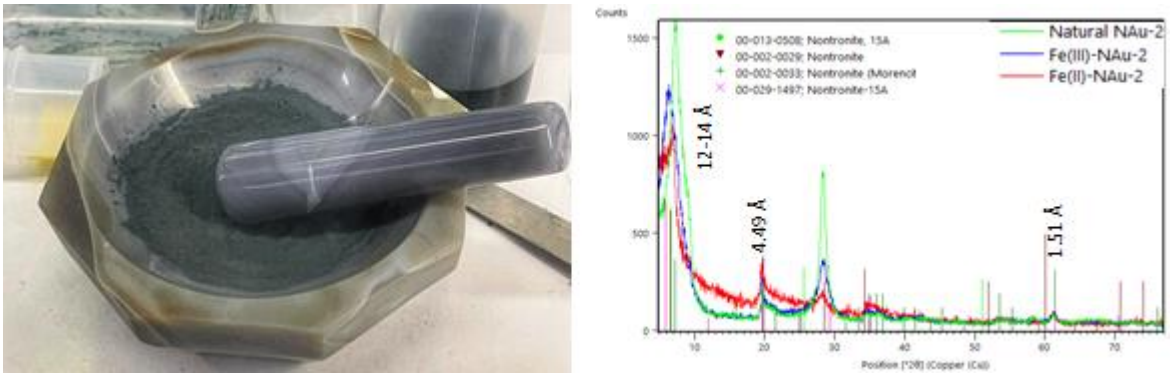

Figure 4. a) Photograph of the reduced Ferrous-NAu-2 sample, b) X-ray Diffraction patterns of the natural, ferric and ferrous NAu-2 samples

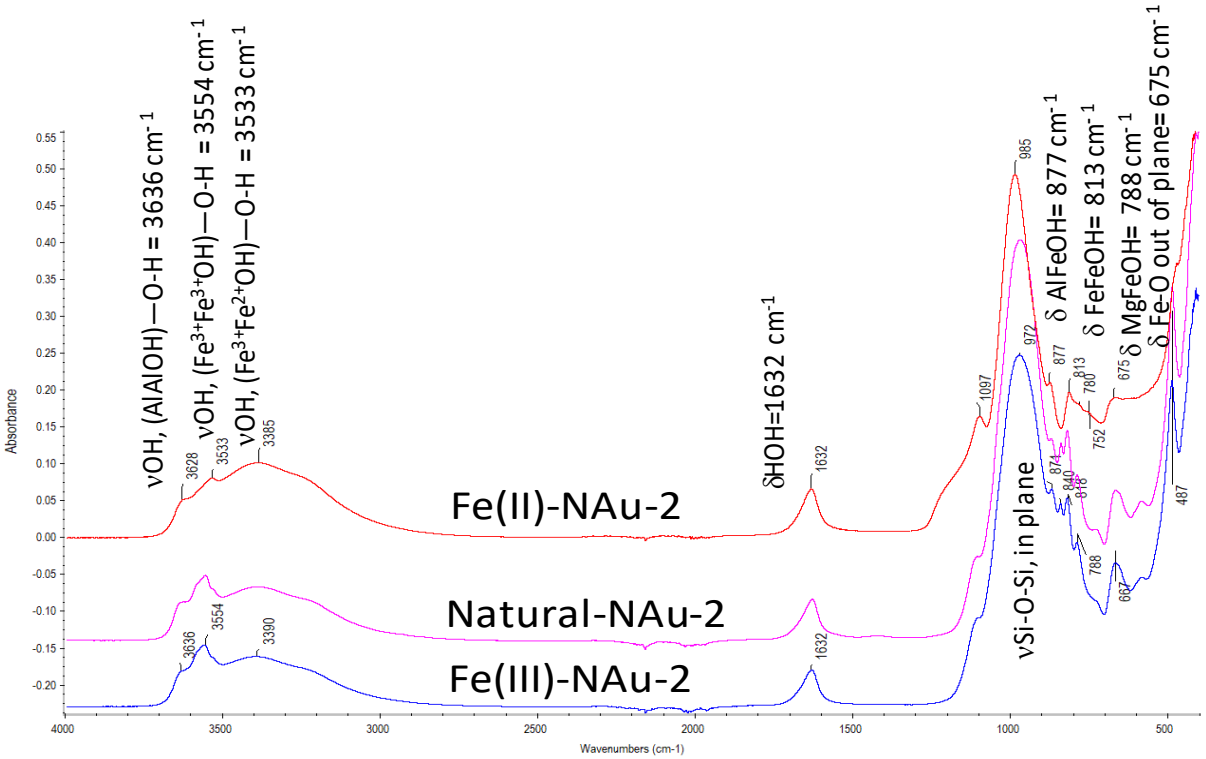

Figure 5. FTIR spectra of the natural, ferric and ferrous NAu-2 samples

Table 5. Physicochemical characterization of natural, Fe(III)-Nau-2 and Fe(II)-Nau-2 samples

Sample	BET specific surface (m^2/g)	CEC (meq/100g)
Natural Nontronite NAu-2	44 ± 0.3	77.3
Ferric-NAu-2	67 ± 0.5	76.5(*)
Ferrous-NAu-2	275 ± 0.3	75.7

(*) *See cation exchange occupancies in Table 4*.

The amount of Fe(III) and Fe(II) in the ferric- and ferrous-NAu-2 samples was obtained via NH_4HF_2-H_2SO_4 leaching tests from the samples, by using a modification of the procedure described in (Tarafder and Thakur, 2013) and analysed by 1,10 phenanthroline spectrophotometric method.

In addition, Mössbauer spectroscopy was also used to characterize iron compounds. ^{57}Fe Mössbauer spectroscopy data were recorded at room temperature (300 K) and at 8.5 K in transmission mode using a conventional constant acceleration spectrometer and a ^{57}Co (Rh) source. Absorbers were prepared to have an effective thickness of about 5-10 mg of natural iron per square centimetre. The velocity scale was calibrated using a 6 μm thick natural iron foil. All the spectra were computer-fitted using Lorentzian lines and the isomer shifts were referred to the centroid of the α-Fe sextet at room temperature. The spectra are shown in Figure 6.

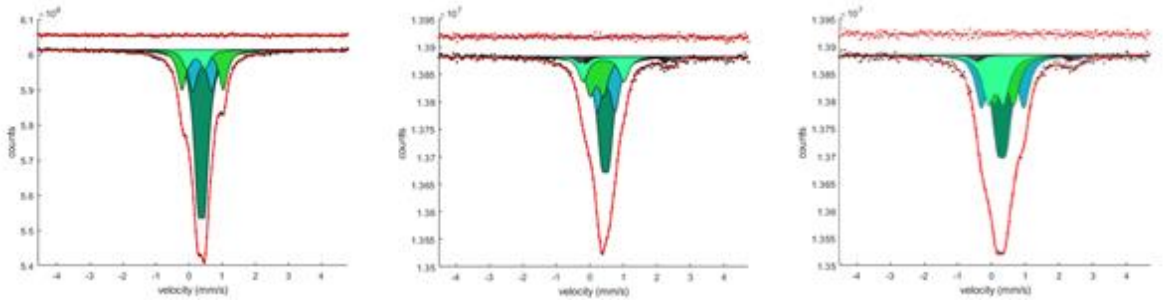

Figure 6. a) Mössbauer spectra of ferric NAu-2 nontronite at 298 K, b) Mössbauer spectra of ferrous NAu-2 nontronite at 298 K, c) Mössbauer spectra of ferrous NAu-2 nontronite at 8.5 K

2.1.1.2 Synthesis of nontronite and tuning of their properties [CIEMAT, BRGM]

[CIEMAT] synthesized Fe(III)-nontronites following the procedure described in (Decarreau et al., 2008) , under oxidizing conditions. The initial step was the co-precipitation of a starting silico-metallic gel by the mixing of solutions of sodium silicate and ferrous chloride in acidic medium (0.1 M $SiNa_2O_3$, 0.3 M $Fe(II)Cl_2$, 1 M HCl), having a Si/Fe ratio of 4:3 (trioctahedral smectites). Dioctahedral smectites were also obtained by using 4:2 Si/Fe ratios by working with 0.2 M ferrous or ferric chloride The pH of the suspension during co-precipitation was around 12.5 at 25°C. After precipitation, the starting gel was collected by centrifugation and slightly washed with Milli-Q® pure water (18 MΩ·cm). The starting gel was then oxidized during air drying before being crushed. Then, 500 mg of the powdered starting gel was placed in contact with 30 mL of NaOH 0.01M solutions at fixed pH of 12, 12.5 or 13 at 25°C in Teflon® metallic-coated hydrothermal reactors (Parr®, reactor number: 4744). The solutions were obtained from various dilutions of Normadose 1 M (NaOH).

Synthesis of Fe(III)-nontronites were performed at 150°C under equilibrium vapour pressure for 3 to 30 days. The temperature was chosen to obtain a better crystallinity of the synthesized nontronites without any crystallization of aegirine, according to (Mehra and Jackson, 1958). The synthesized solid phase was removed from the suspension at the end of the synthesis by centrifugation (15000 rpm for 30 minutes), washed with deionized water by centrifugation and air-dried.

The pH of the starting solutions (pH`s) and of the solutions at the end of synthesis (pH_f) was measured at 25°C using the Orion pH meter calibrated with three buffer solutions. The final aqueous phases were analysed for Si, Fe and Na.

X-ray diffraction patterns of different synthesized ferric nontronites can be seen in Figure 7 and the comparison with reference nontronites can be seen in Figure 8. The final pH of the solutions decreased from the pH of the starting solutions due to the consumption of OH^- groups by the crystallization of hydroxylated 2:1 layers. Figure 7b shows XRD patterns of powdered synthesized samples exhibit reflections at 12.53Å (001), 4.57 Å (02-11), 3.15 Å (004), 2.61 Å (13-20) and 1.536 Å (060),

corresponding to nontronite. Aegirine precipitated in addition to nontronite at starting solutions above pH 12.5, with aegirine reflections at 6.41 Å (110), 2.98 Å (121) and 2.53 Å (031), (Figure 7b).

Fe(II)-nontronites were obtained following the same procedure listed above. However, all the steps were performed inside an anoxic glove box, except for centrifugation. The synthesis at anoxic conditions began with the formation of a silicometallic gel due the mixing of solutions of sodium silicate and ferrous chloride. 500 mg of the powered starting gel was placed in contact with 30 mL of deionized water inside an anoxic glove box. The starting pH was adjusted to 12 by adding drops of 1M NaOH at 25°C in a Teflon® metallic-coated hydrothermal reactors (Parr®). Synthesis of Fe(II)-rich smectites were performed at 150°C under equilibrium pressure between 3 and 30 days. At the end of the synthesis, the synthesized solid phase was treated inside an anoxic glove box (Figure 9), and the suspension was removed by centrifugation, the solid phase being dried inside the anoxic glove box.

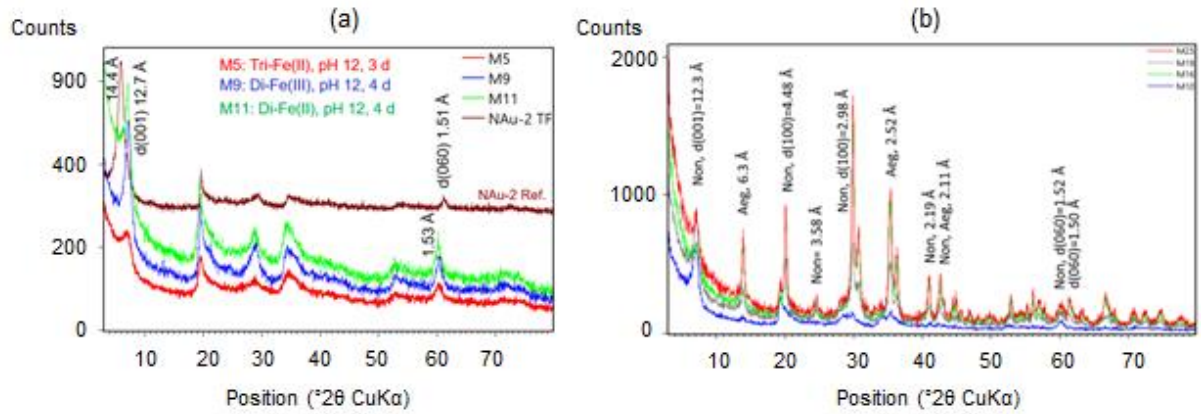

Figure 7. X-ray diffraction patterns of different synthetized nontronites at 150 °C: a) during 4 days at a starting pH of 12; and b) during 30 days at a starting pH of 12.5.

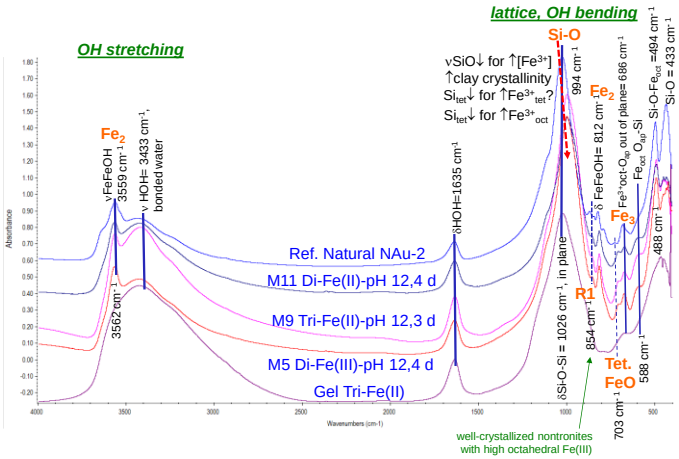

Figure 8. FTIR spectra of synthetized Fe(III)-nontronite and its comparison with reference nontronite NAu2.

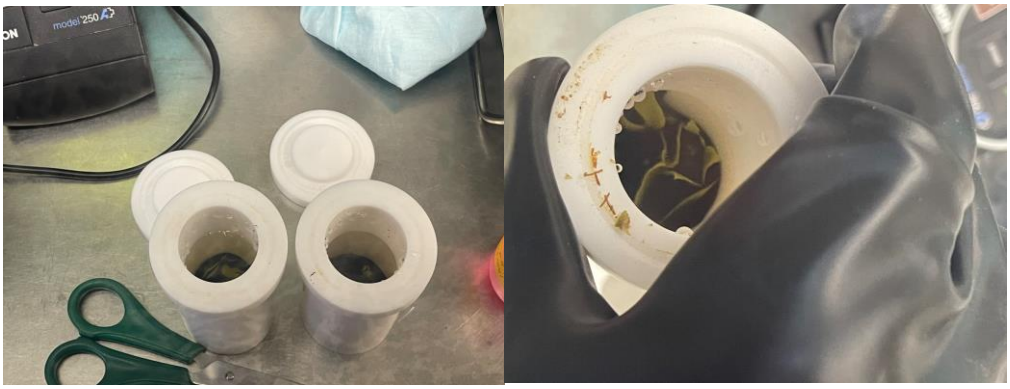

Figure 9. Ferrous smectites at 150 °C and starting pH of 12 synthetized during; a) 4 days; and b) during 30 days.

2.1.1.3 Treatment of smectite clays to eliminate Fe accessory minerals [CIEMAT]

To analyse the role of accessory Fe minerals, naturally present in clays, on the retention of redox sensitive radionuclides, [CIEMAT] obtained *Fe-oxide free* clay fractions, from NAu-1 (Jackson, 2005) and FEBEX raw clay, a Ca-Mg bentonite with high smectite content, from Cortijo de Archidona, Spain (Fernández and Villar, 2010; Huertas et al., 2000),following the methodology described in (Mehra and Jackson, 1958), using dithionite to eliminate the accessory Fe-oxides, mainly goethite and biotite (Table 1). The clay fractions treated with dithionite are noted as *Fe-oxide-free-NAu-1* and *Fe-oxide-free-FEBEX*. The procedure converts clays in Na-form and eliminating Fe-oxides. These Fe-oxide-free clay fractions were used for ^{233}U(VI) sorption experiments, whose sorption was compared to that of corresponding raw or Na-homo-ionic fractions. More details can be found in (Alonso et al., In preparation)

[BRGM] Nontronites prepared by BRGM were NAu-1 and NAu-2 clays obtained from the clay mineral society. They were purified by using an elutriation technique to obtain X-ray diffraction pure nontronite, having a size < 2 µm. They were then Na-saturated by 3 successive washings with a 1 M NaCl solution. Nontronites samples were characterized for total element content by electron probe microanalyzer, for Fe oxidation state with Mossbauer spectrometry and X-ray photoemission spectroscopy, and for morphology with TEM. The purified and characterised samples were sent to different partners for use in their sorption studied.

2.1.2 Other phyllosilicates [TNO]

2.1.2.1 Use of mediated electrochemistry to modify Fe(II)/Fe(III) and analyse the (absence of) relation between total Fe and redox-active Fe [TNO]

Several different types of clay minerals were acquired to investigate their redox-active Fe content. The clay mineral standards originated from the Clay Minerals Society, Ward's Natural Science Establishment, and the mineral collection at Utrecht University: chlorites (CCa-1 and a thuringite from Santa Ana, New-Mexico, USA), glauconite (Rarecourt, France), interstratified mixed-layered illite-smectites (ISCz-1, ISMt-1, RAr-1, Fithian illite) and an illite (IMt-1). The clay minerals were first purified to obtain a homogeneous Na-form with a particle size <0.5 µm (following the same protocol as PSI). Subsamples of these purified clay minerals were reduced using the Citrate-Bicarbonate-Dithionite (CBD) method (Stucki et al., 1984), and for RAR-1 and ISCz-1 also by mediated electrochemical reduction. For the latter, an electrochemical set-up was used at an applied redox potential of -0.38 V vs SHE using Zwitterionic Viologen as mediator to facilitate electron transfer between the electrode and clay mineral (description of the set-up and general idea of mediated electrochemistry applied to clay minerals can be found in (Gorski et al., 2012a; Gorski et al., 2012b)).

The total Fe content and Fe(II) content of the purified clay minerals, in their original redox state and in the reduced states, were analysed using the HF-phenanthroline method (Amonette and Charles Templeton, 1998). Redox-active Fe was investigated by measuring the electron donating and accepting

capacities (EDC and EAC) during mediated electrochemical oxidation and reduction (MEO/MER) (Gorski et al., 2012). These measurements were performed at different applied redox potentials (-0.6 V, -0.38 V,-0.18 V, 0.09 V and 0.6 V) in an electrolyte of 0.1 M NaCl buffered to pH=7 using MOPS (see details of this method in (Gorski et al., 2012a; Gorski et al., 2012b; Gorski et al., 2013)). In addition to the clay minerals mentioned in the previous paragraph, purified samples NAu-2, SWy-1 and STx-1 (native and reduced) were also analysed.

Results from MEO (+0.6V) and MER (-0.6V) showed that there was a linear relation between smectite content and redox-active Fe, with the higher the smectite content the higher the percentage of redox-active Fe (Figure 10 and Figure 11). In SWy-1 and STx-1smectites, 100% of the Fe was redox-active, in nontronite NAu-2 (native, low-red and high-red), 70-80% of total Fe was redox-active, while in the illite IMt-1 only 10% of total Fe was redox-active. The interstratified mixed-layered illite-smectites had redox-active Fe ratios in between the two endmembers (Figure 10 and Figure 11). In glauconite, only 5% of total Fe content was redox-active and in chlorite only 0.5-2%. These outcomes and results from similar measurements were used to interpret some of the results observed in batch experiments with selenite.

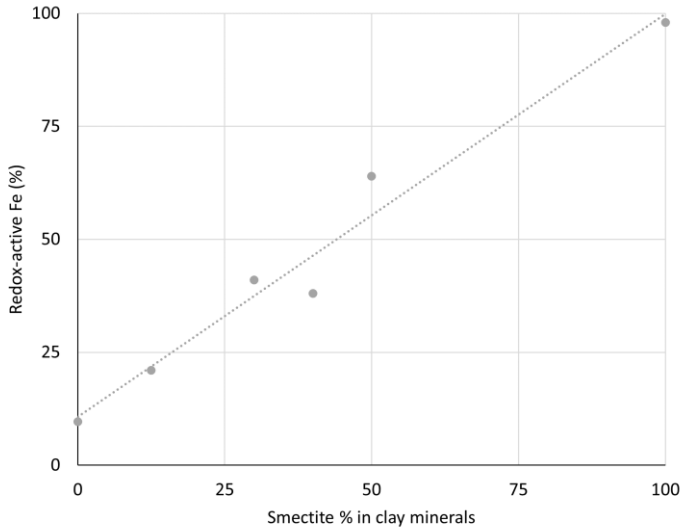

Figure 10. Percentage of redox-active Fe in various clay mineral standards (SWy-2, RAr-1, ISMt-1, ISCz-1, Fithian illite, IMt-1) measured by mediated electrochemistry (MEO at +0.6V, MER at -0.6V).

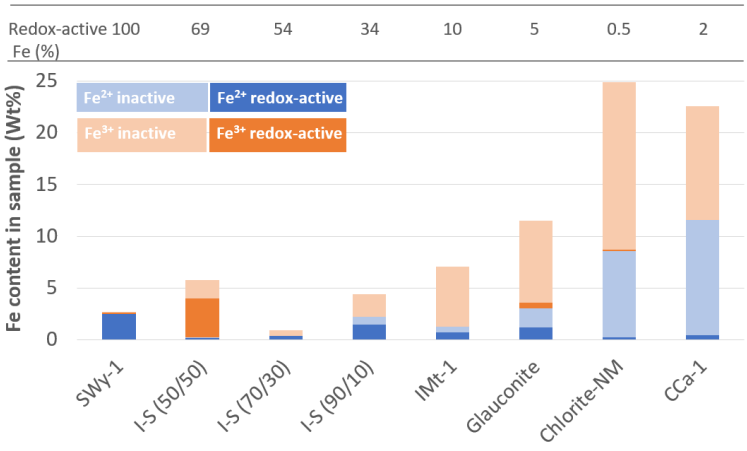

Figure 11. Redox-active Fe(II) and Fe(III) in reduced clay minerals measured by MEO and MER at 0.6V and -0.6V, respectively, and non-redox-active Fe(II) and Fe(III) (based on subtracting EDC from $Fe(II)_{total}$ and EAC from $Fe(III)_{total}$ obtained from the HF-phenanthroline method).

2.1.2.2 Brief description of methods used to tune Fe oxidation degree [PSI, BRGM]

[PSI]

Nontronite clay NAu-2 was reduced with Citrate-Bicarbonate-Dithionite (CBD) method following Stucki et al. Stucki et al. (1984) to different reduction degrees as low-red NAu-2 and high-red NAu-2. Different methods were applied on native NAu-2, low-red NAu-2, high-red NAu-2, and aqueous Fe^{2+} (Fe^{2+}_{aq}) to measure the Fe oxidation state and the results were compared.

- Mössbauer spectrometry probes the nucleus of Fe atom to the bulk of the sample.
- X-ray photoelectron spectroscopy probes excitations from core to valence bands. The penetration depth is in the order of 2-10 nm, which includes a full layer of the clay structure if properly oriented perpendicular to the beam.
- X-ray absorption spectroscopy (XAS, including X-ray absorption near edge structure (XANES) and extended X-ray absorption fine structure (EXAFS)) probes the bulk of a sample (at least tens of microns from the surface). Three independent analyses were made on the different range of the XAS spectrum. Normalized pre-edge was fitting with Voigt function to determine the centroid position; normalized main-edge was analysed with Linear combination fit (LCF) and iterative transformation factor analysis (ITFA); the extended region was analysed with shell fitting to correlate Fe-O bond length with Fe oxidation state. Native NAu-2 and Fe^{2+}_{aq} were taken as the standards of Fe^{3+} and Fe^{2+} in the analysis.
- Mediated electrochemical oxidation/reduction (MEO/MER) demonstrates the Fe oxidation state through measuring the electron donating and accepting capacities of Fe in the sample through chemical reactions.

Consistent results of Fe oxidation state were achieved at a mean value with a certain range of error.

Table 6. Fe(II) fractions in the three NAu-2 samples obtained by different measurements (Qian et al., 2023).

			XAS				
	Mössbauer at 77K	XPS	XANES centroid	XANES ITFA	XANES LCF	EXAFS Fe-O	MEO/MER
Native NAu-2	0.00	0.07	0.00	0.00	0.00	0.00	0.00
Low-red NAu-2	0.19	0.24	0.10	0.11	0.11	0.09	0.19
High-red NAu-2	0.44	0.46	0.33	0.39	0.38	0.36	0.58

[BRGM]

The Fe oxidation state of the nontronite samples was tuned by reducing Fe in the structure, since all Fe in the purified NAu-1 and NAu-2 samples was Fe(III). The protocol used was a citrate bicarbonate dithionite (CBD) method. Briefly, in a glove box with N_2 atmosphere, given amounts of nontronite were contacted with various amounts of CBD solution. Two series of reduced samples were produced, corresponding to NAu-1 and NAu-2 samples. In a first step, the samples were suspended in a solution of a 2:1 ratio of 1.2 M citrate and 1 M bicarbonate. Then, for the low-reduced samples, the same weight of dithionite as nontronite was introduced, whereas in the high-reduced sample, this dithionite to nontronite ratio was 3. The suspensions were then agitated for 1 d, centrifuged, washed with a 1 M NaCl solution, and then washed twice with distilled water, and finally the solid was collected and dried in an oven (at 40 °C) in the glove box.

2.1.2.3 Methods for converting K-Montmorillonite to Na-montmorillonite [RATEN, PSI]

[RATEN]

In sorption tests on pure montmorillonite conducted at [RATEN], a montmorillonite suspension with particles size <5 µm were used for Re sorption tests on pure clay mineral. To prepare such montmorillonite suspension, a K-type montmorillonite in powder form (commercialized by Sigma Aldrich), with a pH between 2.5 - 3.5 and a specific weight in the range of 300 – 370kg/m^3 was used

after the following procedure applied for its conditioning (*Paul Scherrer Institute, Laboratory for Waste Management (LES) - Experimental protocol: Clay conditioning procedure*):

- conversion of montmorillonite in Na-form with removing the soluble salts and easily soluble minerals and initiate the flocculation process.
- peptization and flocculation - size fractionation (<0.5 *μm):* Successive washings with de-ionised water, centrifugation (~7 minutes at 600g) and supernatant separation, re-flocculation with 1 or 2M NaCl.
- removal of soluble hydroxyl-aluminium compounds.
- adjusting the ionic strength - conversion to 0.1 NaCl

40 g of K -montmorillonite was prepared by the above-described procedure and a Na-montmorillonite suspension with a solid: solution ratio of 12.74 g/l was obtained and further used in the sorption tests. The main characteristics of the Na-montmorillonite suspension, related to the characteristics of 0.1M NaCl solution are given in

Table 7. The chemical composition of the aqueous phase of the montmorillonite, measured by ICP-OES is provided in Table 8.

Table 7. Main characteristics of the Na-montmorillonite suspension and of 0.1M NaCl solution.

	Montmorillonite suspension	0.1M NaCl
pH	6.10	5.78
Conductivity	10.96 mS/cm	10.72 mS/cm
TDS	5.48 g/l	5.36 g/l
Redox potential	153 mV	207 mV

Table 8. Chemical composition of the aqueous phase of the montmorillonite.

concentration [mg/L]						
Al	Ca	Fe	K	Mg	Na	Si
71.94	5.71	16.87	5.93	5.47	1764.49	360.00

The dry-weight of montmorillonite suspension in 0.1M NaCl solution was measured using a MOC120H type thermo-balance. For this, 4 aliquots of 10 ml suspension, under continuous stirring, was pipetted on the aluminium plates and dried at constant weight at 105°C. The results obtained are given in Table 9.

Table 9. Mass of montmorillonite, moisture, dry mass, and S/L ratio of the suspensions.

ID sample	Volume [mL]	Mass [g]	Moisture [%]	Dry mass [g]	S/L ratio [g/L]
1	10	10.023	98.69	0.1313	13.13
2	10	10.009	98.74	0.1262	12.62
3	10	9.938	98.75	0.1242	12.42
4	10	9.945	98.72	0.1279	12.79
Average					12.74

2.1.3 Iron oxides [ISTerre, HZDR]

[ISTerre]

Synthesis. Magnetite was synthesized following the protocol of Jolivet et al. (1992) in an N_2 filled glovebox where strict anoxic conditions (PO_2< 1 ppm) allowed to obtain 100% pure (according to Mössbauer and XRD) nanomagnetite. This was done by slowly adding 60 mL of 6 M NH_3 (Sigma-Aldrich) to 50 mL of solution containing [Fe_{tot}] = 0.55 M and [Fe(II)]/[Fe(III)] = 0.5, prepared by adding 0.4 M $FeCl_2$ (tetrahydrate, Sigma-Aldrich) to 0.8 M $FeCl_3$ (hexahydrate, Merck). The solution turned black immediately upon mixing and was left for 24 h on a rotary shaker. Afterward, a strong magnet was used to separate the magnetic particles, and the supernatant was filtered (0.22 μm MF-Millipore). The

magnetite was rinsed four times with water and two times with 0.1 mM NaCl solution, the latter one also used for its storage.

TEM. A few milligrams of the solid samples were placed in plastic tubes, filled with 10 mL of ethanol (previously stored for several weeks in the glovebox), sealed with Parafilm, and removed from the glovebox for 5 min for redistribution in an ultrasonic bath. Next, the solutions were immediately transferred back to the glovebox, diluted with ethanol, and drop-casted on pure carbon, 200 mesh Cu TEM grids (TED PELLA, INC.). The samples were transferred to the microscope in anoxic conditions and were in contact with air only for few minutes during mounting on the microscope sample holder. Conventional transmission electron microscopy (TEM), high angular angle dark field imaging in scanning mode (STEM-HAADF), X-ray energy-dispersive spectroscopy (XEDS), and selected area electron diffraction (SAED) patterns were collected at IMPMC, Sorbonne University, Paris, using a JEOL 2100F microscope. Fast Fourier transform on HR TEM images was carried out using ImageJ software, and the SAED pattern was indexed using SingleCrystal Software (Abràmoff et al., 2004). HR-TEM images show 8 nm large nanoparticles (Figure 12). The average crystallite size of 15 nm was estimated using the Scherrer equation, while TEM image showed rather large distribution of particles ranging from 5 to 50 nm, aggregated in large clusters (Figure 12).

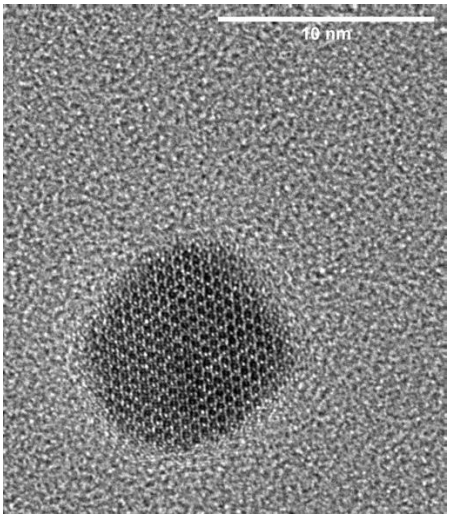

Figure 12. High Resolution STEM-HAADF image of a 10 nm nanomagnetite particle stabilized at pH 8.

XRD characterization. Magnetite (Fe_3O_4) and maghemite (γ-Fe_2O_3) have a similar inverse spinel structure with comparable unit cell parameters of 8.3963 Å and 8.347 Å in the microcrystalline state, difficult to differentiate by laboratory XRD. Magnetite contains both Fe^{2+} (in octahedral sites) and Fe^{3+} cations (in tetrahedral and octahedral sites), while maghemite is an oxidized form of spinel, containing only Fe^{3+} cations in the two types of sites. This leads to unit cell shrinking due to both the smaller size of the Fe^{3+} cation in relation to Fe^{2+}, and the formation of cationic vacancies in the octahedral sites necessary to maintain charge balance. Because of possible deviations from perfect magnetite stoichiometry corresponding to an $Fe^{2+}/Fe^{3+} = 0.5$, a whole range of mixed phases is possible ($Fe^{2+}/Fe^{3+} = 0$ for pure maghemite).

The samples were loaded inside the glovebox into Kapton capillaries, sealed with epoxy glue, and stored in anoxic conditions until measurement. X-ray powder diffraction data were collected at room temperature at the ID31 beamline at the ESRF (λ = 0.1907 Å) using a Pilatus3 X CdTe 2 M detector with 172 Å~ 172 µm pixel size. The detector was calibrated using the NIST-certified CeO_2 674b standard. Azimuthal integrations were performed using the pyFAI package (Kieffer and Karkoulis, 2013). The lattice parameters, average crystallite sizes using the Debye−Scherrer equation, and phase fractions were determined using Rietveld analysis with the FullProf Suite (Rodriguez-Carvajal, 2000). The advantages of synchrotron over laboratory X-ray source are a better signal-to-noise ratio, thanks to high photons flux and a noise-free detector, faster measurements (few seconds vs few hours), and the smaller amount of powder required (beneficial for small-scale sorption experiments). An average

crystallite size of 15 nm was estimated using the Scherrer equation, while the TEM image showed rather large distribution of particles ranging from 5 to 50 nm, aggregated in large clusters. Although phase identification by laboratory XRD is challenging, due to nearly identical contribution of the crystallographic planes, it is still feasible. Several XRD patterns measured using a laboratory device (Bruker D8) and synchrotron X-rays confirmed that the synthesized magnetite that was kept in the glovebox, as well as stabilized at pH ≥ 7, represented the pure phase with Fe^{2+}/Fe^{3} = 0.5 and *a* = 8.39 Å (Figure 13).

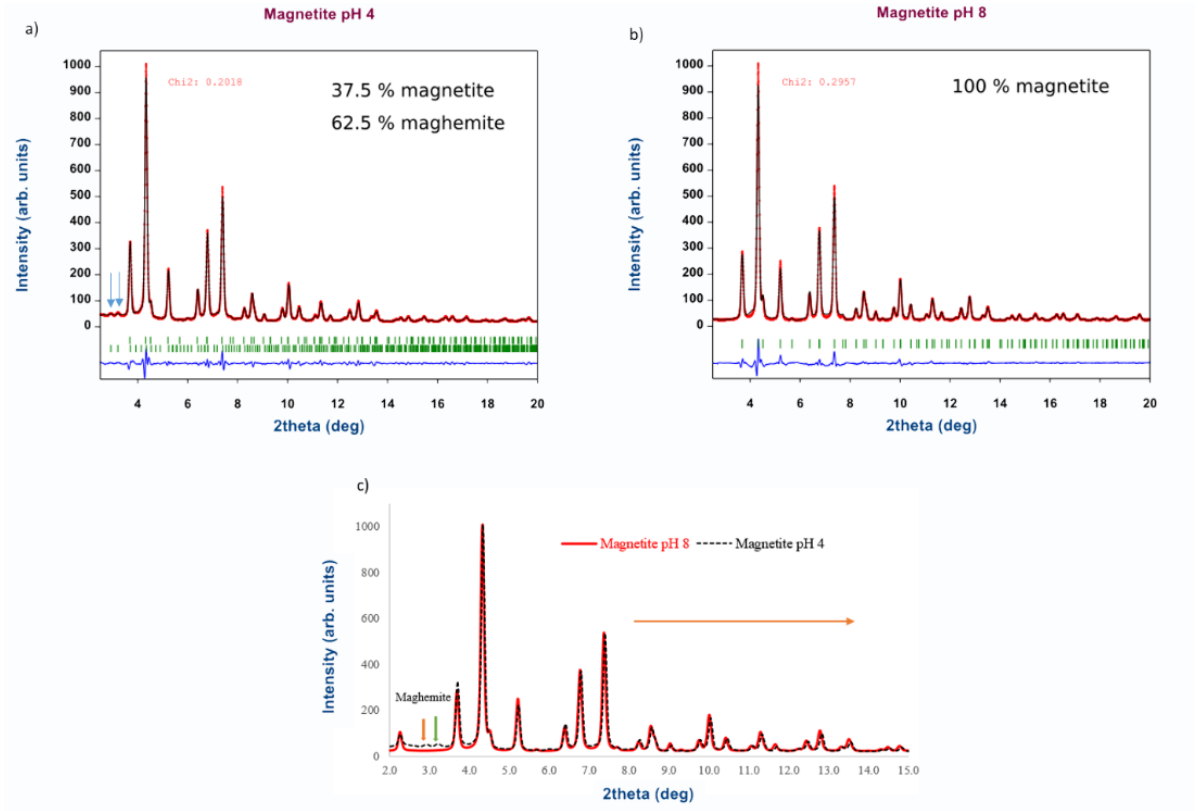

Figure 13. (a) Fits of XRD patterns of magnetite (a = 8.39 Å) stabilized at pH 4 and 8 (λ = 0.1907 Å). Imperfect fit of the 3 most intense peaks comes from memory effects of the detector. The two blue arrows show peaks of a similar intensity typical for maghemite (a = 3.42 Å). (b) Superimposed patterns of magnetite stabilized at pH 4 and 8 highlighting the peak shift due to magnetite transformation to maghemite and the new peaks at 2theta = 2.9 and 3.2°.

^{57}Fe Mössbauer. Mossbauer spectroscopy was used to quantify (complementary to XRD) the magnetite to maghemite transformation occurring either in acidic pH as a consequence of Fe^{2+}(aq) release or as a consequence of Se (or Re) redox reaction with magnetite or co-adsorbed Fe^{2+} (Charlet et al., 2023). Spectra were collected at 300 and 77K using a conventional constant acceleration transmission spectrometer with a ^{57}Co(Rh) source and an α-Fe foil as the calibration sample. To obtain 5 mg Fe/cm^2 to satisfy the fine absorber conditions, 20 mg of the powder was loaded inside the glovebox in flat round plastic holders, sealed with epoxy glue, and transported in oxygen-free conditions. Then, the hyperfine structure was modelled by means of quadrupole doublets and/or magnetic sextets with Lorentzian lines using the homemade program MOSFIT (Teillet).

A typical Mössbauer spectrum of microcrystalline magnetite at room temperature consists of two magnetic sextets, one due to Fe^{3+} in tetrahedral positions and the other one due to Fe^{3+} and Fe^{2+} in octahedral positions, which are averaged as $Fe^{2.5+}$ because of fast electron exchange above the Verwey transition at about 125 K. The ratio between $Fe^{3+}/Fe^{2.5+}$ is equal to ½. On the other hand at 77 K, the spectrum differs from that at room temperature due to the Verwey transition observed at about 119 K, below which electron hopping is absent and the hyperfine structure must be described by means of the superposition of different magnetic sextets. A structural change from cubic (300 K) to monoclinic (77 K) phase can be best fitted with three to five sextets. In the case of microcrystalline maghemite, the

Mössbauer spectra consist of one magnetic sextet at temperatures below its magnetic ordering temperature T_N, which must be described by means of two magnetic components attributed to Fe^{3+} species, according to the values of isomer shift, located in tetrahedral and octahedral positions. Therefore, the stoichiometry of magnetite can be accurately estimated by Mössbauer measurements, which allow the Fe^{2+}/Fe^{3+} ratio to be successfully determined from the least square data fitting, particularly from the mean value of the isomer shift.

In the present study, the Mössbauer spectrum of the "pure" magnetite at 300K (Figure 14, left) differs from the typical one, and shows broadened lines due to superparamagnetic relaxation effects due to the presence of nanoparticles.

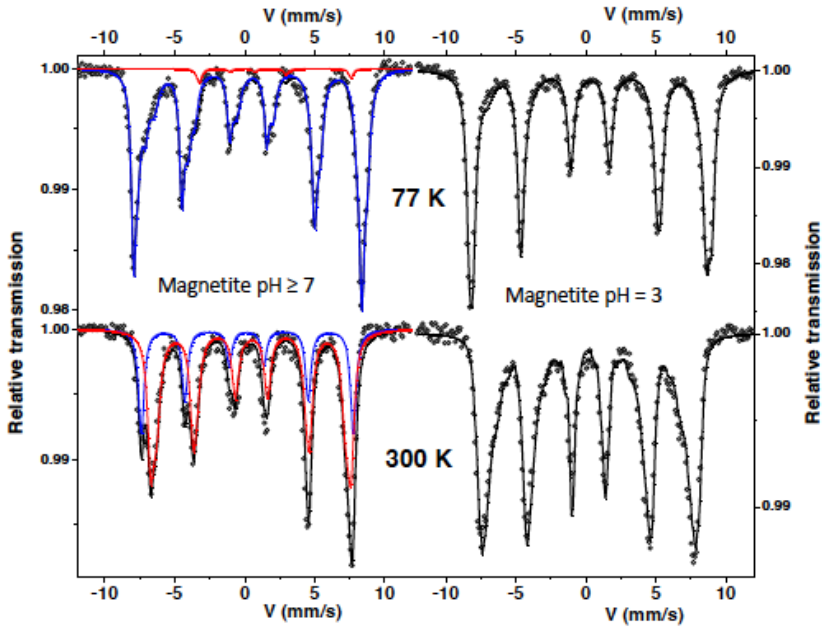

Figure 14. Left: Mössbauer spectra of the pure magnetite synthesized in a glovebox, measured at 77 K and 300 K, fitted with three components containing Fe(II) and Fe(III) species; Right: Mössbauer spectra of the magnetite stabilized at pH 3, containing about 82 % of a maghemite at 77 K and 300 K.

[HZDR]

Synthesis of iron oxides and Tc sorption. To simulate anoxic underground repository conditions as close as possible, all experiments were carried out in a glove box under N_2 atmosphere (Glovebox-System GS050912) with an oxygen content always below 2 ppm. Furthermore, magnetite suspensions, without and with added pertechnetate, were always kept in closed vials with little gas-filled headspace to create a large redox buffer and eliminate as much of the remaining 2 ppm oxygen of the glovebox atmosphere. Further measures included the use of fresh reagents and boiling of the milli-Q water (resistivity of 18.2 MΩ·cm, Water Purified®) used for the experiments for at least two hours for degassing. Magnetite nanoparticles were synthesized following the procedure detailed in (Jolivet et al., 1992). Tc sorption studies were conducted as follows: Magnetite suspensions (4 g/L) were equilibrated at given pH values one day prior to Tc addition (pH_{ini}). After Tc addition, the pH was regularly checked and adjusted. The resulting suspensions were shaken in a horizontal shaker for a given time, after which pH (pH_{end}) and Eh values were measured. Samples were centrifuged (6000 rpm for 10 min). Subsequently, the supernatant was analysed for Tc and Fe concentration and the precipitate was characterized via TEM, X-ray absorption spectroscopy (XAS) and X-ray photoelectron spectroscopy (XPS). Tc contact experiments to evaluate pH effects were performed at a load of 600 ppm Tc, i.e., 24.3 µM Tc^{VII} in 50 ml H_2O containing 200 mg magnetite for four weeks with initial pH (pH_{ini}) in the range of

2.0-14.0 in steps of full units. In Tc contact experiments to evaluate the effect of time, three different pH_{ini} (5.0, 7.0, 10.0) were investigated in time steps of 1 d, 14 d, 28 d and 49 d.

Tc co-precipitation with magnetite. For Tc magnetite co-precipitation experiments, 110 mg $Fe^{II}Cl_2 \cdot 4\ H_2O$ and 280 mg $Fe^{III}Cl_3 \cdot 6\ H_2O$ (resulting in 200 mg magnetite) were dissolved in 45 ml of a 0.01 M HCl. Subsequently, an aliquot of Tc stock solution was added to the Fe^{II} and Fe^{III} solution, followed by the addition of 3.125 ml of 6 M NH_4OH. The pH cannot be controlled, because the addition of base has to be instantaneous, otherwise impurities of different Fe-phases might occur. The resulting solid, hereafter referred to as co-precipitate (CoPrec), was washed the same way as magnetite as described above. CoPrecs were equilibrated in the final washing solution for seven days. Afterwards, the samples were centrifuged, and the supernatant was analysed (see below). Three different CoPrecs with variable Tc load per magnetite (600, 3000, 10000 ppm) were synthesized.

pH and Eh measurements were carried out in suspensions without agitation, using a pH meter (pH3110, WTW) with pH electrode (SI Analytics Blue Line) for pH, and a Pt electrode with Ag/AgCl (InLab Redox Micro, Mettler Toledo) with a redox buffer solution (220 mV / pH = 7). The measured Eh values were converted to hydrogen standard electrode by adding +207 mV. The Tc concentrations in the supernatant were determined by liquid scintillation counting (LSC) using a scintillation cocktail (Ultima Gold™, Perkin Elmer) and a liquid scintillation counter (1414 LSC Winspectral α/β Wallac, Perkin Elmer. Fe concentrations (total and Fe(II)) were measured using inductively coupled plasma mass spectrometry (ICP-MS) (NexION 350x from Perkin Elmer) and the ferrozine essay (Stookey, 1970). The Tc-containing wet pastes were mounted on double (for Tc load of 600 ppm) or quadruple sealed (for Tc loads > 600 ppm) HDPE sample holders inside the glovebox for XAFS measurements. The samples were immediately flash-frozen with liquid nitrogen when taken out of the glovebox and stored in a liquid nitrogen container for storage and transportation to prevent further aging and oxidation of the samples.

EXAFS measurements. Samples were measured at the Rossendorf Beamline (BM20) at the European Synchrotron Radiation Facility (ESRF) in Grenoble, France (Scheinost et al., 2021). Tc K-edge (21 044 eV) XAS spectra were acquired in fluorescence mode. The energy of the Si(111) double crystal monochromator was calibrated using a Mo foil (edge energy 20 000 eV). Two Rh-coated mirrors were used to collimate the beam onto the first monochromator crystal. Fluorescence spectra were collected with an 18-element, high-purity, electrically cooled solid-state Ge detector (Ultra-LEGe, GUL0055, Mirion Technologies) with digital spectrometer (XIA Falcon-X). During the measurement, the samples were kept at 15 K within a closed cycle He cryostat to avoid photon-induced changes of oxidation state and to reduce thermal disorder.

2.1.3.1 Synthesis of Fe oxides for sorption experiments in mixtures [CIEMAT]

[CIEMAT] synthetized in the laboratory goethite, magnetite and ferrihydrite oxides following the receipts described in (Cornell and Schwertmann, 2003; Missana et al., 2003a; Missana et al., 2003b), commercial metallic Fe(0) shavings (MERCK), and commercial hematite (Fe_2O_3) from Sigma Aldrich were also used. These oxides were obtained to carry out radionuclide sorption experiments on mixtures of bentonite with variable Fe-oxide concentration, evaluating a canister/bentonite interface in a scenario where canister corrosion released iron corrosion products, which may affect redox conditions and radionuclide sorption properties in smectite.

2.1.4 Green Rust [BRGM, CIEMAT]

2.1.4.1 Synthesis of green rust with monovalent interlayer anions [BRGM]

The synthesis of green rust with interlayer Cl was done based on the one pot chemical clock synthesis protocol of Hadi et al. (2014). This method is based on the simultaneous addition, in an O_2-free glovebox, of stoichiometric addition of cobaltihexamine and $FeCl_2$. After a few hours of induction time, the green rust samples are produced within a few seconds. The chemical composition (Fe^{II}, Co^{II}, Fe^{III} layer composition, amount of Co^{II} within the layers, layer charge) can be controlled by varying the ratio of

cobaltihexamine and $FeCl_2$. For this study, we targeted the synthesis protocol of sample "P2" in Hadi et al. (2014), that is a 3D-ordered green rust having particle size in the 0.1-1 µm size range.

2.1.4.2 Synthesis of green rust with divalent interlayer anion [CIEMAT]

[CIEMAT] synthetized sulfate green rust inside a glove box, under N_2 atmosphere, following the recipe described in (Cuttler et al., 1990). To do so, 50 mL of ferric 0.08 M $Fe(NO_3)_3$ solution were mixed to 200 mL ferrous 0.1 M $FeSO_4$ solution, with pH fixed at 7. After mixing, samples are centrifuged and washed with deionised water, and the precipitated is dried inside the glove box, in the absence of O_2. XRD spectra agreed to an Fe(II) sulfate hydroxide.

2.2 Natural clay rocks used for experimental works

2.2.1 Callovian-Oxfordian Clay rock [CEA]

Raw COx samples were provided by Andra (CMHM, Bure, France) and send to CEA/L3MR for storage and preparation under controlled atmosphere in gloveboxes. Rock cores were drilled in borehole EST51764 (OH26126, K8 and K12). Solid samples for diffusion cells were sliced using a wire saw in glovebox under constant nitrogen flushing. Diffusion sample dimensions are ΔL×Ø ~ 1.1 × 1.9 cm. Three diffusion experiments were conducted with samples Diff_U_COx_C7 C8 and C9. Complementary analyses were performed on pre-existing sample Diff_U_COX_C3. Results were compared to previous data obtained with analogous samples C1 to C6 (Fralova, 2021; Fralova et al., 2021). Some remaining rock cores and pieces were crushed in glovebox and sieved under 125 µm. Corresponding COx powder was stored in glovebox ($[O_2]$ ~ 1-10 ppm) under aluminium bag until use. A 25g-batch of COx powder was sent to IPHC (Strasbourg, France) for experiments in the framework of FUTURE / Task 2. Other powder samples were pre-equilibrated for adsorption experiments. Synthetic "porewater" was prepared by dissolution of salts, aiming reference composition (Fralova et al., 2021). The corresponding solution was mixed with "sacrificial" clay powder for equilibration of trace elements (Al, Si, DOM). Two steps of 48h-mixing at least were performed with a solid to liquid ratio S/L ~ 10 $g \cdot L^{-1}$. Solution was then centrifugated to remove clay and ultrafiltered to remove colloids and prevent bacterial activity. Porewater was then bubbled with N_2/CO_2 (1 %) for 1 hour to adjust pH to ~7.2 ± 0.2. Part of the corresponding porewater was used to pre-equilibrate powder and diffusion cells. Several hydration steps, between 2 days up to 2 weeks, were used with a liquid to solid ratio L/S ~ 10 L/kg. Reduced samples were also prepared following the clay conditioning procedure proposed within the task 3. Samples were first decarbonated using lixiviation by slow addition of HCl (1 M), until pH drops in the range pH ~ 3 ± 1 (Rasamimanana et al., 2017). Decarbonated Cox samples were reduced by citrate dithionite treatment, with a sodium citrate (0.27 M) / sodium bicarbonate (0.1 M) extraction solution and a sodium dithionite (200 g/L) (@ 80°C / 30 min). Reduced Cox powder samples were washed three times and pre-equilibrated with synthetic porewater, with or without reducing agent (N_2H_4 ~ 10^{-2} M) before batch experiments.

2.2.2 Red Clay [RATEN]

For the sorption tests on natural clay rock, a sample from Saligny site (the preferred site for the future Romanian near surface disposal facility for LILW-SL) was selected. According to the technical specification the clay rock was sampled from 50 – 55m depth.

As the data on the physico-chemical composition of this clay sample are missing, a partial characterization of this sample with high clay content was performed. The pH of the clay sample is alkaline (8.96), the sample has an apparent density of 1.216 g/cm^3 and a moisture content of 2.97%. The measured redox potential is 126.4 mV, specific for an oxidizing environment. The clay samples (drill cores) were kept in aerobic conditions for a long period of time, so it is possible that the measured redox potential does not correspond to the in-situ conditions. The chemical composition of the clay was measured by ICP-OES after previously acid digestion of the sample in microwave field (in the presence of concentrated HNO_3 and concentrated HF). In parallel with the clay sample a standardized soil sample - SRM 2709a was subjected to the same mineralization process to determine the recovery yield. The

obtained results show that beside silicon oxides, the analysed sample contain aluminium, calcium and iron oxides (

Table 10).

Table 10. Chemical composition of the clay, in wt%.

Al_2O_3	CaO	Fe_2O_3	MgO	MnO_2	Na_2O	SiO_2
29.75	11.06	8.43	1.19	0.04	6.69	42.83

Iron ions have an important role in the Tc retention process facilitating its reduction to Tc(IV), a compound that can adhere to the clay surface. According to literature data, a reducing environment favours the reduction of structural octahedral Fe(III) to Fe(II), Fe^{2+} ions migrate from the *cis*-octahedral positions to the adjacent *trans*-octahedral ones, developing tri-octahedral Fe^{2+} groups that are separated from the vacant positions. The reduction is accompanied by dehydro-oxylation reactions due to the protonation of the OH groups initially coordinated by Fe^{3+}. The negative charge resulting after Fe^{3+} reduction is located at the "O" type ligands located at the boundary between the trioctahedral layer, and the vacant positions are compensated by sorption of protons and cations from the solution (Barton and Karathanasis, 2002).

As localization of iron ions was not possible to perform at RATEN, the extractable Fe was measured applying a procedure for extractable elements measurement with sodium dithionite and sodium citrates allowing to obtain information on the presence of Al, Fe and Mn in the form of complex organic compounds and in the form of amorphous inorganic compounds (*Extractable Al, Fe, Mn, Si procedures from (F. Courchesne and Turmel)*).

For the Saligny red clay used in the sorption tests performed in RATEN around 5% of the iron content is extractable indicating its presence in the form of organic compounds but also amorphous inorganics (Table 11).

Table 11. Total and extractable Al, Fe, and Si in the Saligny Red clay.

	Al	Fe	Si
Total elemental composition of clay sample[mg/g]	81.80	30.65	207.65
Extractable elements with DT procedure [mg/g]	0.1471	1.5001	0.7826
% extractable	0.18	4.89	0.377

The cation exchange capacity (CEC) measured for Saligny red clay sample is 62.33 meq/100 g. The pH value of ~9 indicates an alkaline environment in which the number of edge negative charges is increased, which leads to an increased CEC value. The high concentration of exchangeable Ca, correlated with the high concentration of total Ca concentration in the clay sample, indicates that Saligny clay has a high content of calcium carbonate. A high CEC value (> 25 meq/100 g) is representative for a rock with a high clay content, predominantly as smectite like minerals.

The mineralogy measured on the clay sampled from Saligny site from similar depth with the Red clay used in RATEN sorption tests is shown in Table 12. The composition of the pore-water relevant for Saligny red clay that was used in the sorption test is provided in Table 13.

Table 12. Mineralogical composition of the clay sampled from Saligny site (wt%).

Quartz	Feldspar	Mica	Carbonate	Smectite	Illite	Kaolinite
20	4	7	44	14	10	2

Table 13. Pore-water composition relevant for Saligny Red clay.

Al [mg/L]	Ca [mg/L]	Fe [mg/L]	Mg [mg/L]	Mn [mg/L]	Na [mg/L]	Si [mg/L]
3.1633	29.6573	0.4980	6.9830	0.0257	6.0357	9.9762

2.2.3 FEBEX clay [CIEMAT]

[CIEMAT] selected FEBEX clay, a Ca-Mg bentonite with high smectite content, from Cortijo de Archidona, Spain (Fernández and Villar, 2010; Huertas et al., 2000) with three purposes: (i) as reference material because the sorption properties of this clay towards many different elements have been analysed (Missana et al., 2021), also within EURAD (Missana et al., 2023). In particular, previous sorption results of ^{233}U(VI) (Missana et al., 2009b) and ^{75}Se(IV) (Missana et al., 2009a) on Ca-Mg FEBEX clay were used to compare the sorption behaviour of these elements on Fe-rich smectites and on Fe-oxide-free clay fractions, analysed in the present project. (ii) to carry out sorption experiments on smectite mixed with known proportions of Fe-phases and oxides and (iii) to carry out ^{75}Se(IV) retention/diffusion experiments in compacted pure and mixed materials.

2.3 Beamline developments aiming at an improved capacity to study elements speciation.

2.3.1 European radionuclide beamlines [KIT and HZDR]

To the best of our knowledge, only five dedicated radionuclide beamlines are currently fully operational, all of them in Europe. Many characteristics are shared amongst those beamlines, including a variety of techniques. ROBL-II provides with its four permanently mounted experimental stations the possibility to use all available techniques even during a typical six-day run, with easy sample transport between the stations, which are in one controlled area. Other distinguished features are the high-count-rate detector and multisample cryostat for EXAFS, the six-crystal spectrometer with complete crystal sets for 1 and 0.5 m Rowland radii, and finally the surface and single-crystal diffraction stations for radioactive samples offered by XRD-1 and XRD-2. The two KARA beamlines at KIT are distinguished by their proximity to dedicated alpha labs of INE, where sample preparation can be performed, as well as the possibility for in situ experiments at non-ambient conditions including heating up to 2000 K. Although beam time is no longer provided through the typical proposal review process, it is provided through collaboration with INE. While these previously described beamlines have been designed with predominately alpha-emitting radionuclides in mind, the experimental stations of the MARS beamline of Soleil incorporate substantial lead shieldings around samples to enable the measurement of much stronger gamma-emitting samples. Such lead-shieldings can also be (temporarily) established at the microXAS beamline of the SLS/PSI, which is further discriminated by its high spatial resolution through strong microfocussing down to 1 micrometer.

2.3.2 ROBL-II Beamline [HZDR]

The Rossendorf beamline has been operated at the ESRF since 1996 by Helmholtz-Zentrum Dresden-Rossendorf (HZDR) (Matz et al., 1999; Nitsche, 1995; Reich et al., 2000) and has been redesigned in 2016–2020 (ROBL-II). Embedded within the Helmholtz Association's program on nuclear safety, ROBL-II is dedicated to research on actinides and other elements with no stable isotopes (Tc, Po, Ra). The beamline hosts four major experimental stations for synchrotron X-ray experiments in two radiochemistry hutches (RCH-1 and RCH-2) (Figure 15): 15 (1) XAFS station with fluorescence and transmission detection for X-ray absorption fine-structure (XAFS) spectroscopy, including (conventional) X-ray absorption near-edge structure (XANES) and extended X-ray absorption fine structure (EXAFS) spectroscopies. (2) XES station with a five-crystal Johann-type spectrometer for high-energy-resolution fluorescence-detection X-ray absorption near-edge spectroscopy (HERFD-XANES), X-ray emission spectroscopy (XES) and resonant inelastic X-ray scattering (RIXS) measurements. (3) XRD-1 station with a heavy-duty, Eulerian cradle, six circle goniometer for (high-resolution) powder X-ray diffraction (PXRD), surface-sensitive crystal truncation rod (CTR) and resonant anomalous X-ray reflectivity (RAXR) measurements. (4) XRD-2 station with a Pilatus3 x2M detector stage for single crystal X-ray diffraction (SCXRD) and in situ/ in operando PXRD measurements. Details can be found in (Scheinost et al., 2021).

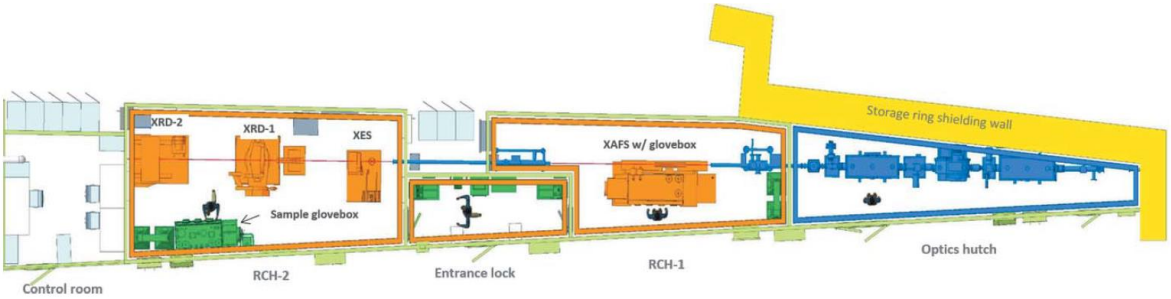

Figure 15: Layout of ROBL-II, showing from right to left the X-ray Optics hutch (blue), the two experimental hutches (RCH-1 and RCH-2) connected by a common entrance lock room (orange), and the control room. The X-ray beam marked by the red line enters from the right through a port in the shielding wall. RCH-1 houses the XAFS experiment, RCH-2 a five-crystal spectrometer (XES), a six-circle goniometer for powder and surface diffraction (XRD- 1), and a Pilatus3 2M diffractometer (XRD-2). Hutch walls are shown in light green, radiation protection equipment in green (Scheinost et al., 2021).

2.3.3 XES at ROBL-II [HZDR]

[HZDR] X-ray emission spectrometers are used for several techniques, including X-ray emission spectroscopy (XES), high-energy resolution fluorescence-detection X-ray absorption near-edge structure spectroscopy (HERFD-XANES), resonant inelastic X-ray scattering (RIXS) and/or resonant inelastic X-ray emission spectroscopy (RXES) (Glatzel and Bergmann, 2005). Two spectrometers are available at ROBL: a one-crystal and a five-crystals spectrometer. The one-crystal spectrometer is used only for specific experimental setups, which require detection of emitted X-rays in particular scattering geometries (Kvashnina and Scheinost, 2016). The five-crystals spectrometer is the principal instrument for standard HERFDXANES, XES, RIXS and RXES experiments (Figure 16).

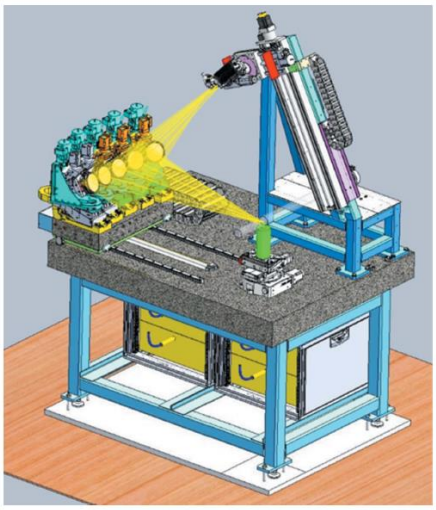

Figure 16: Schematic drawing of the five-crystals X-ray emission spectrometer (Scheinost et al., 2021).

The spherically bent crystal analysers, the sample and the detector are mounted in vertical Rowland geometry. Each of the five crystals monochromatizes the fluorescence according to Bragg's law and focuses the reflected monochromatic photons into the detector (Kleymenov et al., 2011). The resolution of the instrument depends on the selected Bragg angle of the analyser and is thus linked to the selected energy. The best resolution is obtained in the backscattering geometry at Bragg angles close to 90° due to the geometrical effect of the Johann geometry (Kleymenov et al., 2011; Sokaras et al., 2013)). The resolution is further improved by a motorized slit (typically 1 mm) in front of the detector. ROBL's five-crystal spectrometer covers the Bragg angles 65–89°. For concentrated samples an avalanche photodiode (APD) with an area of 10 mm × 10 mm, and for dilute samples a Ketek detector with 10 mm diameter and 450 mm Si thickness are available. The five-crystal spectrometer can be operated with

crystal analysers with 0.5 m and 1 m bending radius (Rovezzi et al., 2017). Available spherically bent striped crystal analysers (100 mm diameter) cover most elements of the periodic table in the energy range 3–20 keV. Note that the whole spectrometer setup (sample, analyser crystals and detector) can be placed into a He-filled bag to obtain sufficient fluorescence yield also at the lowest energies. Energy scans are based on the Bragg angle and trigonometric equations that follow the Rowland circle geometry (Kvashnina and Scheinost, 2016). Each crystal analyser is mounted on four motorized translation stages: two linear stages for the up/down and horizontal (closer or farther from the sample) motions, a goniometer to focus the fluorescence on to the detector, and a cradle for Bragg angle selection. The detector is mounted on two perpendicular, linear stages, and a goniometer to follow the Bragg angle reflection and to use different detector angles. HERFD-XANES measurements are performed by scanning the incident energy across the absorption edge of the selected element at the maximum of the X-ray emission line. XES spectra are measured by scanning the emitted energy with the crystal analysers, while keeping the incident energy fixed. If the incident energy is selected above the X-ray absorption edge, non-resonant XES is recorded. If the incident energy is selected below or near the absorption edge, RXES or/and RIXS is recorded. In order to minimize the down-time between the different techniques and to accustom the spectrometer operation for users' needs in general, the PyXES software has been developed, which allows to select the chemical element, the absorption edge (K, L, M), the emission line, and the crystal analyser set, and moves all motors positions into optimal instrumental settings corresponding to the provided input. Energy ranges for HERFD-XANES, XES, and RIXS are proposed automatically and can then be adjusted by the user. Additionally, batch scripts can be written to set up automatic measurements for several samples and/or techniques. The current position of all spectrometer motors and their expected position upon the selection of a particular experiment are displayed. We demonstrate here the different techniques using ThO_2, prepared as a powder sample sealed between two layers of Kapton foil of 25 mm thickness (Amidani et al., 2019).

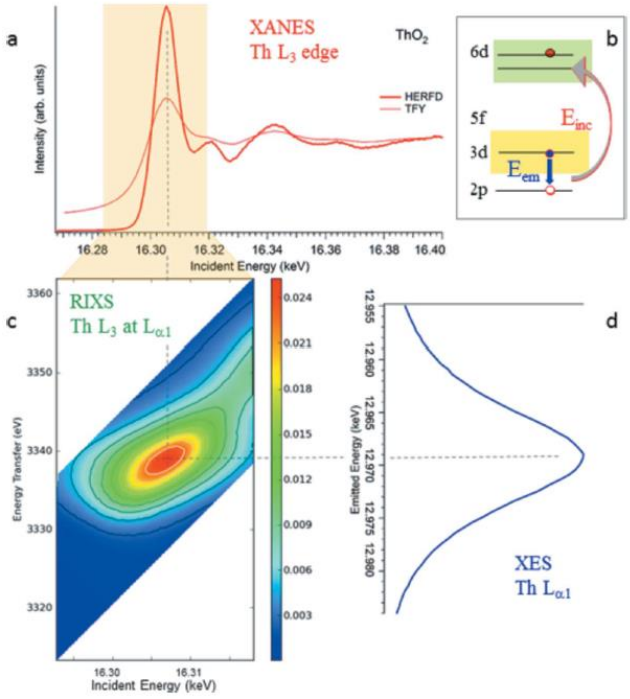

Figure 17: XANES, XES, and RIXS of ThO_2. (a) Th L_3-edge XANES spectra recorded in the conventional, total fluorescence yield (TFY) mode in comparison with the HERFD mode. (b) Electronic transitions of the XANES, XES, and RIXS process. (c) RIXS map recorded near the maximum of the Th L_1 emission line with incident energies near the maximum of the Th L_3 edge. (d) XES Th L_{alpha1} spectrum recorded with non-resonant excitations (Scheinost et al., 2021).

Figure 17 (a) shows the conventional Th L_3-edge XANES (collected in normal, total fluorescence yield mode without crystal analyser, 'TFY') in comparison with the HERFDXANES spectrum recorded at the

maximum of the Th L1 ($3d_{5/2}$–$2p_{1/2}$) emission line 12968 eV) as a function of the incident energy (collected in about 5 min). The emission energy was selected using the (880) reflections of five spherically bent striped Si crystal analysers with 0.5 m bending radius aligned at 84.4 Bragg angle. The intensity was normalized to the incident flux. A combined (incident convoluted with emitted) energy resolution of 2.5 eV was determined by measuring the full width at half-maximum (FWHM) of the elastic peak of tungsten foil. The full RIXS map [Fig 17c)] established by scanning the incident energy at different emission energies was recorded in about 30 min. The XES shown in Fig 17(d) was obtained by scanning the X-ray emission energy at fixed incident energy above the Th L_3 edge (16.5 keV). Following the dipole selection rules, the XANES spectrum arises from electron excitations from the ground 2p level to the unoccupied 6d level [Fig 17(b)]. The lifetime of the core hole created by this process is very short and core state is quickly filled in by an electron from the higher levels. The X-ray photons emitted during the process 3d → 2p are measured by XES at the Th L_{alpha1} emission line.

2.3.4 ACT beamline [KIT]

CAT-ACT-the hard X-ray beamline for CATalysis and ACTinide/radionuclide research at the KIT light source is dedicated to the investigation of radionuclide materials with activities up to one million times the German law exemption limit by various speciation techniques applying monochromatic X-rays. This section highlights the latest technological developments at ACT-station that enable high resolution X-ray absorption near edge structure (HR-XANES) spectroscopy for low radionuclide loading samples - encompassing the investigations of actinide (An) elements down to 1 ppm concentration - combined with a cryogenic sample environment reducing beam induced sample alterations. One important part of this development is a versatile, gas tight plexiglass encasement ensuring that all beam paths in the five-analysers crystal, Johann-type X-ray emission spectrometer run under He atmosphere. The setup enables the easy exchange between different experiments (conventional XAFS, HR-XANES, HEXS/WAXS, tender to hard X-ray spectroscopy) and opens the possibility for the investigations of environmental samples such as specimens containing transuranium elements from contaminated land sites or samples from sorption and diffusion experiments to mimic the far-field of a breached nuclear waste repository. Details can be found in (Schacherl et al., 2022b) and schemes of the He box, microstatHe chamber, kapton cell are respectively provided in Figure 18, Figure 19, and Figure 20. An example of the resolution that can achieved and of the effect of cryogenic conditions is provided in Figure 21 where the effect of irradiation time and temperature on a Np-sorbed illite is shown.

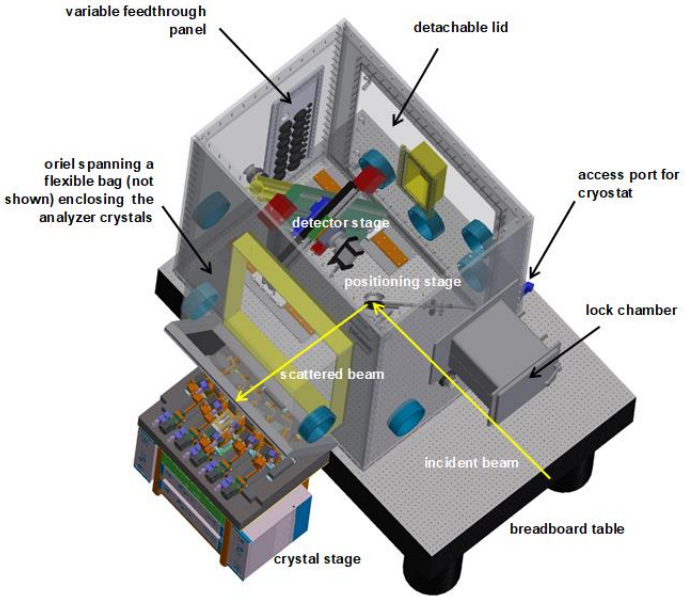

Figure 18. 3D CAD model of the He box providing an improved concept with possibilities for several experiments, e.g., enabling in situ measurements and cryostat experiments at the M-edges of actinides at the ACT station (Schacherl et al., 2022b).

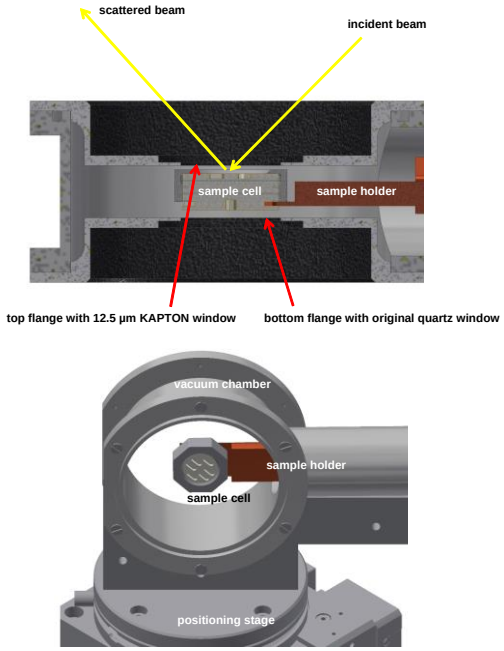

Figure 19. Top – cross-section CAD drawing of the modified MicrostatHe vacuum chamber (side view). The original sample holder has been replaced by a copper fork clamping the sample cell as described in section 4; bottom – 3D CAD drawing of the vacuum chamber with removed flanges mounted on top of the positioning stage - exhibiting sample holder (copper fork) and sample cell assembly (Schacherl et al., 2022b).

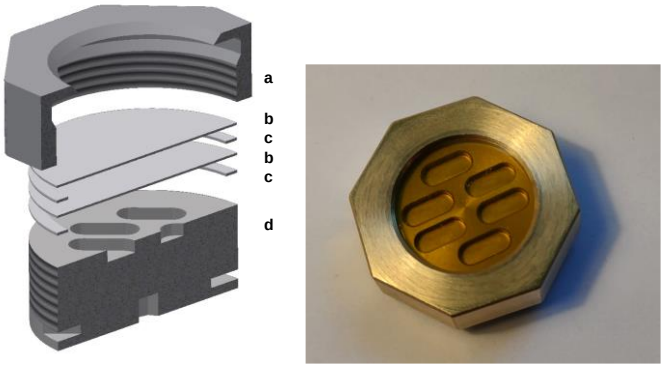

Figure 20. Left image – exploded view CAD drawing of the sample cell assembly – from top to bottom: (a) cap nut, (b) KAPTON disk, (c) TEFLON gasket, (b) KAPTON disk, (c) TEFLON gasket, (d) cell body; right image – top view of a sealed sample cell with six sample cavities (outer diameter ~30 mm) (Schacherl et al., 2022b).

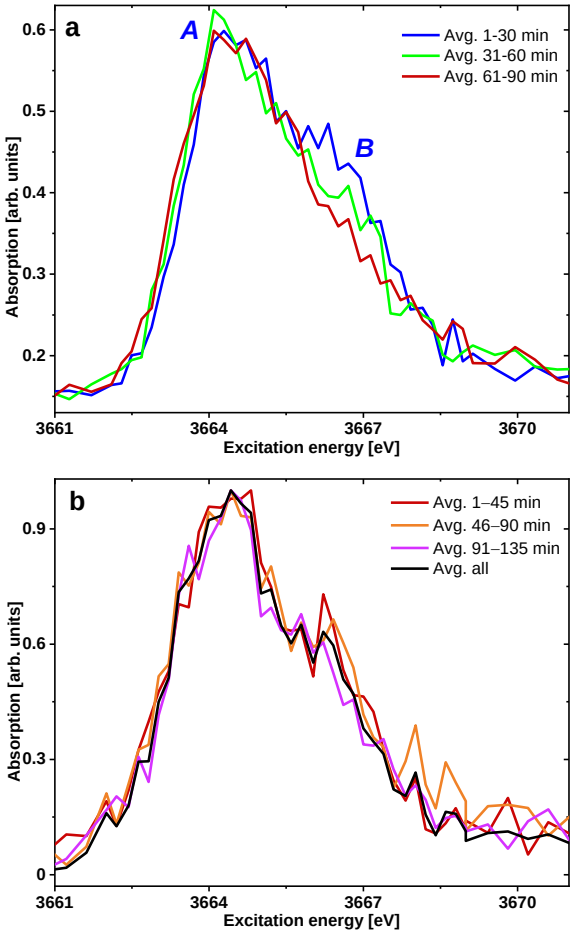

Figure 21. a) Gradual change of Np M_5-edge HR-XANES spectra of a sample with 83 ± 2 ppm Np sorbed on illite (cf. section 6 for sample details) at 300.0 ± 1.5 K, changes in the shoulder denoted as feature B are visible with irradiation time. b) At cryogenic conditions (141.2 ± 1.5 K), no significant changes of the spectra are discernible within the noise level (Schacherl et al., 2022b).

2.3.5 Paving the way for examination of coupled redox/solid-liquid interface reactions: 1 ppm Np adsorbed on clay studied by Np M5-edge HR-XANES spectroscopy [KIT]

The focus of project hosted at KIT, was on redox state and speciation measurements of Np adsorbed on the clay mineral illite at low metal ion loadings, using Np M_5-edge HR-XANES spectroscopy while avoiding beam-induced oxidation state changes. To lower the instrumental detection limits for Np loadings, the experimental set-up was optimised. This included the emplacement of the spectrometer within a tight but flexible He flushed casing and applying a liquid N_2 cryostat set-up for cooling the sample during measurements. The experiment was equipped with a multi-sample cell for X-ray emission spectroscopy optimised for both tender and hard X-ray regions including An $M_{4,5}$- and $L_{2,3}$-absorption edges. Technical details can be found in (Schacherl et al., 2022b). The Np oxidation state was studied in the range from 1 to 209 ppm Np on illite by the advanced Np M_5-edge HR-XANES spectroscopic technique. The effects of beam-induced changes at temperatures of 141.2 ± 1.5 K and 300.0 ± 1.5 K were investigated. This study demonstrates that Np $M_{4,5}$-edge HR-XANES spectroscopy is applicable for samples with Np loadings obtained in batch sorption experiments. Experimental details can be found in (Schacherl et al., 2022a).

2.3.5.1 Spectral features of $Np(V)_{aq}$ and $Np(IV)_{aq}$ and sorbed Np species

Np(V) in an acidic to pH-neutral aqueous solution forms covalent bonded, trans-dioxo complex (NpO_2^+, neptunyl) coordinated by five water molecules weakly bound in the equatorial plane (Antonio et al.,

2001b; Ikeda-Ohno et al., 2008). Np(IV) in strongly acidic aqueous solution is bound to approximately ten water molecules (Antonio et al., 2001b; Gaona et al., 2012; Ikeda-Ohno et al., 2008). The Np M_5-edge HR-XANES spectrum of $Np(V)_{aq}$ shows a strong absorption peak at 3664.1 eV (*A*), also called white line (WL), and a distinct shoulder feature at 3667.15 eV (*B*) (Figure 22**A 22**).

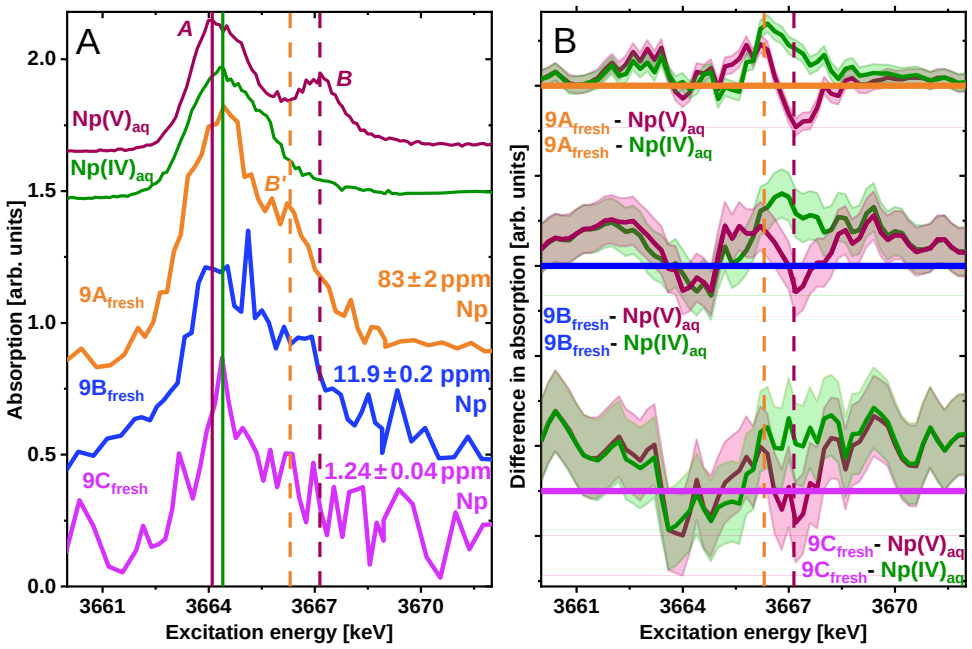

Figure 22. A) Np M_5-edge HR-XANES spectra of the aqueous references $Np(V)_{aq}$ and $Np(IV)_{aq}$ and the sorption samples $9A_{fresh}$ (83 ± 2 ppm), $9B_{fresh}$ (11.9 ± 0.2 ppm) and $9C_{fresh}$ (1.24 ± 0.04 ppm). The features A, B and B' are indicated. All spectra of Np-illite samples were recorded at 141.2 ± 1.5 K. B) Difference plots of the sample spectra in A), the shaded green and red areas correspond to a confidence interval of ± 2σ (Schacherl et al., 2022a).

The spectrum of $Np(IV)_{aq}$ exhibits a relatively broad and intensive WL with its maximum trending to slightly higher energies compared to $Np(V)_{aq}$ (*A*). The peak shows a sharp decrease in intensity in the higher energy region with no clear second peak. Usually, a higher energy position of peak *A* would be expected for a higher metal oxidation state. The shift to a lower energy for the higher Np oxidation state can be explained with the covalency of the trans-dioxo bond. It leads to charge transfer from the oxygen atoms to Np(V) resulting in a higher electron density on Np and increasing screening of the nuclear charge of $Np(V)_{aq}$ compared to $Np(IV)_{aq}$. Similar effects can be observed in Np L_3-edge XANES spectra, where also a higher energy position for the absorption edge would be expected for higher oxidation states (Schacherl et al., 2022a). Instead, the absorption edge of $Np(V)_{aq}$ is at the same position as the absorption edge of $Np(IV)_{aq}$ (Brendebach et al., 2009; Denecke, 2006; Gaona et al., 2012). Feature *B* can be assigned to electronic transitions of Np *3d*-electrons to the unoccupied σ-antibonding orbital of NpO_2^+ as identified for neptunyl, as well as uranyl and plutonyl, solid phases in (Vitova et al., 2015; Vitova et al., 2018; Vitova et al., 2017; Vitova et al., 2020). Therefore, this feature with strong intensity can be used to detect neptunyl species. The large ligand field splitting of the *5f* unoccupied orbitals leads to the well resolved peak *B* in the An $M_{4,5}$-edge HR-XANES spectra, which is characteristic for the actinyl series.

According to geochemical calculations, neither Np(IV) nor Np(V) precipitates should form under the chosen experimental conditions. Consequently, spectra for Np-illite samples represent exclusively Np species sorbed on illite surfaces. The spectrum of sample $9A_{fresh}$ (83 ± 2 ppm Np, Figure 22A) shows a distinct shoulder (*B'*). This shoulder shows an energy shift towards lower energies compared to feature *B* in the $Np(V)_{aq}$ spectrum. The energy splitting between features *A* and *B'* is approximately 0.85 eV smaller than between features *A* and *B* in $Np(V)_{aq}$. This trend is also well visible in the difference plot $\Delta(9A_{fresh}, Np(V)_{aq})$ (red spectrum) and $\Delta(9A_{fresh}, Np(IV)_{aq})$ (green spectrum) with a confidence interval of ± 2σ, respectively, marked in Figure 22B. The horizontal orange straight line represents $\Delta(9A_{fresh},$

$9A_{fresh}$). At the approximate energy position of shoulder *B'* (vertical orange dashed line), the difference plot $\Delta(9A_{fresh,}\ Np(V)_{aq})$ shows a maximum while a minimum occurs at the energy position for feature *B* (vertical dark red dashed line). This finding illustrates that the spectrum of $9A_{fresh}$ contains additional speciation information beyond the oxidation state. In detail, it indicates the decrease of the Np(V)-O_{ax} bond covalency for sorbed Np (Vitova et al., 2017) and reflects differences in the Np(V) bonding environment at the illite surface as compared to Np(V) in aqueous solution. Qualitatively, the relatively narrow WL feature shows that Np(V) is the predominant oxidation state in this sample. The interpretation of the slight trend to higher energies of feature *A* for Np-illite samples as compared to $Np(V)_{aq}$ still needs to be discussed (cf. vertical green line in Figure 22 as compared to the dark red line marking the WL position of the $Np(IV)_{aq}$ and $Np(V)_{aq}$ spectrum, respectively). This shift might be a consequence of Np(V) coordination to clay surface hydroxyl groups. However, the WL maximum lies close to that of the $Np(IV)_{aq}$ spectrum. Partial reduction of Np(V) on the illite surface as proposed in (Marsac et al., 2015) may, therefore, also explain the observed energy shift. This observation highlights the need for further X-ray spectroscopic studies on Np surface complexes. For quantitative speciation analysis, for instance using linear combination least squares fit analyses, precise and comprehensive analyses of appropriate reference systems need to be performed (Soderholm et al., 1999; Vitova et al., 2020). This will be subject to future studies (Schacherl et al., 2022a).

2.3.5.2 Detection limit estimate for speciation studies of Np sorbed on illite

The major components of air such as O_2 and N_2 absorb and strongly scatter X-rays with energies in the tender X-ray region (2000–5000 eV). Consequently, X-ray spectra at these energies are best recorded in vacuum. Furthermore, traces of Ar in sample containments should be avoided, since the Ar K-edge absorption energy is at 3206 eV, i.e., near the $M\alpha_1$ fluorescence energy of Np (3261 eV). The presence of Ar would result in a drastic reduction of intensity of both the incident X-ray beam and the emitted Np $M\alpha_1$ fluorescence. The investigation of samples with very low Np loading (1–80 ppm) was only possible in the present study by major improvements of the equipment, i.e. (1) a tight glove box filled with He enclosing the X-ray emission spectrometer; (2) the investigation of cooled samples by including a cryostat for tender X-ray energies in the experimental setup; and (3) a sample holder equipped with three thin Kapton windows (12.5 µm and 2×8 µm) with a new tightening concept. The experimental set-up is described in detail in (Schacherl et al., 2022b).

To determine detection limits for Np loading in the improved setup, highest comparability of the Np-illite spectra was necessary. This was achieved by the application of similar sorption conditions (pH 9, S/L = 2 g illite/L, 0.1 NaCl, sorption time = 11 days). Only the initial Np concentration was stepwise decreased by an order of magnitude each from sample $9A_{fresh}$ over sample $9B_{fresh}$ to sample $9C_{fresh}$. Consequently, this resulted in a stepwise decrease of Np loadings on illite. The spectra from the three samples are depicted in Figure 22A. Alongside feature *A,* the *B'* feature is clearly visible in the spectra and the difference plots, this indicates the predominance of Np(V) in both $9A_{fresh}$ (83 ± 2 ppm Np) and $9B_{fresh}$ (11.9 ± 0.2ppm Np) samples (cf. Figure 22B). The shift of feature *B'* to lower energies indicates a different Np speciation in $9A_{fresh}$ and $9B_{fresh}$ than in $Np(V)_{aq}$. The feature is less pronounced in $9B_{fresh}$, where the Np content is lower. By averaging two scans measured 10 h each, it was possible to record the spectrum of the $9C_{fresh}$ sample containing 1.24 ± 0.04 ppm Np (Figure 22A). The spectral shape is like $9A_{fresh}$ and $9B_{fresh}$. The spectrum of $9C_{fresh}$ exhibits a relatively narrow WL feature and a shoulder region, too. As expected, a significant σ_{noise} is present. The S/N was quantified with 9, much lower than the S/N of $9A_{fresh}$ (42) and $9B_{fresh}$ (15) (Table 27). The larger influence of noise is also visible in the larger ± 2σ confidence interval area in the difference plots. The detection limit criteria for any element or edge is S/N > 3. As a conclusion, the WL signal for Np at the M_5-edge of $9C_{fresh}$ with S/N equal to 9 and a Np loading of about 1 ppm is considered above the detection limit. However, based on the observable features and under consideration of the ± 2σ confidence interval in the respective difference plots, 1 ppm lies on the verge or shortly below the limit of Np loading, where an oxidation state or speciation study of Np sorbed on illite at the CAT-ACT beamline with the current set-up is possible. Nevertheless, it can be stated, that in comparison to previous studies(Arai et al., 2007; Bots et al., 2016; Combes et al., 1992; Elo et al., 2017; Fröhlich et al., 2012; Gaona et al., 2013; Gückel et al., 2013; Heberling et al., 2008;

Heberling et al., 2011; Marsac et al., 2015; Müller et al., 2015; Roberts et al., 2019; Scheinost et al., 2016; Smith et al., 2018; Virtanen et al., 2016; Wilk et al., 2005; Yang et al., 2015), the spectra in the present study are obtained for samples with a factor of 30 to 2000 lower Np loading (Schacherl et al., 2022a).

2.3.5.3 Elimination of beam-induced changes of Np oxidation state

Previously, the $Np(IV)_{aq}$ and $Np(V)_{aq}$ spectra were measured at the Np M_5-edge for samples with high Np concentrations (c(Np) = 2×10^{-2} mol/L) at room temperature. These measurements were recorded with a previous He-box configuration, under He atmosphere with higher air content. Chemical changes of the Np samples induced by irradiation were tested by recording quick HR-XANES scans (1 min/scan). Within this illumination time, no changes of the spectra indicating X-ray induced oxidation state variations of Np were found. This could be explained by the reduced intensity of the incident X-ray beam because of the high air content in the box encapsulating the spectrometer. Complementary, beam-induced changes in liquid samples were checked with Vis-NIR spectroscopy. The energy positions and intensities of the features in the Vis–NIR spectra are very sensitive towards changes of the Np oxidation state. The Vis-NIR measurements were performed for $Np(IV)_{aq}$ and $Np(V)_{aq}$ before and after HR-XANES experiments (Figure 24). Both sets of spectra show similar features, which is an additional strong indication, that beam-induced changes were avoided for these highly concentrated Np samples.

To successfully measure Np oxidation state in the low ppm range of Np, it was mandatory to reduce the amount of air in the box enclosing the X-ray emission spectrometer. As a result of this improvement, the emitted fluorescence photons were less attenuated. However, the intensity of the incident photon flux has also increased. Consequently, beam-induced changes of the Np oxidation state became visible in sorption samples measured at room temperature already after a few minutes of X-ray irradiation. The Np M_5-edge HR-XANES spectrum of sample $7A_{aged}$ recorded at 300.0 ± 1.5 K is shown in Figure 25.

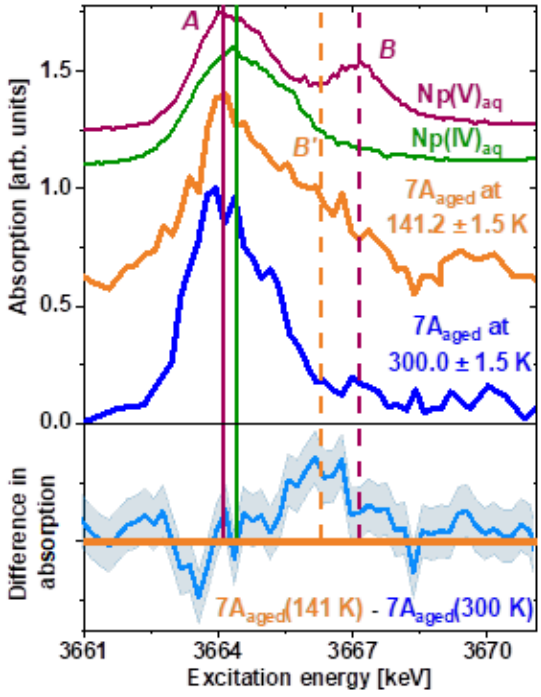

Figure 23. Np M_5-edge HR-XANES spectra of the aqueous references $Np(V)_{aq}$ and $Np(IV)_{aq}$, and sample $7A_{aged}$ at 141.2 ± 1.5K (54.6 ± 0.9 ppm) and at 300.0 ± 1.5 K. Below: Difference plot for $\Delta(7A_{aged}$ (141 K),$7A_{aged}$ (300 K)), the shaded blue area corresponds to a confidence interval of ± 2σ (Schacherl et al., 2022a).

The spectrum exhibits a relatively broad feature *A* and almost no shoulder *B'*, thus it resembles the spectrum of $Np(IV)_{aq}$. The disappearance of feature *B'*, typical for Np(V), after extended irradiation times is strongly suggesting the reduction of Np(V) to Np(IV). The beam-induced oxidation state change of Np

can be minimised by cooling the sample as demonstrated for sample $7A_{aged}$ in Figure 25. A narrow feature *A* and a shoulder feature *B'* are visible in the spectrum of the $7A_{aged}$ sample measured at 141.2 ± 1.5 K. The difference between the spectra of the sample $7A_{aged}$ measured at 141.2 ± 1.5 K and at RT is statistically significant as visualised by the peak in the difference curve in Figure 25 (cf. vertical dashed orange line). This finding demonstrates that sample $7A_{aged}$ measured at 300 K showed beam-induced changes of Np, which most likely caused reduction to Np(IV).

At the CAT-ACT beamline, the flux density was determined to be $(5.2 \pm 0.2)\times10^{10}$ ph/(s·mm^2) at 3664 eV incident energy. At 300 K, Wilk et al. (2005) found 78 ± 12% of Np(IV) in a NpO_2^+ control solution after X-ray irradiation. The X-ray irradiation time per sample is unknown for Wilk et al. (2005), but the flux density could be estimated from the beamline characteristics (Stojanovic, privat comm.) and amounted to about 5×10^{10} ph/(s·mm^2). This value is comparable with the photon flux in the experiments described in the present study. The present observations are also consistent with the studies of Göttlicher et al. (2018) and Steininger et al. (2018). They found that Cr(VI) sorbed onto kaolinite was reduced by X-ray radiation to lower Cr oxidation states, since the Cr(VI) signal decreased, during irradiation at 270 K with a photon flux of 1.5×10^{11} ph/(s·mm^2). Beam-induced changes could however be prevented at temperatures below 180 K. The authors found, that for photon flux densities higher than 10^{12} ph/(s·mm^2), beam-induced changes of sorbed Cr(VI) were inevitable over time even at 15 K. These findings are important to consider when investigating similar samples at high photon flux beamlines.

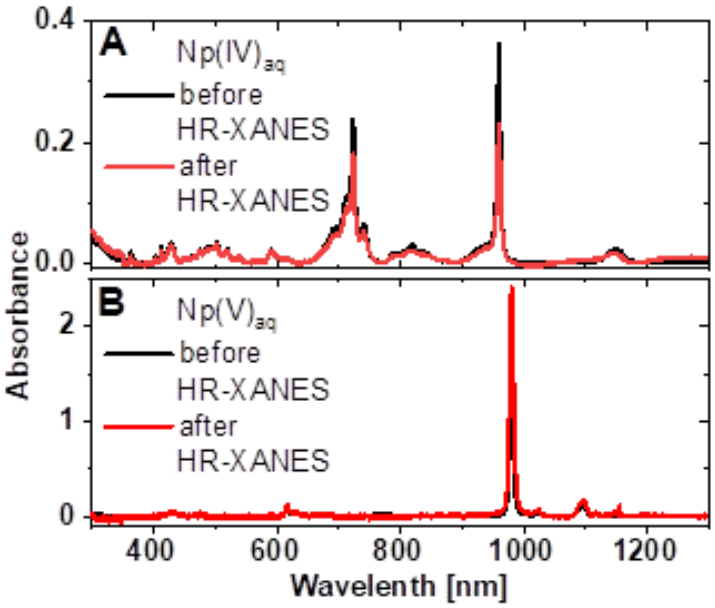

Figure 24. Visible near-infrared spectra of A) $Np(IV)_{aq}$ and B) $Np(V)_{aq}$ samples measured before and after HR-XANES spectroscopy (sample volume: 200 µL, cuvette path length: 2 mm) (Schacherl et al., 2022a).

The occurrence and extent of beam-induced changes of samples depend on many factors, not only on the photon flux as shown by Van Schooneveld and DeBeer (2015). In an extensive study, they showed that there is no exclusive dose-photoreduction correlation for Fe and Mn L-edge (640–720 eV) investigations model systems such as $K_3[Fe(CN)_6]$ and $KMnO_4$. The authors discussed the irradiation effects on different oxidation states and absorption edges of Fe and Mn as well as the combination of factors like temperature, pressure, and sample conditions. Also, Göttlicher et al. (2018) and Steininger et al. (2018) highlighted the importance of the sample matrix, for instance, cellulose being more susceptible to beam-induced changes than boron nitride. Based on these results, the selection of a representative reference system, where beam-induced changes can be monitored, has high importance. In the present study, $9A_{aged}$ (209 ± 4 ppm Np) was chosen for beam-induced damage tests at 141.2 ± 1.5 K. The matrix and measurement geometry of this sample was consistent with all other

sorption samples analysed in this study. Repetitive measurements on the same sample spot showed no substantial changes or trends in the spectra within the 2σ confidence interval calculated for each point considering 9 single spectra (Figure 20). This demonstrated that no beam-induced changes were caused in this sample.

A total irradiation time of 240 min was covered with these tests. For very dilute samples, where even longer scan times were needed, the total scan time was divided in at least two equally long scans. The raw data of these scans were thoroughly compared for any changed features in the spectra before averaging. As a result, beam-induced changes could be ruled out in this system at 141.2 ± 1.5 K for up to 20 h total irradiation time. The σ_{noise} in the single spectra were, in accordance with the central limit theorem, larger than the σ_{noise} of the final averaged spectrum. These averaged spectra with their individual σ_{noise} are compared in this study (Figure 23**,** Figure 25**,** Figure 26 black line), they should and were not compared to single scan spectra (Schacherl et al., 2022a).

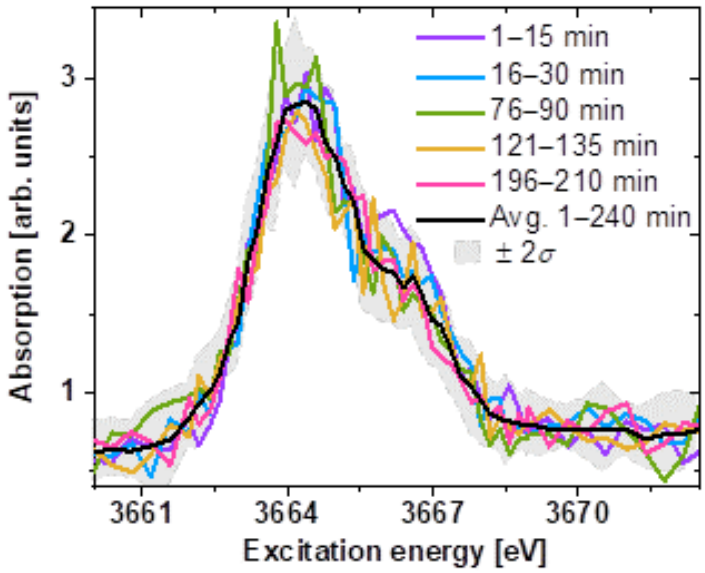

Figure 25. Test for beam-induced changes of Np oxidation state in sample $9A_{aged}$ (209 ± 4 ppm) (single scans) as a function of X-ray irradiation duration at 141.2 ± 1.5 K. The average of all single scans is shown in black with the corresponding ± 2σ confidence interval calculated for each individual data point (grey area) (Schacherl et al., 2022a).

2.3.5.4 Potential for further optimisation

The presented results using the current set-up display a significant improvement for the An $M_{4,5}$-edge HR-XANES spectroscopy on dilute samples. However, there is still potential for an increase of signal to noise ratio, which can lead to reliable oxidation state analyses for 1 ppm Np or even lower Np loadings. For instance, the X-rays elastically scattered from the sample and the characteristic fluorescence emitted from other elements present in the clay can be minimised in the detected signal. How both effects influencing the Np XANES spectrum shall be discussed briefly. Illite du Puy contains significant amounts of potassium (7.82 wt.% K_2O (Montoya et al., 2018)). The K-edge absorption energy is at 3607.4 eV. Figure 26A depicts the $K\alpha_{1,2}$ characteristic fluorescence lines of sample $5A_{aged}$. These lines have 50 eV energy difference compared to the Np $M\alpha_1$ fluorescence emission and can be very well separated by the X-ray emission spectrometer (energy resolution, $\Delta E \approx 1$ eV (Vitova et al., 2017), cf. Figure 26A). However, a small fraction of the K Kα-fluorescence, in every measurement, directly reaches the detector (green arrow in the inset of Figure 26B). Unfortunately, the Np Mα and K Kα fluorescence signals cannot be resolved by a solid-state detector (ΔE> 100 eV) used in the present study. For samples with high analyte loadings this unwanted, interfering signal is negligibly small, but for low analyte loading it can have a considerable effect. This is visible in Figure 26B, where the fluorescence spectrum of sample $9A_{fresh}$ measured by the detector for excitation energies (E_{inc}) well above or below the Np M_5 absorption edge is shown. The elastically scattered incident beam contributes, too (blue

arrows in the inset of Figure 5B). These effects are particularly significant for low loading samples with relatively high fractions of interfering elements (e.g., K in the case of Np). Then, the intensity of the direct emission from the interfering element is significant compared to the emission intensity from the element of interest. One solution for minimising contributions of elastic scattering and fluorescence signals from other elements than Np would be to mount a slit with defined width in front of the detector. Besides the detector modification, the sample holder geometry can be improved. So far, the irradiated sample areas were only marginally larger than the beam size, which led to signal loss due to minor beam instability. This can be overcome with sample holders with larger sample areas.

An additional possibility for improvement of the signal to noise ratio of Np M_5-edge HR-XANES spectra lies in the measurement parameters. As it is performed in the present study, the XANES spectra are usually recorded by positioning the analyser crystals at the maximum intensity of the normal emission line. This is identified as the maximum of the emission intensity at incident energies above the absorption edge (E_{inc} = 3700 eV). However, higher intensity is often observed at the absorption edge itself at a different emission energy (known as the resonant emission energy). If the resonant emission energy is used to record the Np M_5-edge HR-XANES, it can improve the count rate by approximately 30% (exemplary for sample Np-cp) (Vitova et al., 2020). Before this can be applied for samples with low Np loading, the energy positions of the intensity maxima of the resonant emission for the different Np oxidation states must be better understood and a procedure for measurement of references has to be developed.

As a last point, analyser crystals with 0.5 m bending radius, as opposed to 1 m in the current study, can be applied. This would increase the photon collection efficiency. Since the Bragg angle using the Si(220) reflection of the crystals is large (81.9°) and therefore favourable for recording Np M_5–edge HR-XANES, no substantial loss of spectral energy resolution is expected (Schacherl et al., 2022a).

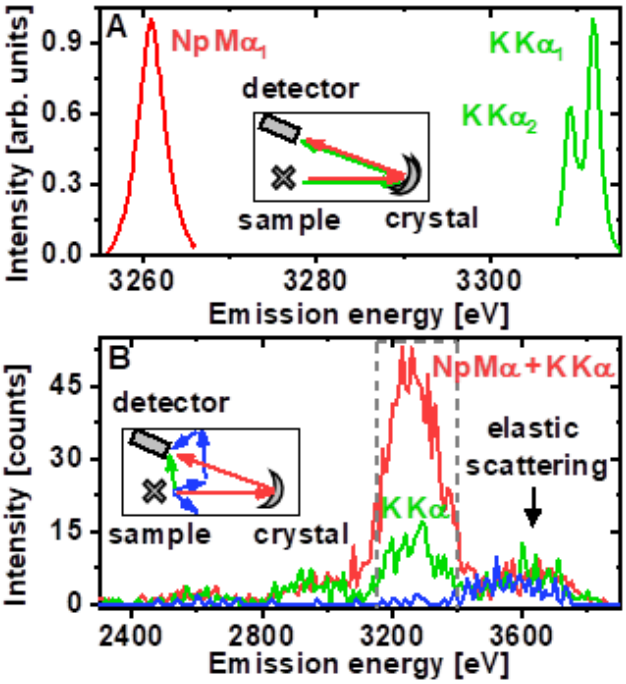

Figure 26. A) Np Mα$_1$ of sample Np(V)-cp (red) and K Kα of sample 5A$_{aged}$ (green); B) The solid-state detector signal collected for 90 s using excitation energy above (red, E_{inc} = 3664 eV) or below (green, E_{inc} = 3654 eV) the Np M_5-edge and below the K K-edge (blue, E_{inc} = 3590 eV). The spectra are recorded of sample 9A$_{fresh}$ (red and green) and of the Al_2O_3 sample holder (blue). The insets depict the set-up and origin of the predominant signals for samples with high Np/K loadings (A) and low Np loadings (B). The region of interest (ROI) integrated to obtain the spectra is marked with grey dashed lines (Schacherl et al., 2022a).

2.4 Atomistic simulations methods applied to iron oxides [HZDR]

Density functional theory (DFT) based atomistic simulations were applied to reveal geometrical parameters and the mechanism of Tc uptake by iron oxides.

DFT calculations for TcO_2 and ReO_2 crystal structures. The initial TcO_2 and ReO_2 structures were constructed from crystallographic data for α-ReO_2 (Ferreira et al., 2009) (monoclinic, P21/c), β-ReO_2 (Magneli, 1957) (orthorhombic, Pbcn), and γ-ReO_2 (Ivanovskii et al., 2005) (tetragonal, P42/mnm). The equivalent TcO_2 structures were obtained simply by replacing the Re atoms with Tc. Finally, the tetragonal phases (γ-TcO_2 and γ-ReO_2) were duplicated in the c direction (1×1×2 supercells), so that all cells would contain four TcO_2 or ReO_2 formula units. Subsequently, the atomic coordinates and lattice vectors were fully optimized using the PBE (Perdew et al., 1996) density functional with numerical atomic orbitals (NAOs) augmented with a triple-zeta polarized (TZP) set of Slater-type basis functions; relativistic effects were included via the zeroth-order regular approximation (ZORA) (Philipsen et al., 1997). These calculations were conducted with the AMS/BAND (Philipsen, 2020; te Velde et al., 2001) program, using regular k-space grids with quality set to "Good" and default convergence criteria.

DFT calculations for $TcO_2{\cdot}2H_2O$ infinite chains. The initial $TcO_2{\cdot}2H_2O$ chains were constructed by extracting a single chain of edge-sharing TcO_6 octahedra from each TcO_2 crystal phase and saturating the O atoms with H according to the following approach: terminal O atoms were converted into H_2O ligands and bridging O atoms were left unprotonated, resulting in $(Tc(\mu\text{-}O)_2(OH_2))_n$ chains. Then, the atomic coordinates and lattice parameter of each structure were fully optimized using the method described above for the crystal structures, supplemented with Grimme's D3 corrections (Grimme et al., 2010) to improve the description of dispersion interactions with OH and H_2O groups. Like for the crystal structures, these calculations were conducted with the AMS/BAND program, using regular k-space grids with quality set to "Good". Note that these systems are periodic only along the chain direction.

DFT Single-point calculations. Energies and electronic properties were calculated for the optimized structures with the same methods used in the preceding geometry optimizations, except for a denser k-space grid (quality set to "VeryGood"). For comparison, single-point calculations were also carried out within the FHI-aims program (Blum et al., 2009), using the PBE (Perdew et al., 1996) and HSE06 (Heyd et al., 2003; Heyd et al., 2006; Krukau et al., 2006) density functionals with a "tier 1" set of atom-centered NAO basis functions; relativistic effects were described with the "atomic ZORA" approach (Blum et al., 2009); for the $TcO_2{\cdot}2H_2O$ infinite chains, the Tkatchenko-Scheffler (TS) method (Tkatchenko and Scheffler, 2009) was used for the dispersion interactions.

DFT calculations for the Fe-containing Tc-doped magnetite species. The energies of the optimized structures were also calculated employing the Hubbard correction to the PBE functional (PBE+U) with a Hubbard parameter U = 5.3 eV. The initial spin configurations of the magnetite and derived species were modified in every simulation by flipping the spins of the tetrahedral Fe^{III} sites to facilitate the development of a ferrimagnetic arrangement during the calculations.

DFT calculations for the interaction of pertechnetate and TcO_2 x H_2O chains with the magnetite surface were carried out with the HSE06 (Heyd et al., 2003; Heyd et al., 2006; Krukau et al., 2006) hybrid exchange-correlation functional using the CRYSTAL17 package (Dovesi et al., 2018). This methodology has been shown to give good description of structural, electronic, and magnetic properties of magnetite systems (Liu and Di Valentin, 2017). The Kohn−Sham orbitals were expanded in Gaussian-type orbitals: the all-electron basis sets are H|511G(p1), O|8411G(d1), Fe|86411G(d41), and Tc|976311(d631f1) according to the scheme previously used for Fe_3O_4(Bianchetti and Di Valentin, 2022; Liu and Di Valentin, 2017, 2018, 2019). The irreducible Brillouin zone was sampled with a 3×3×1 k-point grid generated with the Monkhorst-Pack scheme (Monkhorst and Pack, 1976). The convergence criterion of 4.5×10^{-4} hartree/bohr for atomic forces was used during geometry optimization and the convergence criterion for total energy was set to 10^{-6} hartree for all the calculations. All structures were constructed in such way as to keep inversion symmetry (e.g., by adding adsorbate molecules in specific locations above and below the slab models) to minimize the appearance of artificial dipole moments.

3. Reactivity of redox-active elements towards reference minerals [All groups]

The experimental work conducted in the Task 3.0 of WP-FUTURE was motivated by two main research questions:

- Can the structural Fe (II) present in phyllosilicate-type and smectite clay minerals reduce selenium, technetium or uranium?
- How do newly formed metal corrosion products affect radionuclide retention?

To elucidate different processes that can lead to the reduction of radionuclides under repository in situ conditions, the experimental conditions and materials have been adapted and/or simplified when necessary with respect to specific radionuclides and their known affinity to the mineral phases.

3.1 Se reactivity

3.1.1 Towards phyllosilicates [TNO, PSI, BRGM, CIEMAT]

In this section, Se reactivity is investigated for a variety of phyllosilicates having contrasting amount of total Fe and Fe speciation, either incorporated in their layers, or adsorbed at the surface. The overarching goal being to determine (i) the mechanism of interaction between Se and Fe-bearing phyllosilicates, and in particular to distinguish between potential adsorption or irreversible (redox) interaction, (ii) if there is a relationship between total Fe, redox-active Fe, Fe structural location, or (and) Fe speciation on Se uptake capacity and mechanism, and (iii) to determine the retention coefficient and the nature of the reaction product.

[PSI] Se sorption experiments were performed on smectites reduced to different Fe(II)/Fe(III) ratios (Table 14).

Table 14. Fraction of Fe(II) and Fe(III) w.r.t. Fe_{tot} measured by MEO/MER in the different smectites samples.

Clay	Fe(II)	Fe(III)
High-red NAu-2	0.58	0.12
Low-red NAu-2	0.19	0.45
Native NAu-2	0	1
Red SWy-2	1	0
Native SWy-2	0	1
Red STx-1	0.89	0
Native STx-1	0	1

Figure 27 shows the Se pH dependent sorption on native NAu-2 and on the four reduced clays after 7 days. Selenite sorption decreases from log $R_d \approx 2.5$ mL/g as the pH increases from 4 to 9. Both native and reduced clays have similar sorption tendency. Figure 27b shows the sorption isotherm of native and reduced clays at pH 5-6 after 7 days in solid symbols. Below an equilibrium concentration of 10^{-5} M, sorption shows a linear decrease with decreasing selenite concentration. Above the equilibrium concentration of 10^{-5} M, however, sorption rate decreases and reaches a plateau. Both sorption edge and sorption isotherm of native and reduced clays are in a good agreement with the data published by Missana et al. 2009 on native Na-smectite. After 7 days, no significant disparity in sorption behavior was noticed between native and reduced clays. However, sorption after one month is higher than after 7 days, indicating that sorption kinetics is involved in the sorption process. Therefore, sorption kinetics experiments on reduced clays were carried out at pH of 5 and an initial Se concentration of 3×10^{-5} M.

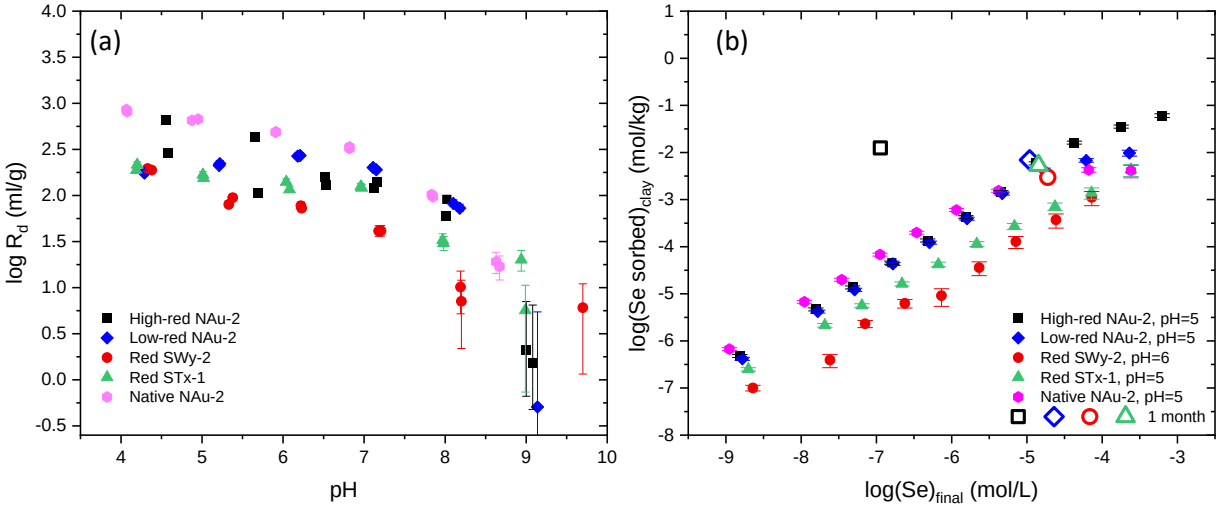

Figure 27. Selenite sorption on high-red NAu-2, low-red NAu-2, red SWy-2, red STx-1, and native NAu-2 at S/L of 2 g/L, 0.1 M NaCl. (a) Sorption edges at $[Se]_{init}$ = 6×10-8 M after 7 days, (b) Sorption isotherms at pH 5 and 6, after 7 days (solid symbols) and 1 month (hollow symbols).

Figure 28 shows the Se sorption behaviour on reduced clays after 4 hours to 5 months. The sorption of selenite on reduced clays increases with longer contact time, indicating a kinetically controlled sorption reaction, consistent with previous observations (Charlet et al., 2007a; López de Arroyabe Loyo et al., 2008; Myneni et al., 1997). A divergence was observed between High-red NAu-2 and the other reduced clays. High-red NAu-2, characterized by the highest Fe(II) wt% (11.4 wt%), exhibited higher sorption, with complete sorption of selenite achieved after 1 month. Low-red NAu-2 and red STx-1 displayed lower sorption. Red SWy-2 also exhibited lower sorption, which gradually increased over a period of 5 months without reaching a plateau.

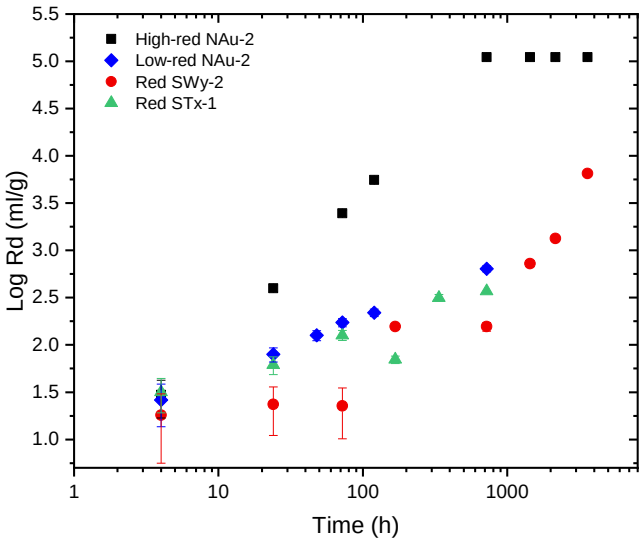

Figure 28. Selenite sorption kinetics on high-red NAu-2, low-red NAu-2, red SWy-2, and red STx-1 at S/L of 2 g/L, $[Se]_{init}$ = 3×10^{-5} M, and 0.1 M NaCl.

EXAFS measurements were performed on red-SWy to quantify the reduction degree of selenium and to identify the Se surface species as a function of time. Figure 29 display the XANES and EXAFS spectra of the kinetics series (from 24h to 3600h) obtained for Se reacted with red SWy-2 as well as the reference spectra for Se(IV)), red Se(0) and grey Se(0) retrieved from previous publications (Charlet et al., 2007b; Scheinost and Charlet, 2008; Scheinost et al., 2008). The samples of the shortest reaction time (24 h) shows the Se(IV) white line, which then gradually transforms into the Se(0) white line.The EXAFS spectra were successfully fitted with the linear combinations of three components, amorphous

red Se(0), trigonal Se(0) grey and adsorbed Se(IV). Se initially sorbs as Se(VI) and is then reduced to Se(0) red and finally transformed into Se(0) grey. No $FeSe_2$ could be identified.

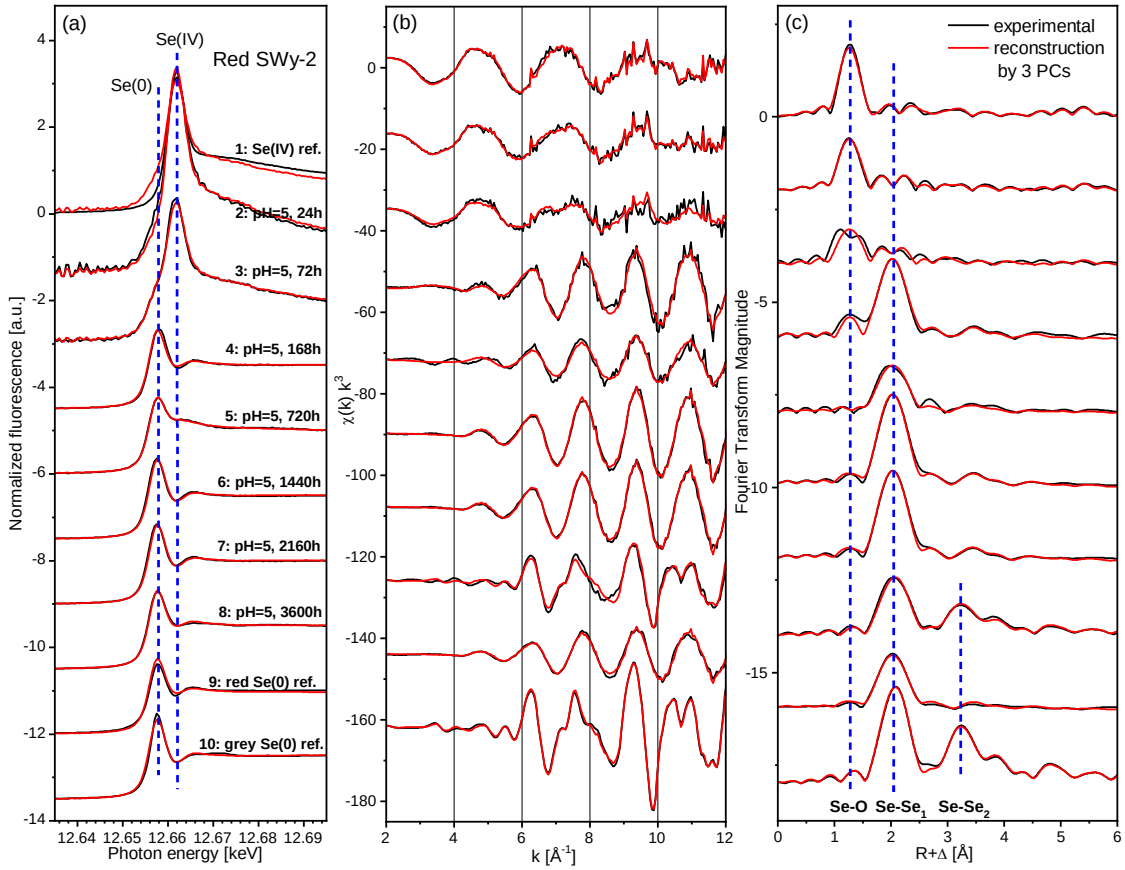

Figure 29. Se K-edge EXAFS of selenite sorption kinetics on red. Swy-2 at S/L of 2 g/L, $[Se]_{init}$ = 3×10^{-5} M, 0.1 M NaCl, and pH 5. Samples were chosen from the kinetics experiment (Figure 28). The experiment data is in black solid line, the red solid line represents the reconstruction of the spectra with three components: Se(IV), red Se(0), and grey Se(0), and the blue dash line shows the position of each peak. (a) Normalized Se absorption edge (XANES), (b) k^3-weighted EXAFS $\chi(k)$ function, (c) k^3-weighted EXAFS Fourier transform magnitude.

[TNO]

In addition to smectites, other types of clay minerals can be present in the host rock. In section B.I.2, it was shown that almost all Fe in smectites was redox-active when measured by mediated electrochemical reduction/oxidation, but this percentage was much lower for mixed layer illite-smectites, illites, chlorite and glauconite. Batch experiments with selenite and different types of reduced clay minerals were performed to assess the retention and potential reduction of selenite in relation to commonly occurring clay minerals. The following dithionite-reduced clay mineral standards were studied: illites IMt-1.d and Fithian illite.d, interstratified mixed-layered illite-smectites ISCz-1.d and RAr-1.d, glauconite (Rarecourt, France, GRf.d), and chlorite (Santa Ana, New-Mexico, USA, CNm.d) (see section B.I.2). Clay mineral samples ISCz-1 and RAr-1 were also reduced by mediated electrochemical reduction (ISCz-1.m, RAr-1.m) (see section B.I.2). The clay minerals were suspended in 0.1 M NaCl at pH7 with a loading of 10 g/L and a selenite concentration of 150 µM.

Selenite concentrations in solution decreased over time and did not yet reach equilibrium after 1300 hours. Rd values after 1300 hours ranged from 53 mL/g for ISCz-1 to 118 mL/g for chlorite. The speciation of Se on the clay minerals was assessed by XAS. In Figure 30, XANES and EXAFS spectra are plotted for the different types of clay minerals from the selenite batch experiment after 3 months. The spectra were successfully fitted with three components amorphous red Se(0), trigonal Se(0) grey

and Se(IV) adsorbed on oxidized smectite. On clay mineral samples reduced by MER, Se was not entirely reduced but present as both adsorbed Se(IV) and amorphous red Se(0). Se on all clay mineral samples that were reduced by dithionite, except for glauconite, was entirely reduced to trigonal Se(0) grey which formed small 100 nano- to 2-micrometer sized needles (Figure 31). Se on glauconite was entirely present as amorphous red Se(0). The glauconite sample and MER-reduced clay minerals contained both redox-active Fe(III) and Fe(II), while all other dithionite-reduced clay minerals only had redox-active Fe(II) and negligible redox-active Fe(III). The presence of redox-active Fe(III) together with a limited amount of redox-active Fe(II) in the clay mineral samples appears to result in a delay of selenite reduction or to limit the extent of reduction, compared to the samples containing only redox-active Fe(II). Also, the transformation of amorphous red Se(0) to Se(0) grey, as was observed in the SWy-1 batch experiment, seems to be either delayed or inhibited in the clay mineral samples with both redox-active Fe(II) and Fe(III). In conclusion, different types of clay minerals, such as illite, mixed illite-smectites, chlorite and glauconite, that contained redox-active Fe(II), measured by mediated electrochemical oxidation, were able to reduce selenite to Se(0); the extent of selenite reduction and the form of Se(0) (amorphous or trigonal) varied and seemed to have a relation with the presence of redox-active Fe(III) in addition to Fe(II).

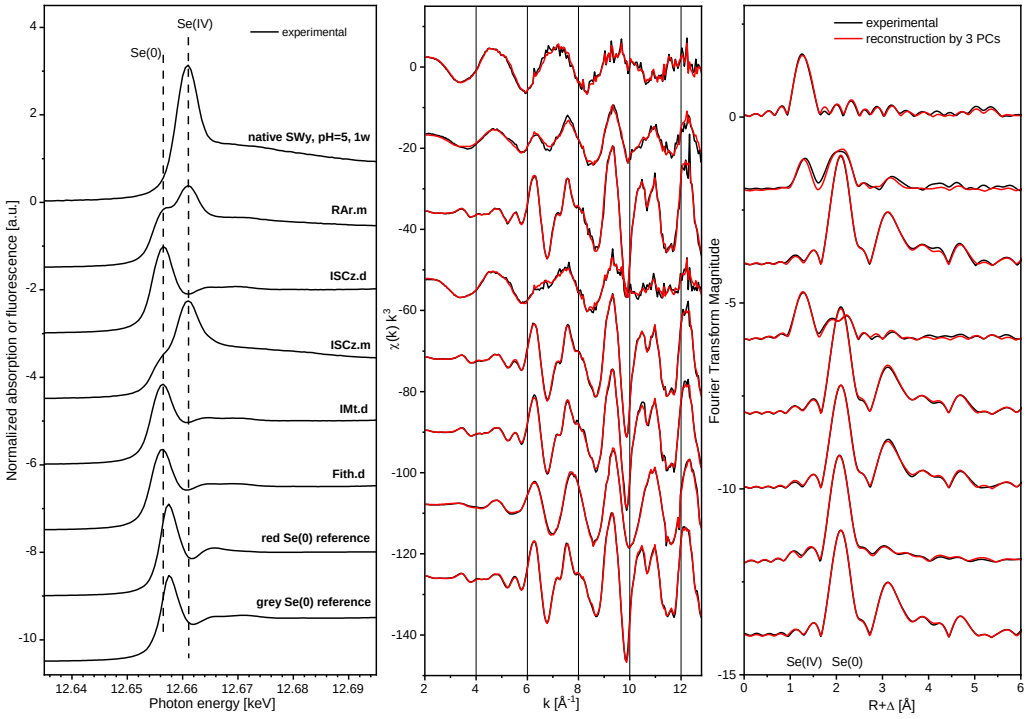

Figure 30. Selenium K-edge XANES and EXAFS spectra measured in different types of clay minerals from the selenite batch experiments and the three standard spectra (red Se(0), grey Se(0) and Se(IV)).

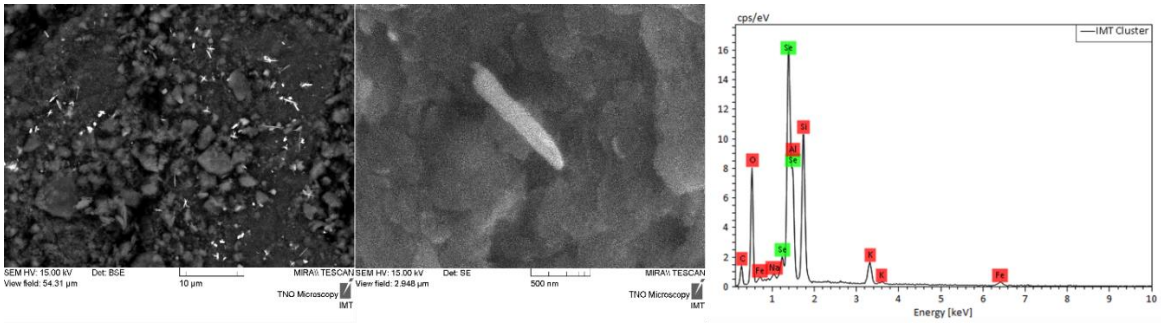

Figure 31. Left and middle: SEM images of dithionite-reduced IMt-1 from the selenite batch experiment after 3 months. Right: EDX spectrum of needle shaped particle (spot size around 0.1 µm).

[CIEMAT] carried out $^{75}Se(IV)$ sorption studies on Fe-rich smectites, under oxic (Task 2.1) and anoxic conditions (Task 3.0). The main results obtained in the project are reported in (Maes et al., 2023). Comparatively, selenium sorption as a function of pH was very similar in raw and ferric nontronite, but differed of ferrous nontronite, being higher the retention at acidic pH and slightly lower for pH > 6.

3.1.2 Towards magnetite [ISTerre, HZDR]

In this section, Se reactivity towards magnetite is investigated with a variety of chemical and physical methods, including synchrotron X-ray absorption spectroscopy. Like the work conducted with phyllosilicates in the previous section, the main goal was to determine the mechanisms of interaction, including determining if sorption is related to adsorption or redox phenomena, and to determine the nature of the reaction product, as well as chemical factors influencing the interaction between Se and magnetite.

[ISTerre]

Selenium is a highly mobile and soluble radionuclide in its high oxidation states, selenate ($Se(VI)O_4^{2-}$) and selenite ($Se(IV)O_3^{2-}$), but mostly insoluble in its various lower oxidation states (Se(0), $FeSe_2$, FeSe, oxidation states which are hard to differentiate by standard XANES (Lenz et al., 2008; Scheinost et al., 2008) as well as by HERFD/RIXS, as their corresponding maximum energy peak lie within 1 eV difference).

The reactivity of Selenium (VI) towards nanomagnetite was investigated in a series of experiments conducted at constant pH (with the magnetite pre-equilibrated for 96h at the given pH for a long time before addition of Se) and in a glovebox (with pO2 < xx ppm). Sorption experiments of selenate on magnetite were performed in glass bottles at room temperature in an Ar-filled glovebox. The concentration of dry magnetite in four 100 mL batches was fixed at 10 g/L in 0.1 mM NaCl background electrolyte. Due to published stronger selenium adsorption on magnetite in acidic conditions, pH 5 and 7 were selected for comparison. The acidity of the initial suspensions was adjusted during 96 h by adding drops of 0.1 M HCl or NaOH stock solutions, until the pH was not drifting from the desired value by more than 0.2 unit within 24 h. After this equilibration step, aliquots of Se(VI) stock solution were added to obtain a total target concentration of 8.6 mM. This should cover 100% of the [-Fe-OH] surface reactive sites, as calculated from the BET-determined specific surface area values and the theoretical crystallographic site density of magnetite, 8 sites/nm^2.

In the absence of the values of real concentrations of selenate in the underground repositories, the concentration of selenium was chosen so (i) the solutions are undersaturated with respect to any Fe(II)−Se(IV) phases, and so they are high enough to be observed via the physicochemical characterization tools used here. The addition of Se(VI) to the magnetite suspension stabilized at pH 5 resulted in an increase in the pH to 5.4, which was immediately readjusted to pH 5.0. No change in pH was observed upon the addition of Se(VI) to the magnetite suspension stabilized at pH 7. The pH of the suspensions was monitored and readjusted, if necessary, throughout the experiment. This addition of acid did not modify significantly the solid-to-liquid ratio in the system (less than 1%). The two reactors were placed on a rotary shaker, and 5 mL aliquots of the suspension were sampled at selected time intervals. The solid was isolated by magnetic separation, dried using a vacuum filtration system (0.22 µm), and used for further X-ray absorption spectroscopy (XAS) and Mössbauer spectroscopy, TEM, and XRD characterization. The liquid was filtered through a syringe filter (0.22 µm) and used for ICP-AES, IC, and Eh analyses.

Results have been described in detail in Poulain et al. (2022) and are just summarized below. The results of the Se(VI) sorption experiments at pH 5 and 7 are given in Figure 29. Se(VI) uptake was fastest during the first 240 h in the two experimental series, with the rate depending on the solution pH, as already observed previously. During this time, 43% of the selenate was removed from the solution at pH 5, in contrast with only 22% removed at pH 7. Thus, sorption of Se(VI) is observed to be much larger at pH 5 than at pH 7 (Figure 29). The uptake stagnated after ~1000 h for both pH values. After the first 240 h, a plateau (within analytical error) was observed at pH 7, which would correspond to about 1.5

Se(VI) molecules/nm^2. At pH 5, the removal process continued but at a much lower rate, reaching 53% after 3600h, equivalent to about 4.2 Se(VI) molecules/nm^2. This indicates that the theoretical sorption capacity (8 sites/nm^2) calculated for [Fe-OH] groups on the {111} crystallographic faces of magnetite was only partially reached, with a level of 53% at pH 5 and 22% at pH 7. On the other hand, a 28 molecules/nm^2 coverage could be reached if inner-sphere complexes with bidentate ligands are formed, these would account for 8.4 Se(VI) molecules/nm^2, a value very close to the theoretical site density.

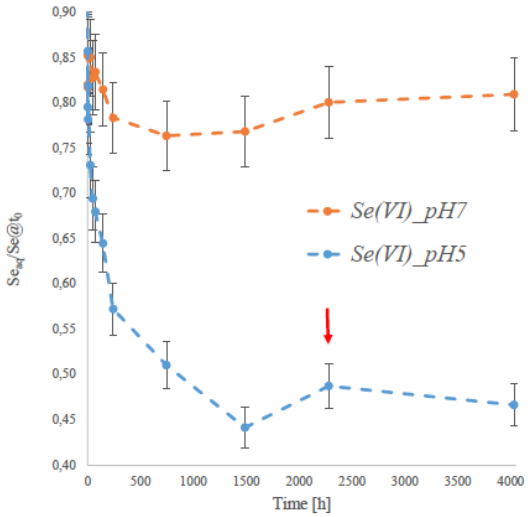

Figure 32. Sorption kinetics of Se(VI) observed in batch experiments. Error bars represent 5 % error of the ICP-AES measurements.

Aqueous Fe(II). At pH 7, the concentration of Fe(II)$_{aq}$ stayed below 0.01 mmol/L during 4000 h, so we could assume that the magnetite was pure at t_0 (as confirmed by Mössbauer spectrometry). In contrast at pH 5, after injection of selenate and throughout the 4000 h of the sorption experiments, a re-adsorption of the Fe(II) was observed, with an initial value of 1.87 mmol/L measured after 0.17 h of the reaction and a practical depletion from the solution after ~1000 h, the time at which the selenate removal was observed to stagnate as well (see Figure 32). While the re-adsorption of Fe(II)$_{aq}$ on magnetite is not favoured at pH 5 due to the positively charged mineral surface, the presence of Fe(II)$_{aq}$ may catalyse changes in the chemistry of Se(VI), via the formation of ternary surface complexes. To test this hypothesis, a linear plot was performed, which reveals indeed a co-removal dependency between Se(VI) and Fe(II)aq (Figure 33). The slope of the curve indicates that ~0.5 mol of Fe(II) is removed from solution per one mol of Se(VI). The initial ratio nFe(II)$_{aq}$/nSe(VI)$_{aq}$ in the solution was 0.3:1. Note that a reduction of selenate to selenite by the oxidation of Fe(II) to Fe(III) would require a ratio of 2:1 (and even higher for reductions of selenite to Se(0) or Se(-II)), so the observed value of 0.5:1 points to a completely different, secondary process involving the solid phase. Extrapolation of the co-removal results allowed the estimation of an initial aqueous iron concentration at t_0 equal to 2.4 mmol/L, corresponding to the 5.6% of maghemite initially present (before selenate injection). This corresponds to about one monolayer of maghemite for the averaged 15 nm diameter spherical particles, so that electron exchange between the surface and the core of the magnetite should still be possible.

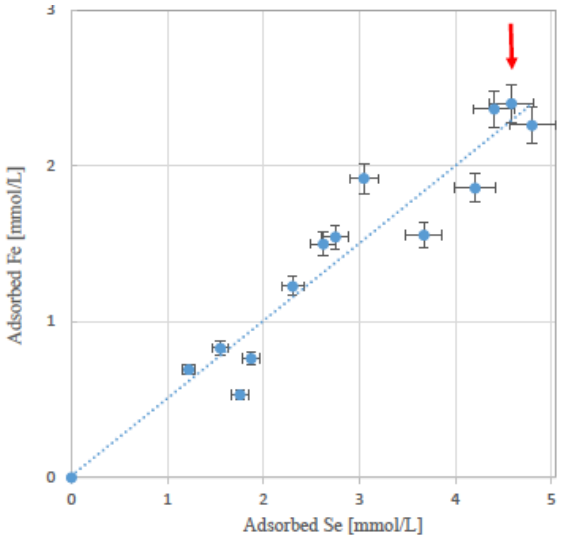

Figure 33. Linear dependence between Se(VI) and Fe(II) sorption observed in Se(VI) adsorption experiment at pH 5. As the Fe(II) first measurement was done at 10 min, concentration at time 0 was estimated by interpolation of the linear fitting.

Se(VI) Reduction: XAS and STEM. The temporal evolution of the selenium speciation on magnetite at pH 5 and pH 7 was determined by Se K-edge XANES and EXAFS using iterative target transformation factor analysis (ITFA). Both datasets (XANES and EXAFS) were subject to the ITFA independently, yielding similar results, with relative deviations below 10% (see the XANES and EXAFS results in Figure 34).

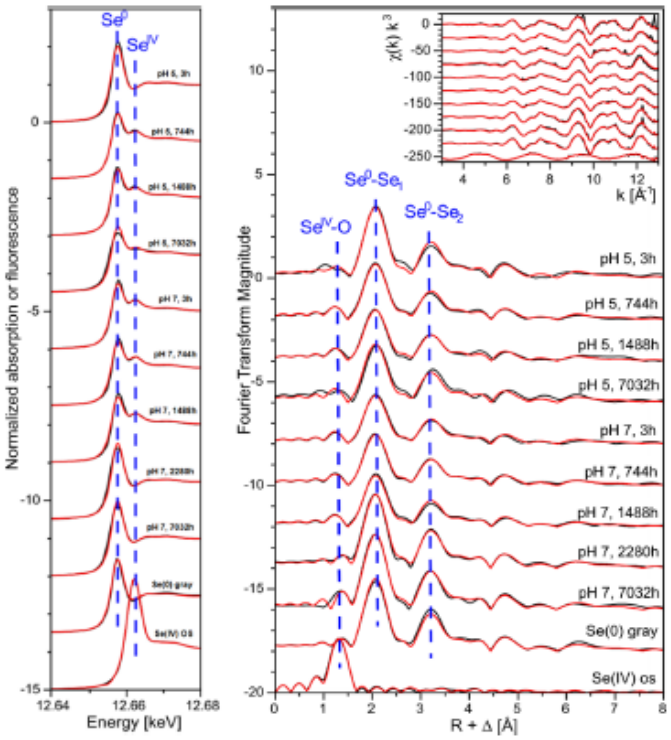

Figure 34. Selenium K-edge XANES (left) and EXAFS (right) spectra of the two time-series of Se(VI) experiments at pH 5 and 7 and the two standard spectra (grey Se(0) and Se(IV) outer-sphere sorption complexes (OS)). Inset (right): black lines, experimental data; red lines, reconstruction by two components.

Both XANES and EXAFS spectra collected for selected solid samples from the two experimental series were successfully fitted with two components: trigonal Se(0) grey and outer-sphere aqueous Se(IV)

(Figure 34). The EXAFS data confirm the presence of the grey elemental form (in contrast to amorphous, red Se(0)) and show even more clearly in the XANES spectra the presence of an oxygen shell indicative of Se(IV). Although the fit gives a good result with the Se(IV) outer-sphere reference, the low amount of Se(IV) in the samples makes it difficult to ascertain if a second shell is present. The presence of inner-sphere complexes, as described by Missana et al. (2009), cannot therefore be excluded. While these two oxidation states have also been reported as reduction products of selenate by magnetite and green rust, numerous studies reported in literature show that selenite can be immobilized by iron-containing minerals in the form of stronger inner-sphere (creation of covalent of ionic bonds) and/or weaker outer-sphere (electro-static-driven sorption) complexes, depending on the experimental conditions.

Initial Se(VI) was not detected on the solids, so all selenates must have been reduced by electrons from structural Fe(II) in magnetite (at pH 7) or from re-adsorbed Fe(II) (at pH 5); otherwise, the weakly adsorbed Se(VI) would have been removed during filtration.

In conclusion, XAFS data demonstrate at pH 7, a slow kinetics formation of Se(0) as well as the formation of an oxidized maghemite layer. In contrast, at pH 5, the additional presence of $Fe(II)_{aq}$, released during magnetite pre-equilibration and dissolution, is shown to lead to Se(0).

TEM-HAADF images and STEM-XEDS maps (Figure 35) show 4.5 µm long Se(0) thin trigonal grey Se(0) nanowires (contrasting with the 8 nm wide magnetite nanoparticles) (Poulain et al., 2022), and sorbed Se(IV) intermediate surface complexes remain at the nanoparticle surface at longer reaction times. The Se(0) nanowires grew during the reaction, which points to a complex transport mechanism of reduced species or to active reduction sites at the tip of the Se(0) nanowires.

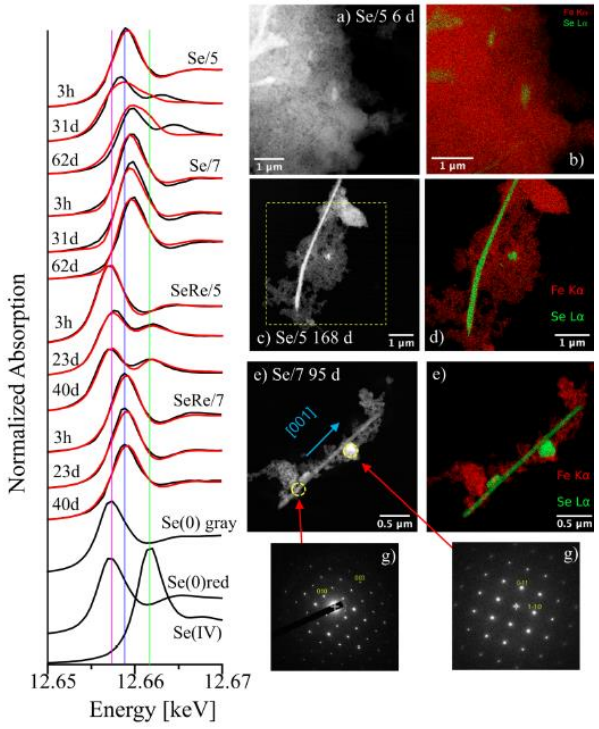

Figure 35. Left: Normalized Se-K edge XANES spectra of the magnetite samples from Se(VI) and Se(VI)/Re(VII) experiments and the three standard spectra. Data –black curves, fitting – red curves, max of both Se(0) – pink line, max of Se(IV) – green line. Right: STEM-HAADF and STEM-XEDS maps of magnetite samples: a-b) Se(VI) at pH 5, after 6 days – several selenium crystal seeds; c-d) Se(VI) at pH 5, after 168 days - > 5 µm long selenium nanowire ; e-f) Se(VI) at pH 7, after 95 days – 2.5 µm long nanowire with small selenium seeds; e) [211] zone axis of $P3_121$ Se(0); f) [100] zone axis of $P3_121$ Se(0) ; g-h).

3.1.3 Towards green rust [BRGM, CIEMAT]

In this section, the interaction between Se and green rust will be investigated with the aim, as in the previous sections, to determine the nature of the mechanisms of interaction and of the reaction product. Because literature studies previously evidenced an influence of the interlayer anion on green rust reactivity, two studies were performed, one with green rust containing interlayer Cl and one with green rust containing interlayer SO_4^{2-}.

[BRGM] The first step is studying green rust reactivity to have a sound understanding of the composition of the solid. For this purpose, several techniques were combined. Electron-probe microanalyser (EPMA) was used to determine the relative amounts of Fe, Co, and Cl. Differential Scanning Calorimetry coupled with thermogravimetric analysis was used to determine the abundance of interlayer water. Mössbauer spectroscopy was employed to determine the relative proportions of Fe^{II} and Fe^{III} in green rust structure, and to check for the presence of magnetic impurities, as magnetite is a frequent co-product with the presently used synthesis protocol (Hadi et al., 2014). Finally, X-ray photoelectron spectrometry was used to study Co oxidation state in green rust structure, and to crosscheck results obtained by Mössbauer. With all these methods, it could be determined that the green rust synthesised in this study had the chemical composition $[Co^{II}_{0.34}Fe^{II}_{0.39}Fe^{III}_{0.27}(OH)_2]^{0.27+}[Cl_{0.27}H_2O_{0.5}]^{0.27-}$, where species under brackets on the left-hand side form the layer, and those on the right the interlayer. Magnetite impurity represented 17 w% of the sample.

To study selenate [Se(VI)] reactivity towards green rust with interlayer Cl, we made use of a flow-through reactor, which was previously used, for example, to study the reactivity of many lamellar phases, including cement lamellar phases (C-S-H, AFm) and phyllosilicates. Briefly, a known amount of solid (here, 0.5 g green rust with interlayer Cl)is introduced in two different reactors that are ran in parallel, and a solution (here, containing 5 mmol/L Se) is flowed through the reactor. After equilibrium is assumed reached, one of the two reactors is stopped and the solid inside is recovered, and in the second reactor, the input solution is changed, and is replaced with one containing 100 mmol/L Cl), to study sorption reversibility. This method allows characterizing the initial solid, after reaction with Se, and after the system has been subjected to sorption reversibility test. The evolution of main chemical parameters during this sorption experiment is shown in Figure 36.

Various information can be extracted from the qualitative analysis of these data. First, Fe and Co were co-varied during the experiment. As only Fe^{II} is soluble under present pH conditions and as Co^{II} was as present in comparable amount to Fe^{II} in green rust structure, this shows that green rust equilibration in water occurs stoichiometric to the structure. In addition, the evolution of the concentration of Fe^{II} and Co^{II} can be used as a proxy to the evolution of green rust solubility. Fe^{II} and Co^{II} concentration in solution was only appreciable when the sample was initially contacted with the solution and when it was contacted with Cl^-. When it was contacted with a solution containing Se^{VI}, Fe^{II} and Co^{II} aqueous concentration dropped to values below the detection limit. In the assumption of interlayer exchange between Cl and Se, this is interpreted as green rust with interlayer selenium (Gr-Se) having a lower solubility than green rust with interlayer Cl (Gr-Cl).

The solid collected after the contact with Se containing solution (i.e., the sample originating from the reactor stopped after step 1 of the presently applied protocol) was studied for its structural evolution. Based on thermogravimetric analyses, the sample did not contain any interlayer water, and, from XPS, 100 % of Co was in Co^{II} form, Fe was 22 % Fe^{II} and 78 % Fe^{III}, and Se was 80 % Se^0, and 20 % Se^{IV} (Figure 37). Se^{VI}, which was initially in contact with the solid, could not be detected. The Fe speciation determined by XPS was, within uncertainties, equal to that determined by Mössbauer spectrometry (23 % Fe^{II}, 30 % Fe^{III}, 27 % magnetic Fe^{III} - Figure 38).

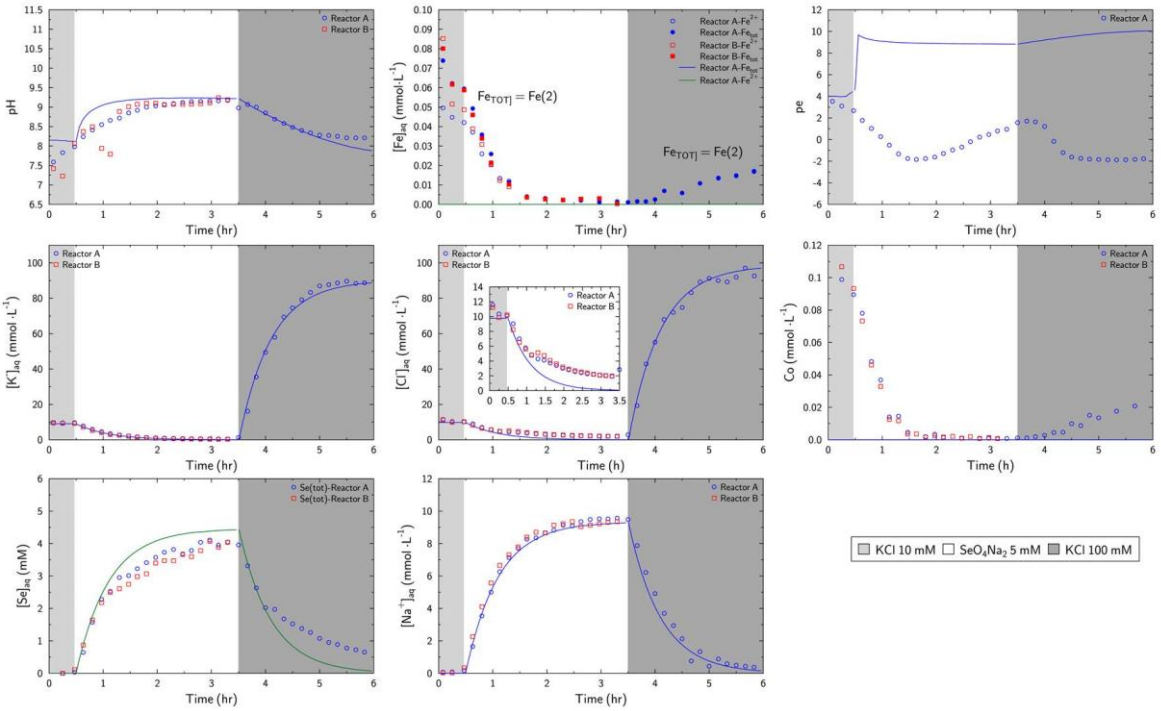

Figure 36. From left to right and top to bottom: pH, [Fe], pe, [K], [Cl], [Co], [Se] and [Na+] as a function of time in the flow-through experiments. Squares are the data, and lines the model, assuming no reactivity (i.e., only transport). The light grey, white, and dark grey shaded areas materialize respectively the equilibrium, Se sorption, and Cl sorption steps.

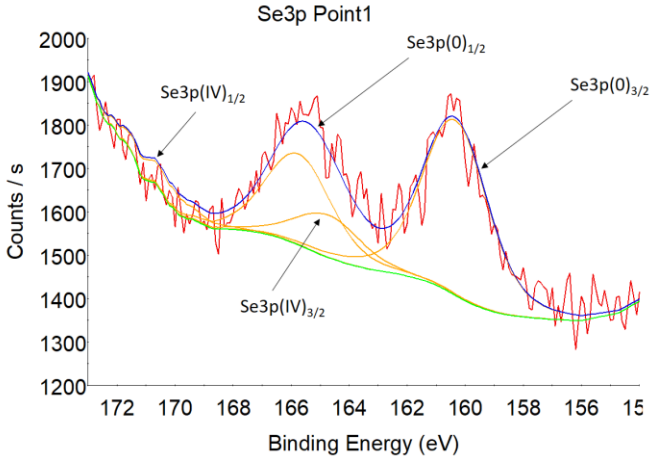

Figure 37. XPS spectrum of Gr-Se sample, at the Se edge.

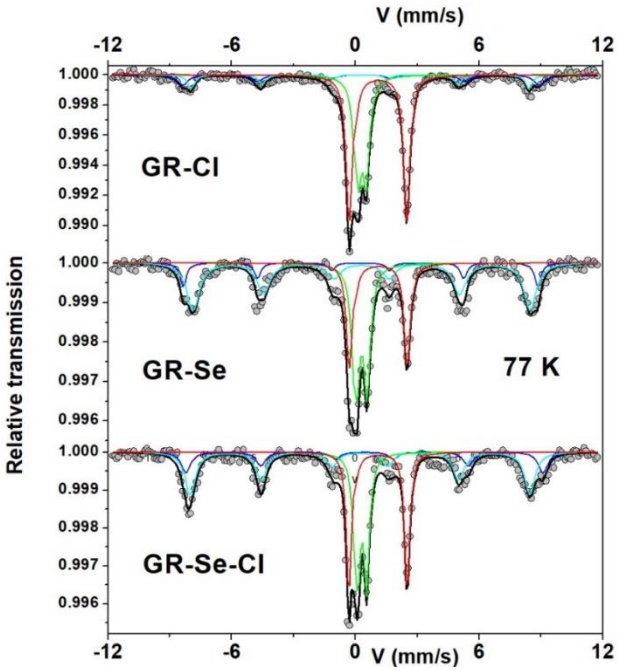

Figure 38. Mossbauer spectra of, from top to bottom, Gr-Cl, Gr-Se, and Gr-Se-Cl. Dots are the data points, and lines the modelled spectrum. Modelling parameters are presented in Table 15.

Table 15. Mossbauer modelling parameters.

Sample	Isomer shift (mm/s)	FWHM (mm/s)	QS/2ε	Magnetic hyperfine field (T)	Area (%)
Gr-Cl	0.35	0.4	0.3		23
	1.1	0.52	2.48		43
	0.24	0.52	0.09	48.4	17
	0.6	0.52	-0.04	46.9	17
Gr-Cl	Gr-Cl	Gr-Cl	Gr-Cl	Gr-Cl	Gr-Cl
	1.11	1.09	1.94		18
	0.29	0.91	-0.05	47.7	35
	0.68	0.91	-0.55	42.1	15
Gr-Se-Cl	0.35	0.57	0.48		25
	1.1	0.55	2.11		20
	0.35	0.66	0.11	49.1	21
	0.4	0.66	0.05	46.5	15
	0.59	0.74	0.15	36.7	19

Using EMPA results from Mossbauer, the chemical formula of the sample after it was saturated with Se can be defined as $[Co^{II}_{0.42}Fe^{II}_{035}Fe^{III}_{0.23}(OH)_2]^{0.23+}[Cl_{0.16}SeO_3^{2-}{}_{0.03}]^{0.23-}$. The sample composed of 60% green rust, 30 % magnetite, 10 % non-magnetic Fe^{III} oxide, and Se^0. After the sample was subjected to step 2 of the experiment (saturated back with Cl^-), Se^{IV} desorbed, and the chemical formula of the product (Gr-Se-Cl) was $[Co^{II}_{0.36}Fe^{II}_{038}Fe^{III}_{0.25}(OH)_2]^{0.25+}[Cl_{0.24}SeO_3^{2-}{}_{0.01}]^{0.25-}$. To determine whether Se^{IV} was adsorbed at green rust surface or adsorbed in the interlayer, oriented preparations were done.

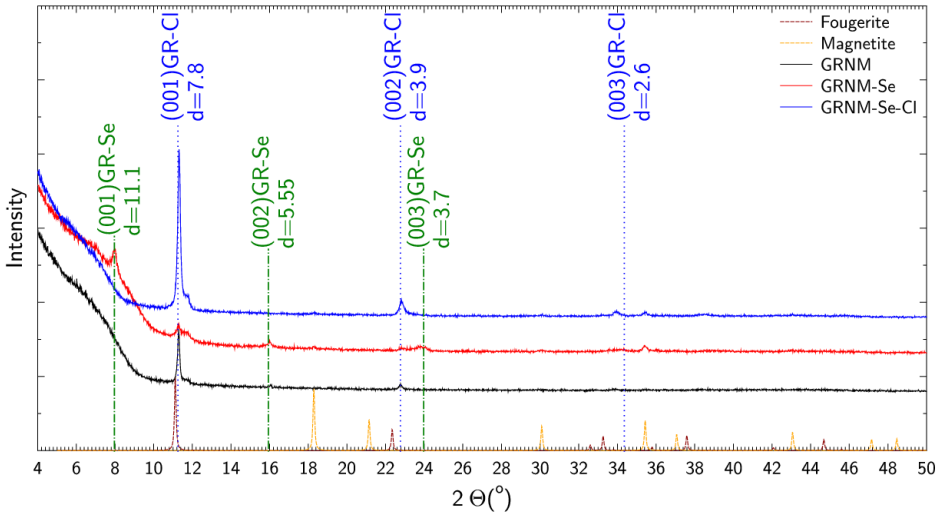

Figure 39. XRD patterns of, from top to bottom, Gr-Cl, Gr-Se, and Gr-Se-Cl.

In the XRD pattern of the Gr-Cl (Figure 39), the 001 reflection was at 7.8 Å, coherent with green rust with interlayer Cl. In the pattern of Gr-Se, this reflection was weaker, and an additional reflection at 11.1 Å was observed. This translates incorporation on an interlayer species having a higher ionic radius than Cl and is attributed in this study to $Se^{IV}O_3^{2-}$. In the pattern of Gr-Se-Cl, the reflection at 11.1 Å was not observed anymore, and the intensity of the one at 7.8 Å increased, showing that Cl^- replaced SeO_3^{2-} in the interlayer.

Using chemical data, mass balances calculations can be performed, to check for the Se^{IV}/Cl exchange stoichiometry. In step 1 (Se sorption), 1.09 mmol Cl was released from the reactor, and 0.26 mmol Se was adsorbed. Hence, the Cl/Se ratio was 4.3. Coherent with XPS, this suggests that, during this step, Se was not only retained in the solid by a Se/Cl exchange which would induce a Cl/Se stoichiometry of 2, but also by other mechanisms. Here, these additional mechanisms are assumed to be the redox reaction leading to the formation of Se^0 that remains in the solid. In step 2, 0.5 mmol Cl was sorbed, and 0.25 mmol Se was released from the solid. Here, the Cl/Se ratio was 2, coherent with sorption of Cl^- in the interlayer by replacing SeO_3^{2-}. Finally, from the difference between sorbed and released Se, it can be calculated that an equivalent of 0.11 w% of the final sample was Se^0, coherent with the fact that it was not detected by XRD.

Overall, the mechanism of SeO_4^{2-} interaction with green rust containing interlayer Cl can be described as a multi-step process. The first step is the adsorption of Se(VI), probably as SeO_4^{2-}, in green rust interlayer. Then, Se(VI) is reduced to Se(IV) while remaining in green rust interlayer. Oxidized Fe forms magnetite. Finally, Se is reduced to Se(0).

[CIEMAT]

[CIEMAT] performed $^{75}Se(IV)$ sorption studies on laboratory synthetized sulphate green rust as a function of pH in $NaClO_4$ 0.1 M, under N_2 atmosphere in the absence of O_2. Higher selenium retention was measured on sulphate green rusts than in magnetite, under equivalent conditions (Missana et al., 2009c). Results showed that selenium sorption on sulphate green rusts was independent of pH, suggesting an exchange process with sulphates. Selenium sorption kinetics carried out up to 60 days (Figure 40) showed selenium desorption at longer times.

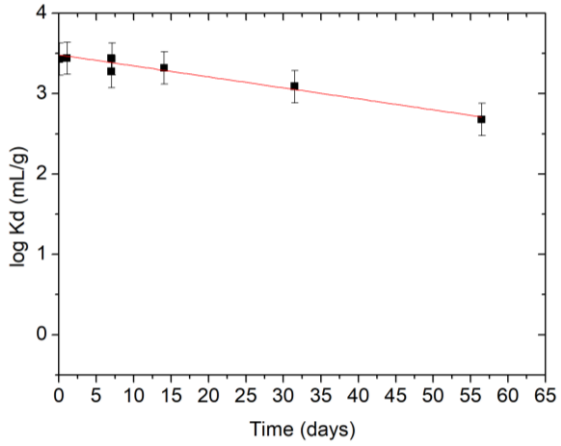

Figure 40. ^{75}Se(VI) sorption kinetics on laboratory synthetized sulphate green rust in 0.1 M $NaCl0_4$ at pH 6 with an initial selenium concentration of $2.48 \cdot 10^{-6}$M.

3.1.4 Towards mixtures of smectite and Fe-phases [CIEMAT]

Sorption tests of radionuclides (uranium, selenium and technetium) are carried out in mixtures of clay and selected oxides. The studies aim to answer two questions:

- Do iron oxides from corrosion of containers affect the retention of radionuclides?
- If yes, are we able to describe the sorption of radionuclides in oxide and clay mixtures using additive models? Previous studies demonstrate that in many binary systems, interactions between particles of different nature modify the retention of radionuclides.

[CIEMAT] carried out ^{75}Se(VI) sorption experiments on mixtures of Na-FEBEX smectite, separately mixed with different proportions of goethite, magnetite, and Fe(0) shavings (from 0 to 100%) at two different pH (4 and 9). In all cases, the addition of the Fe phase to smectite increased selenium retention, attributed to the increased of positively charged surface sites, provided by the oxide, rather than to redox reactions. Under experimental conditions analysed, only when Fe(0) shavings are added to smectite, the Eh values reached may favour the reduction of selenite (Figure 41).

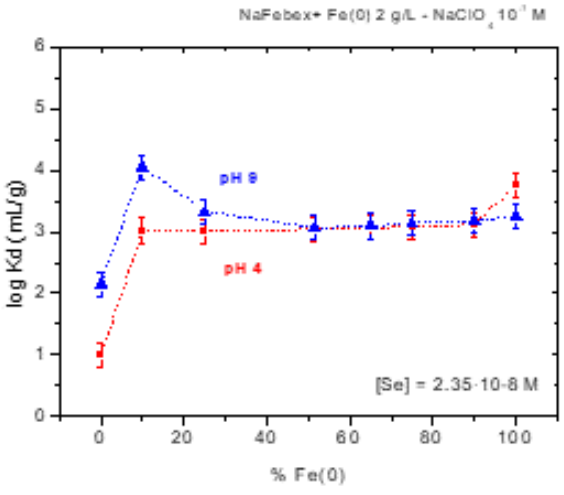

Figure 41. ^{75}Se(VI) sorption on Na-FEBEX smectite mixed with different proportions of Fe(0) shavings, at two pH conditions (pH 4 and pH 9). Selenium initial concentration $2.35 \cdot 10^{-8}$ M.

3.1.5 Summary concerning Se reactivity.

This section shows that the speciation of both Se(VI) and Se(IV) are affected by their interaction by Fe-bearing minerals, namely phyllosilicates, iron oxides, and green rust. An increased supply of Fe(II) to the system increases the amount of Se reacted. The redox interaction involves Se reduction and, in

turn, Fe(II) oxidation. The final reaction product is Se(0), and it seems that Se(VI) reduction is a two-steps processes, because intermediate Se(IV) is detected in studies with magnetite and green rust. Fe(II) involved in the Se reduction process needs to be redox-active, as measured using electrochemical mediators and, interestingly, it could be that the presence of redox-active Fe(III) influences the mineralogy of the Se(0) product.

3.2 Tc/Re reactivity

In this section, the interaction between Tc and (or) Re and phyllosilicates, and with mixtures of phyllosilicates and iron oxides, is investigated. Re was used as a stable analogue for ^{99}Tc. As for Se, the main objectives here were to determine the mechanisms of interaction, and to distinguish between adsorption and redox reaction when Tc/Re is sorbed by the solid of interest. Finally, in this section, the kinetics of interaction where also studied.

3.2.1 Towards phyllosilicates [RATEN, PSI, CIEMAT]

[RATEN]

As Tc is one of the main safety relevant radionuclides for Romanian geological repository for CANDU SF, RATEN experimental work performed in the frame of EURAD FUTURE was focused on understanding the sorption of Tc on iron-bearing minerals. As clay is one of the potential host rock for the Romanian geological repository, and bentonite will be most probable used as buffer/filling, the experimental tests were first performed on pure mineral (Na-montmorillonite).

Tc sorption on Na-montmorillonite was studied using Re (as chemical surrogate for Tc-99). Re sorption kinetics tests and tests to derive the sorption isotherm (in the cases where sorption equilibrium could be achieved during the experimental timeframe) or to evaluate the influence of Re concentration in solution on its sorption, with and without the addition of a reducing agent (sodium dithionite), where performed on Na-montmorillonite suspension, as well as on the suspension enriched with iron ions (to assess the Fe influence on Re sorption).

The sorption tests were carried out in controlled environment (Ar atmosphere), in a polyethylene box with integrated gloves type "*sekuroka - glove bags*" that was purged with Ar until an oxygen level inside the bag was less than 0.1%. From the Na-montmorillonite suspension, 250 ml was sampled under stirring and transferred into a 250 ml Erlenmayer flask, the pH was adjusted to 11-12 with NaOH and bubbled with Ar for 3 hours to remove any residual oxygen. Centrifuge tubes (15 ml PP centrifuge tubes) where prewashed and dried to be used in the sorption tests. Re solution equivalent to a concentration of 2.68E-5 mol/L and 10 ml of the Na-montmorillonite suspension were added in each test tube. For the tests with sodium dithionite used as reducing agent (samples denoted with D), sodium dithionite was added to a ratio DT:solid of 3:1. After Na-montmorillonite suspension was contacted with Re solution, the test tubes were closed inside the glove bag, sealed with parafilm and kept for equilibration on an orbital shaker, at 120 rpm outside the glove bags. For Re measurement in the aqueous phase, the test tubes were centrifuged at 3950 rpm, for 40 minutes, and adequate aliquot of supernatant was sampled to analyse the Re concentration by ICP-OES.

3.2.1.1 Sorption tests on Na-montmorillonite suspension – without sodium dithionite addition

For the Na-montmorillonite suspension with a solid substance of 12.74 g/l of suspension, at initial pH adjusted to 11, for a Re concentration of 2.68E-5 mol/L, it was found that the Re sorption is very low, the percentage sorbed remains almost constant during the testing period (130 days) with a sorption percentage ranging between 8-9%, with a maximum recorded after 7 days (Figure 42).

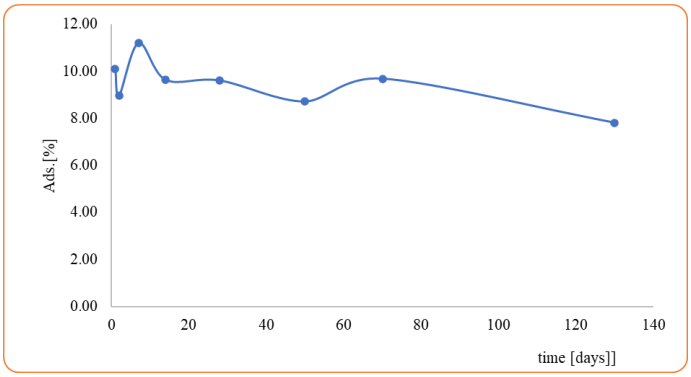

Figure 42. % of Re adsorbed as a function of time.

A decrease of pH to ~6.5 was registered during the sorption kinetics tests and the measured redox potential was in the range of +250mV to +340mV. These redox conditions correspond to an oxidizing environment in which according to the state diagram (pH-Eh) Re is mainly found in the form of Re(VII). Some amount of Fe was measured in the sampled aqueous aliquots but in low concentrations: ~2.4 mg/L compared to the initial concentration of 16.9 mg/L, indicating its sorption (precipitation/complexation) on the surface of the montmorillonite. Under the experimental conditions the state diagram of Fe indicates that Fe is found in the solid form of Fe_2O_3.

Since the sorption kinetics experiment highlighted that the sorption equilibrium is difficult to reach as the pH and the redox potential do not remain constant throughout the sorption test, Re distribution coefficient is difficult to be assess as this concept is defined at equilibrium. Nevertheless, a distribution ratio (defined as ratio between concentration of Re sorbed on clay mineral to the Re concentration in the aqueous solution) was calculated for different Re initial concentrations in solutions. These assessments were performed for contacting period of 7 and 14 days, for four different concentrations of Re in the solution, in the range of E-6 mol/L and E-4 mol/L (Table 16)

Table 16. Initial, sorbed, and equilibrium Re concentration in the experiments, and related Rd and sampling time. Generally, an increased Re sorption with the increasing the Re concentration in solution was observed, and an average distribution ratio of ~0.02 L/g for 7 days of contacting and 0.01 L/g for 14 days of contacting, aver the concentration range considered.

initial Re conc. [mol/L]	**C_{aq}[mg/L]**	**C_{sor} [mg/g]**	**R_d [L/g]**	**Sampling time**
$5.3x10^{-6}$	0.8917	0.0163	0.0183	7 days
$2.6x10^{-5}$	3.8406	0.0832	0.0217	
$5.3x10^{-5}$	8.8414	0.0909	0.0103	
$2.6x10^{-4}$	41.2518	0.6631	0.0161	
			average R_d = 0.0166 L/g	
$5.3x10^{-6}$	0.8927	0.0006	0.0007	14 days
$2.6x10^{-5}$	4.5096	0.0385	0.0085	
$5.3x10^{-5}$	8.9706	0.0729	0.0081	
$2.6x10^{-4}$	42.8792	0.5354	0.0125	
			average R_d = 0.0075 L/g	

3.2.1.2 Sorption tests on Na-montmorillonite suspension – with sodium dithionite (DT) addition

The addition of the reducing agent at the time of contacting the O_2-free Na-montmorillonite suspension with Re solution led to a decrease in the pH (5.4 – 6.4), but also to a decrease of the redox potential up to -535 mV in the first 14 days from contact, followed by an increase of the Eh after 28 days to approximately +100mV, increase potentially generated by the atmospheric oxygen diffusing in the test tubes during equilibration period (when the test tubes were kept outside the glove bags).

The Re sorption kinetics test in the presence of DT as reducing agent indicated that Re sorption is increased in the first period compared with the sorption without DT: after 14 days the sorption percentage of ~38% (compared with ~12% without DT). After 14 days, due to the alteration of oxidizing conditions

(Eh starts to increase) the percentage of Re sorbed on Na-montmorillonite decreased to ~20% after 60-70 days. The decrease seems to be related to the decrease in pH and the increase in the measured redox potential, an oxidizing environment in which Re species is perrhenate and probably the previously sorbed Re was desorbed (Figure 43).

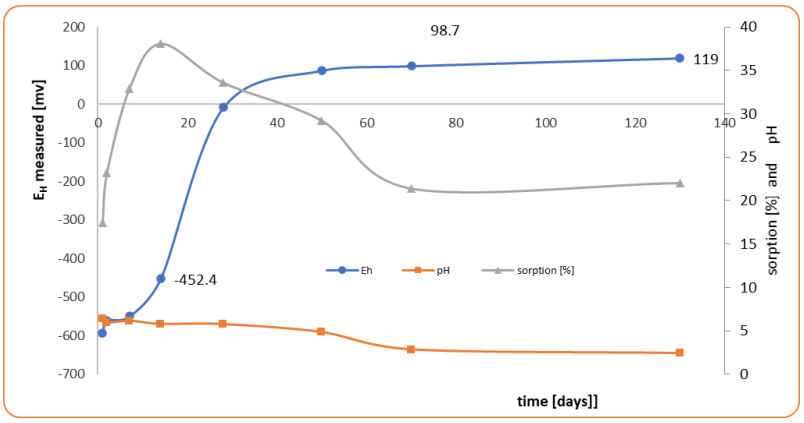

Figure 43. Eh, pH, and % sorption as a function of time.

Also in the tests with DT addition it is difficult to obtained sorption equilibrium and to have an indication on the Re sorption on Na-montmorillonite, distribution ratio was computed for four different Re initial concentration in solution (Table 17).

Table 17. Main chemical parameters and Rd of the Re sorption on Na-montmorillonite. For the first testing intervals (7 and 14 days), as the Eh was reducing, the Re sorption on Na-montmorillonite was slightly increased, with average Rd of ~0.05 L/g. After 50 days, as the redox conditions were altered, the obtaining average Rd was 0.02 L/g, similar with the value obtained for the tests performed without DT addition.

$C_{initial}$ [mol/L]	pH	Eh [mV]	C_{aq} [mg/L]	C_{sor} [mg/g]	R_d(L/g)	time
5.3E-6	12.6	-851.9	1.2373	0.0049	0.0040	
2.6E-5	12.61	-852.9	3.7592	0.1052	0.0280	
5.3E-5	12.51	-846.0	5.2441	0.3812	0.0727	**7 days**
2.6E-4	12.53	-847.4	24.7465	1.9587	0.0792	
Average R_d~ 0.046 L/g						
5.3E-6	12.53	-841	0.9533	0.0037	0.0039	
2.6E-5	12.55	-841.1	3.5430	0.1065	0.0301	
5.3E-5	12.55	-839.5	5.1728	0.3868	0.0748	**14 days**
2.6E-4	12.12	-823	23.8619	2.0281	0.0850	
Average R_d~0.048 L/g						
5.3E-6	5.4 – 6.4	~ 100	0.5441	0.0106	0.0195	
2.6E-5			3.998	0.1241	0.0310	
5.3E-5			7.330	0.1523	0.0208	**50 days**
2.6E-4			45.612	1.0636	0.0233	
Average R_d~0.024 L/g						

As the sorption kinetics test indicated that after around 70 days Re concentration in solution and Re absorbed on the clay fraction seems to be in equilibrium, the experimental data were fitted with linear and power type isotherms, with a correlation coefficient of around 0.98. The values for distribution coefficient (assuming that indeed equilibrium is achieved) derived from the linear and respectively Freundlich type isotherms are similar ~ 0.02 L/g (Figure 44).

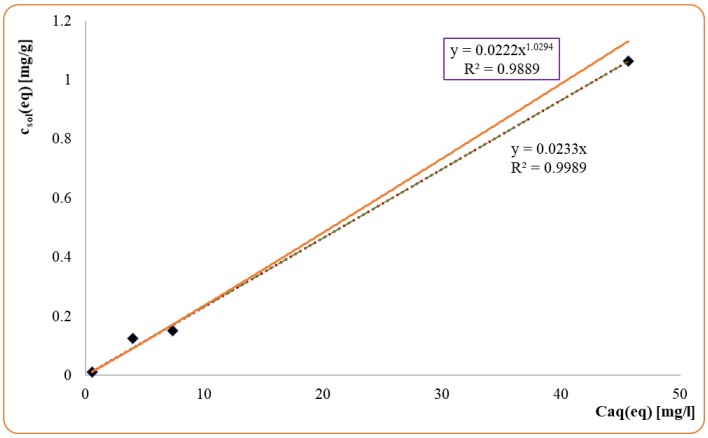

Figure 44. Sorbed Re as a function of equilibrium Re concentration.

3.2.1.3 Influence iron on the Re sorption on the Na-montmorillonite

The influence of iron (Fe(II)/Fe(III)) on the Re sorption on montmorillonite was evaluated for Fe(III) content of 1.6 mg/g (for samples without DT) and respectively Fe(II) content of 1.68 mg/g (for samples with DT addition)

Re sorption kinetics was evaluated for Re initial concentration in the contacting solutions of 2.68E-5 mol/L (5mg/L), while the tests to assess the influence of Re concentration on its sorption and derive the sorption isotherms (if equilibrium is attained) where performed for Re concentration in the contacting solutions between $2.6x10^{-6}$ mol/L and 2.6×10^{-4} mol/L. All sample preparations were performed in glove bags with O_2 content kept around ~0.1%. After their preparation, all samples were extracted from the glove bag, sealed with parafilm, and kept for equilibration on a shaker at 120 rpm. Re concentration in solution was measured by ICP-OES, after centrifugation for phase separation. For the tests performed with reducing agent addition, the suspension reduction was achieved by adding 4.2 g of sodium dithionite (DT) and bubbling with Ar for ~4 hours at 40°C. After reduction step, all samples were introduced in the glove bag and prepared for sorption tests similar those for the sorption tests with no DT addition. At the set time intervals, the samples were centrifuged at 3950 rpm for 40 minutes, an aliquot of supernatant was sampled to measure the Re concentration by ICP-OES, while the rest of the sample was stirred, and the redox potential and the pH of the suspension were measured.

The curve describing the Re sorption kinetics on iron-enriched montmorillonite suspension has a maximum after 28 days of contacting, after which the sorption percentage has a decreasing trend to values of ~10%. The sudden increase in sorption cannot be correlated with the variation of the redox potential or of the pH of the solution, as the Eh values (measured at the time of sampling for Re measurement) were 120 - 40mV, while the pH value was constant during the testing period (~9.4). This increase at 28 days could be correlated with the iron concentration in aqueous phase, which registers a maximum value at that time (Figure 45).

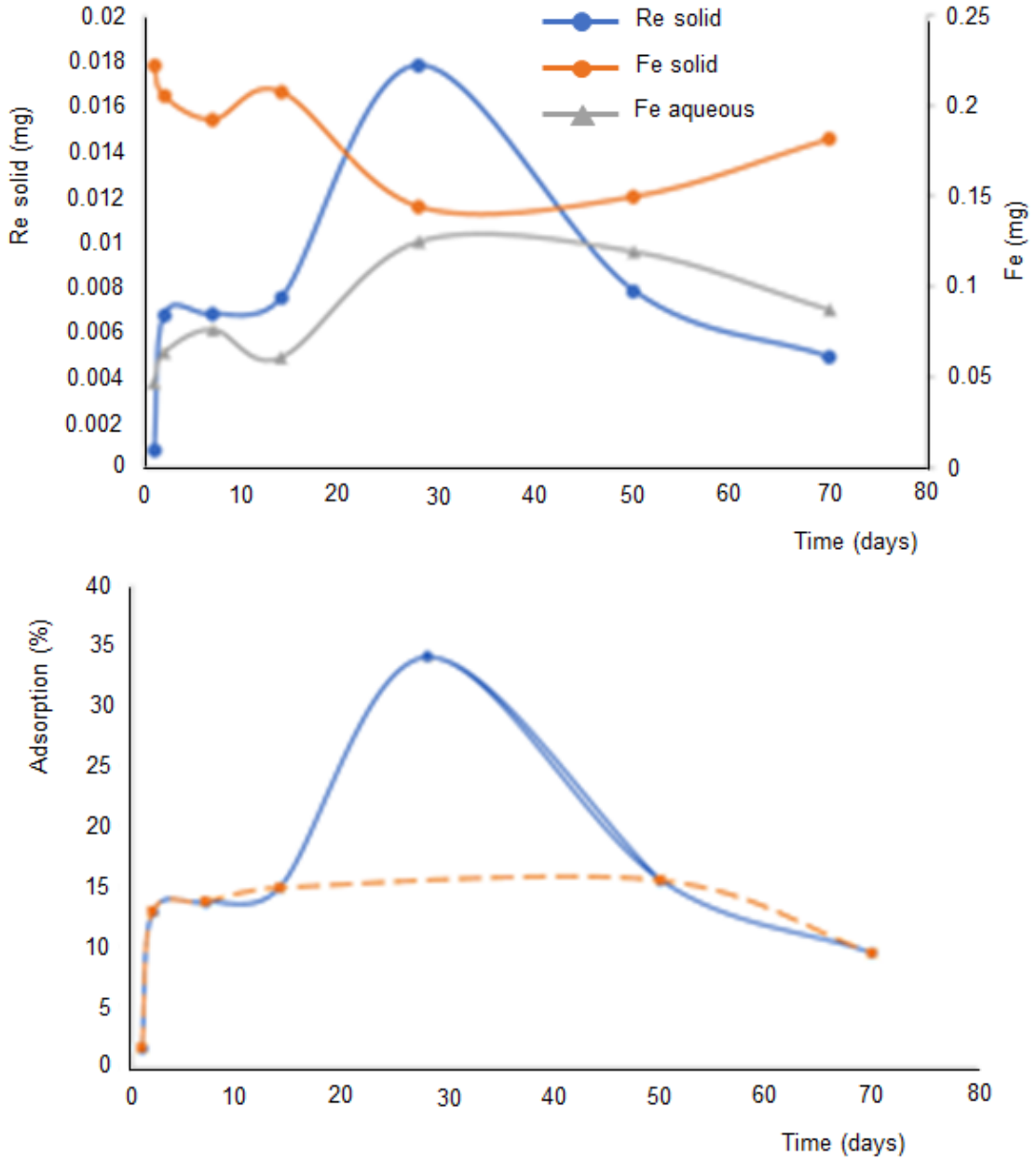

Figure 45. Top: Re solid (blue), Fe solid (orange), and aqueous Fe (grey) as a function of time. Bottom: % of Re adsorption as a function of time.

Except this increase of sorption percentage at 28 days, Re sorption seems to be at equilibrium, with a sorption percentage of around 15%. To assess the influence of Re concentration on its sorption on iron-enriched montmorillonite, four Re concentrations in contacting solutions where used (ranging between 0.5 mg/L and 50 mg/L) and the Re in solution was measured after 50 days of equilibration time (Table 18).

Table 18. Initial, aqueous, and sorbed Re concentration in the various experiments, and individual and average Rd value.

$C_{initial}$ [mol/L]	C_{aq} [mg/L]	$C_{sorb.}$ [mg/g]	R_d, L/g
5.3E-6	0.4157	0.00528	0.0127

2.6E-5	4.2440	0.06147	0.0145
5.3E-5	8.3759	0.13952	0.0167
2.6E-4	38.6330	0.82134	0.0213
Average Rd: 0.02 L/g			

Assuming that in 50 days of contacting equilibrium has been reached, the above experimental were used to derive the sorption isotherm. These data can be reasonably fitted with a linear isotherm (R^2=0.9968) and by a power-type one, specific to the Freundlich isotherm (R^2=0.9991) (Figure 46).

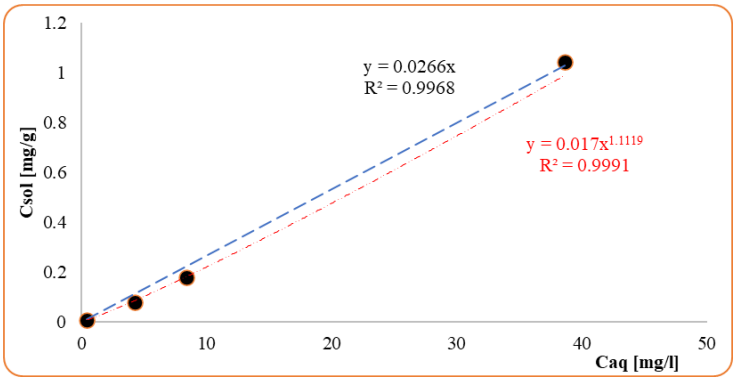

Figure 46. Sorbed Re as a function of aqueous Re, and linear modelling.

Distribution coefficient derived from the slope of linear sorption isotherm is 0.027 L/g dry montmorillonite. The dimensionless parameter from the Freundlich isotherm, [$C_{sorb}(eq)=K_F \cdot C_{aq}(eq)^N$] is above unity (1.1119) suggesting that Re uptake takes place by precipitation/co-precipitation on the mineral surface, as the solubility limit being exceeded.

Since the correlation coefficient R^2 is closer to 1 for the power-type fitting of experimental data (Freundlich isotherm), it can be considered that this type of isotherm represents the best approximation of the experimental data obtained for Re sorption on iron enriched montmorillonite, in an alkaline environment. The distribution coefficient estimated using the Freundlich model is 0.017 L/g dry montmorillonite.

To obtain strongly reducing conditions, sodium dithionite (DT) was used as a reducing agent to reduce Fe(III) ions to Fe(II) and Re(VII) to Re(IV) (Table 19). According to literature data, adding a quantity of dithionite in a mass ratio of 3:1 to the montmorillonite quantity in the suspension and keeping the pH neutral to alkaline and keeping an anoxic environment, under a slight heating (40-70°C), the reduction of the trivalent iron present in the mineral structure to divalent iron is obtained. The iron present in the aqueous phase before the dithionite addition is involved in the precipitation/co-precipitation and complexation reactions with Re; this was evidenced by the absence of Fe in the aqueous phase.

Table 19. Contacting time, Eh, and pH upon reduction by DT.

Contacting time[days]	$Eh_{masurat}$ [mv]	pH
1	-824.3	12.36
2	-825.1	12.13
7	-840.4	12.33
14	-828.6	12.17
28	-799.5	11.04
50	-92.5	7.96

Under these reducing conditions, Re sorption on the Fe-enriched montmorillonite was evaluated at more than 20% in the first 24 hours, followed by an increase to ~39% after 28 days of contacting (Figure 47).

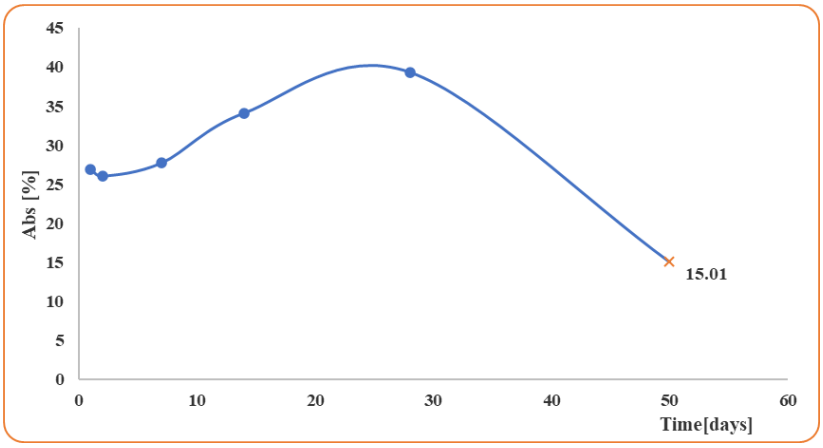

Figure 47. Re sorbed on Fe-enriched montmorillonite as a function of time.

After 50 days of contacting, an alteration of the initial reducing conditions was recorded, with an increase in Eh and a decrease in pH, and in these altered conditions Re desorption took place. The decrease of Re sorption on the montmorillonite measured after 50 days of contacting can be correlated with the increase of Fe concentration in the aqueous phase at that time (Figure 48).

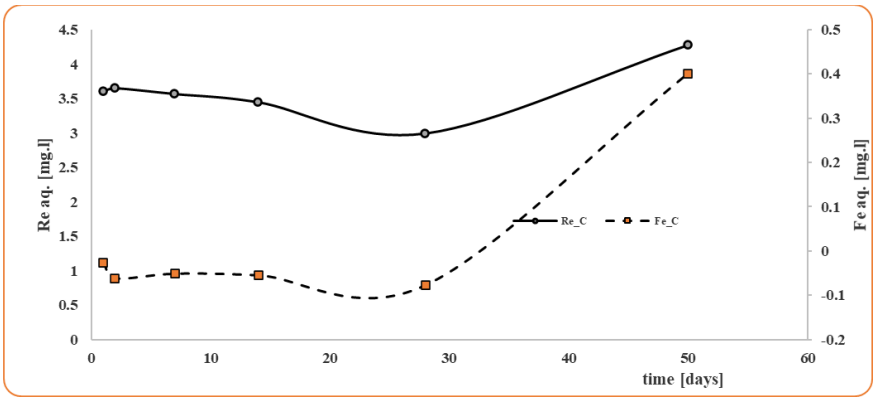

Figure 48. Aqueous Re (black symbols) and Fe (orange symbols) concentrations as a function of time, in the experiment involving 50 d of contact between Re and montmorillonite and in which dithionite was initially added (see text for details).

Formation of a soluble compound/complex between Fe and Re may explain the decrease of Re sorption. The presence of this kind of Fe-Re compound or complex was evidenced at preparing the aliquot sampled for Re and Fe measurement by ICP-OES. The resulted solution after HNO_3 addition (to get a solution with 1% HNO_3) was opaque, cloudy, requiring dilution to be measured by ICP-OES. As it was clear from the sorption kinetics that the sorption equilibrium is strongly perturbed once the redox conditions are altered, the sorption isotherms couldn't be derived. The experimental data obtained after 50 days of contacting, for Re initial concentration in solution ranging between 0.5 mg/L and 50 mg/L, were used to calculate the distribution ratio (Rd) for each initial Re concentration in solution (Table 20).

Table 20. Initial, aqueous, and sorbed Re concentrations, and related individual and average R_d values.

$Re_{initial}$ [mol/L]	**Re_{aq} [mg/L]**	**Re_{sorbed} [mg/g]**	**R_d, L/g**
5.3E-6	0.31	0.01	0.0323
2.6E-5	4.10	0.06	0.0146
5.3E-5	3.39	0.52	0.1534
2.6E-4	39.01	0.77	0.0197
Average R_d: **0.06 L/g**			

The presence of high concentrations of iron ions in suspension seems to be detrimental for Re sorption as Fe ions are preferentially sorbed on clay surface through complexation and precipitation processes, most likely forming $FeCl^+$ complexes with the Cl^- ions from the solution, reducing the possibility of Re complexation under oxidizing conditions. The addition of the reducing agent favours the development of a reducing environment in which the Fe is transformed to Fe_2O_3 but also reduced Fe(II) in the form of $Fe(OH)_2$, but also Re reducing to Re(IV). These conditions are more favourable for the formation of compounds that are sorbed on the surface of the clay mineral either through complexation reactions or through precipitation/co-precipitation reactions.

No significant enhancement of Re sorption on montmorillonite was observed after montmorillonite enrichment with Fe. The observed increase of sorption may be correlated with a lower redox potential in the tests on Fe-enriched montmorillonite in the first days of sorption tests, which favour reducing of Fe and Re and the formation of complexes on the mineral surface (Figure 49).

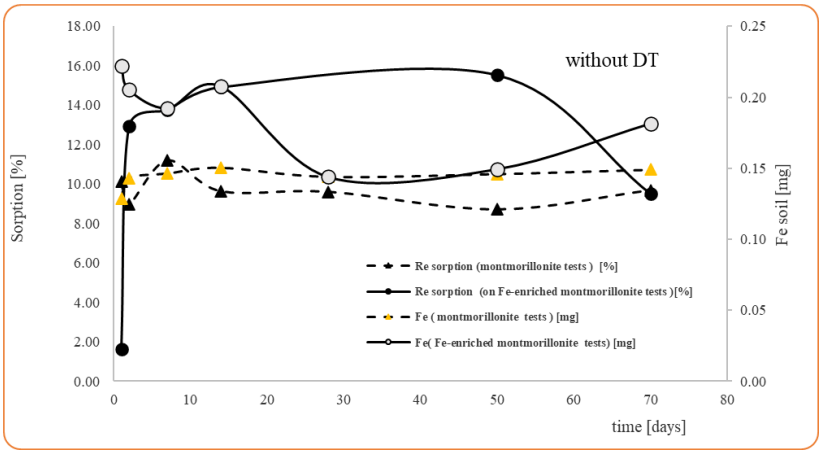

Figure 49. Re sorbed on montmorillonite (black triangle), on Fe-enriched montmorillonite (black circles), and Fe sorbed on montmorillonite (orange triangles) and on Fe-enriched montmorillonite (open circles) as a function of time, in the absence of DT.

Regarding the tests performed with sodium dithionite (DT) addition (Figure 50), an increase in Re sorption can be observed from the first day of the sorption tests. During most of the testing period, Re sorption has a similar evolution to that of Fe retained on montmorillonite. This suggests that under reducing conditions (Eh ~ -500mV) and pH ~6, the retention of Re(IV)/Re(0) – neutral species (according to the state diagram for Re species) can be attributed either to the formation of complex with Fe that is found as $Fe(OH)^+$, or to the retention on the montmorillonite surface sites (Schweitzer and Pesterfield, 2010).

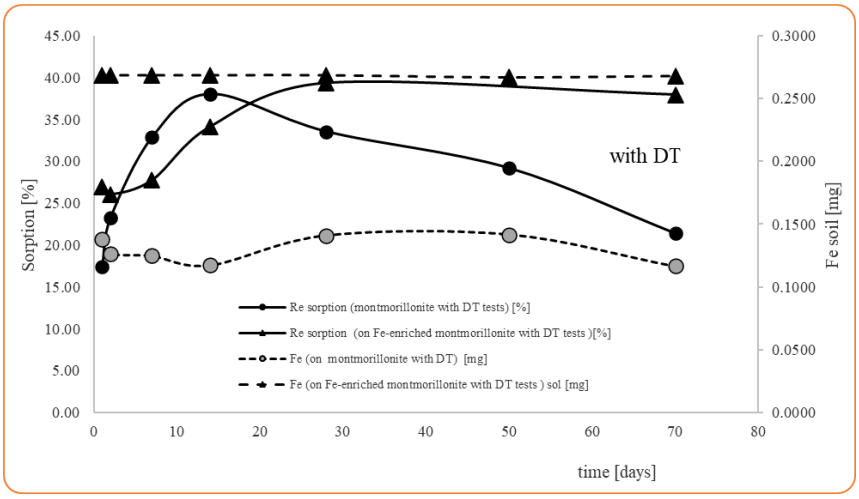

Figure 50. Re sorbed on montmorillonite (black circles), on Fe-enriched montmorillonite (black triangles with full), and Fe sorbed on montmorillonite (open circles) and on Fe-enriched montmorillonite (black triangles with dotted line)) as a function of time, in the presence of DT.

A different behaviour in the samples with DT addition and Fe-enriched montmorillonite was observed. Iron is absent in the aqueous phase during almost the entire testing period, which implies that it either reduced to Fe(II) or forms soluble compounds such as $Fe(OH)_2$. The resulting products are apparently retained on the surface of the mineral through surface complexation processes or precipitation-co-precipitation reactions with the formation of partially soluble compounds. Such a partially soluble complex formed between Fe, S and Re is soluble in an alkaline environment and precipitates in a weakly acidic environment. This was observed when preparing the supernatant sample for ICP-OES analysis, when the acidified samples required filtration to have a clear solution for ICP-OES measurement. It is possible that the high sorption recorded in the samples with DT addition is due to the precipitation that occurred during sample preparation for measurement and not to real sorption processes. In the reducing conditions (Eh measured ~-800mV) and pH around 12, according to the state diagram Re is found as metallic Re (Re(0)) or Re(IV) and is characterized by high sorption. At pH=12, Fe forms soluble compounds, such as $Fe(OH)_2$, that can be retained either by complexation on the surface or by hydrolytic adsorption of Re in the form of $ReO(OH)_2$.

3.2.2 Towards nontronite [PSI, CIEMAT]

In this section, the interaction between Tc(VII) and several samples of nontronite, the Fe-rich endmember of the phyllosilicate minerals, is investigated with the aim of understanding the influence of the Fe(II)/Fe(III) ratio and of the location of Fe(II) (structural or adsorbed) on nontronite Tc sorption capacity, and mechanism of retention.

[PSI]

Tc(VII) batch sorption experiments were performed on native NAu-2 (no structural Fe(II)), low-red NAu-2 (low structural Fe(II)), and high-red NAu-2 (high structural Fe(II)) in 0.1 M NaCl .The pH dependant sorption of Tc($1x10^{-7}$ M at S/L ratio = 2 g/L) on the different clays is shown in Figure 51. No Tc (VII) sorption was observed on native NAu-2 over the whole pH range. Tc (VII) sorption was observed on both high-red NAu-2 and low-red NAu-2 from pH 4 to 7.5. High-red NAu-2 which contains more structural Fe(II) shows higher Tc(VII) sorption than low-red NAu-2 having lover Fe(II) content. Sorption increases as the structural Fe(II) increases from pH 4.0 to 7.5. Above pH=8, Tc(VII) sorption decreases rapidly. At pH=7, Fe^{2+}_{aq} which is in equilibrium with high-red NAu-2 is adsorbed on the surface of the clay and enhanced Tc(VII) sorption.

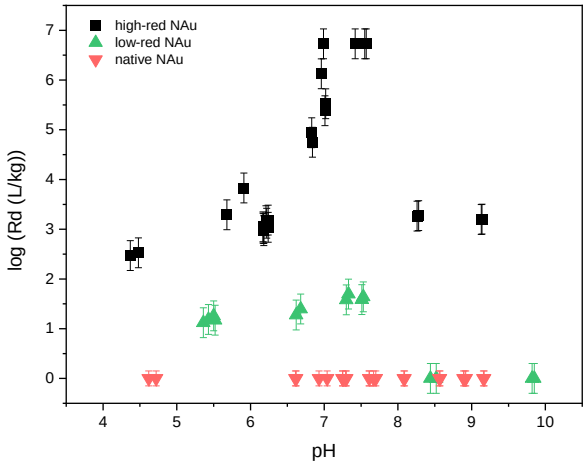

Figure 51. Tc(VII) sorption on high-red NAu-2, low-red NAu-2 and native NAu-2 at S/L of 2 g/L and [Tc]= 10^{-7} M in 0.1 M NaCl after 7 days.

The concentration dependent sorption of Tc(VII) on the two reduced forms of Nau-2 was quantified in the pH range 5.5 to 7.5 as a function of the Tc(VII) concentration and the results are shown in Figure 52. On low red-Nau the sorption Tc(VII) in both pH ranges is fairly linear up to [Tc_{eql}] ~10^{-5}M)(slope of ~1.1). At [Tc_{eql}] > 10^{-5}M, the sorption reaches either a plateau in pH range 5.5 to 6 or increase more steeply at pH 7.5. On high red-Nau, the sorption of Tc(VII) is much higher at higher pH than at pH ~6, in agreement with the pH dependent data. In both cases, data is linear at lower [Tc_{eql}]. At higher [Tc_{eql}], the sorption increased more steeply.

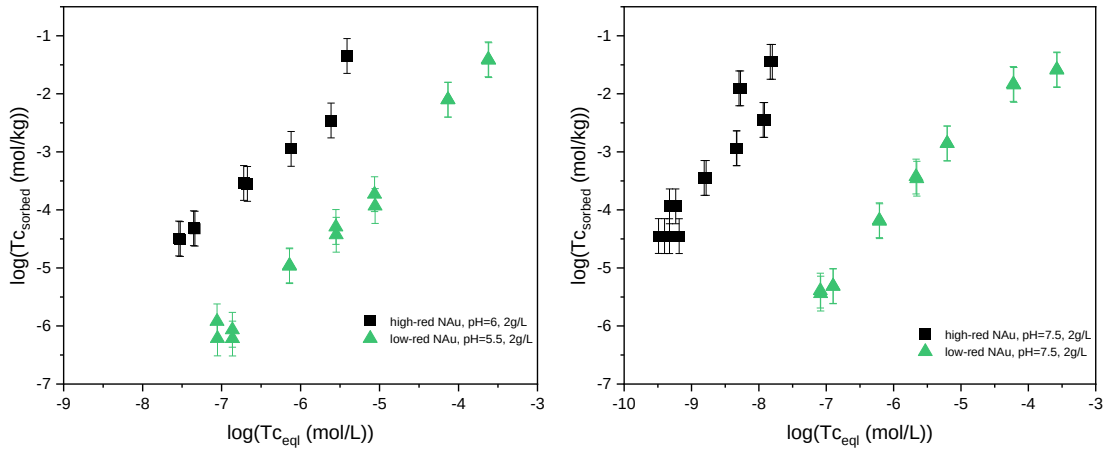

Figure 52. Tc(VII) sorption as function of Tc concentrations on high-red NAu-2 and low-red NAu-2 at S/L in 0.1 M NaCl at a) pH ~5.5 -6 and b) pH 7.5 after 7 days.

EXAFS measurements were performed on low and high-red Nau-2 samples at different pH and different Tc loadings (Figure 53) to characterize the Tc surface species. In all cases i.e., clay form, pH and Tc loadings, only $TcO_2 \cdot nH_2O$ could be identified.

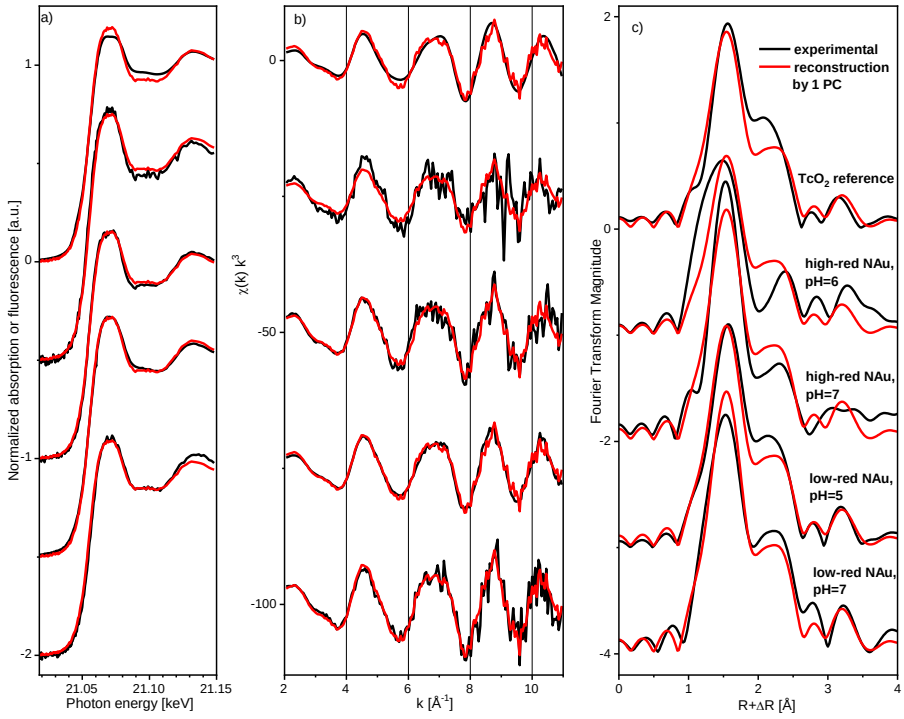

Figure 53. Tc K-edge XANES (left) and EXAFS (right) spectra on low and high-red Nau-2 in the pH range 5 to 7 and the TcO_2 reference spectra. Inset (right): black lines, experimental data; red lines, reconstruction by two components.

3.2.3 Towards mixtures of smectite and Fe-phases [CIEMAT]

To elucidate the role of accessory Fe and to evaluate possible kinetic effects on ^{99}Tc(VII) retention, [CIEMAT] carried out ^{99}Tc(VII) batch sorption tests in raw NAu-1 suspended in $NaClO_4$ 0.1 M, fixing the at pH 8, including the presence of 5% in weight of different Fe sources: commercial metallic Fe(0) (MERCK), commercial hematite (Fe_2O_3) from Sigma Aldrich and laboratory synthetized magnetite (Fe_3O_4). For sorption experiments, contact times varied from 7 up to 200 days. The pH and Eh of samples was periodically measured. ^{99}Tc sorption in NAu-1 was negligible under studied conditions and remained null in most of the systems analysed, except for the NAu-1 samples where 5% of Fe(0) shavings were added where significant ^{99}Tc distribution coefficients were measured (Figure 54), indicating redox induced retention.

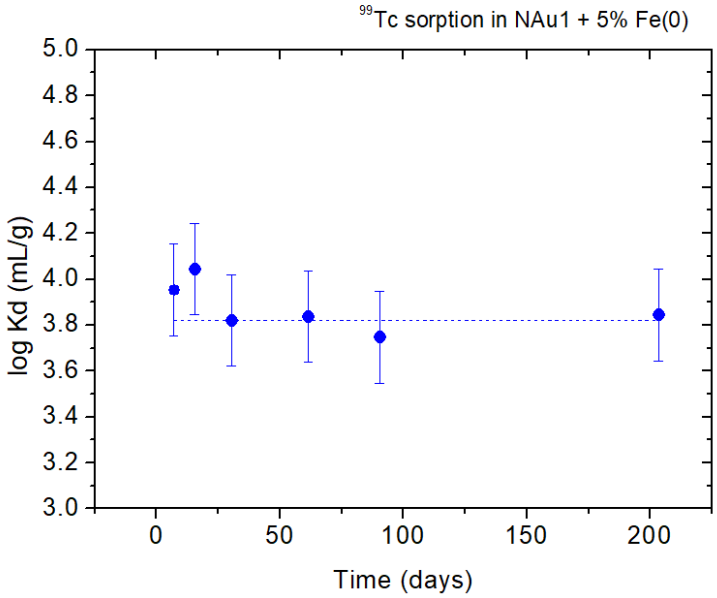

Figure 54. ^{99}Tc(VII) sorption on NAu-1 in presence of 5% of metallic Fe(0) shavings, measured under anoxic conditions as a function of time.

Nature of the $TcO_2 \cdot nH_2O$ as determined by DFT and Tc interaction with magnetite was performed at [HZDR]. Previous sections have highlighted that Tc interaction with Fe-rich solids induce Tc reduction, and precipitation of TcO_2. However, due to its minute size, its structure has up to know remained elusive. This was investigated here with DFT. In addition, the nature of Tc interaction with magnetite was studied to gain better insights into its interactions between Fe-rich solids.

3.2.3.1 Introduction

[HZDR] Previous investigations have shown that aqueous pertechnetate is easily reduced by pristine magnetite to its tetravalent oxidation state, forming a mixture of $TcO_2 \cdot xH_2O$ associated or not with the magnetite surface, and Tc(IV) incorporated by magnetite by occupying octahedral Fe sites of the magnetite structure, all three processes sequestering Tc from solution to solid phases (Kobayashi et al., 2013; Marshall et al., 2014; Yalçıntaş et al., 2015; Yalçıntaş et al., 2016). In the context of EURAD-FUTURE, the work at HZDR centred around three main questions in this context:

(1) What is the exact structure of the $TcO_2 \cdot xH_2O$ precipitate?

(2) Is $TcO_2 \cdot xH_2O$, or small dimeric or trimeric clusters of it, attaching to magnetite by forming chemical bond(s) with the surface?

(3) How can a sorbate (Tc) be so rapidly (within days) incorporated by a rather insoluble sorbent (magnetite) and what is controlling the extent of the competing reaction, namely the precipitation of $TcO_2 \cdot xH_2O$?

All three questions were tackled by a combination of careful (strictly anoxic) wet chemistry experiments, X-ray absorption fine-structure (XAFS) spectroscopy and atomistic simulations based on density functional theory (DFT).

3.2.3.2 (1) The structure of the $TcO_2 \cdot xH_2O$ precipitate (Oliveira et al., 2022)

Under the conditions of deep nuclear waste repositories, Tc is retained through biotic and abiotic reduction of TcO_4^- to compounds like amorphous $TcO_2 \cdot xH_2O$ precipitates. It is generally accepted that these precipitates consist of linear $(Tc(\mu\text{-}O)_2(H_2O)_2)_n$ chains, with H_2O at trans positions. Although corresponding Tc-Tc and Tc-O distances have been obtained from EXAFS spectroscopy, this structure is largely based on analogy with other compounds. Here, by combining DFT calculations and EXAFS measurements of fresh and aged $TcO_2 \cdot xH_2O$ samples, we show that $TcO_2 \cdot xH_2O$ forms zigzag chains with H_2O groups in *cis*- configuration. Moreover, these chains undergo a very slow aging process whereby they form longer chains and, later, a tridimensional structure that could eventually result in a new TcO_2 polymorph, analogous to β-ReO_2 (Oliveira et al., 2022).

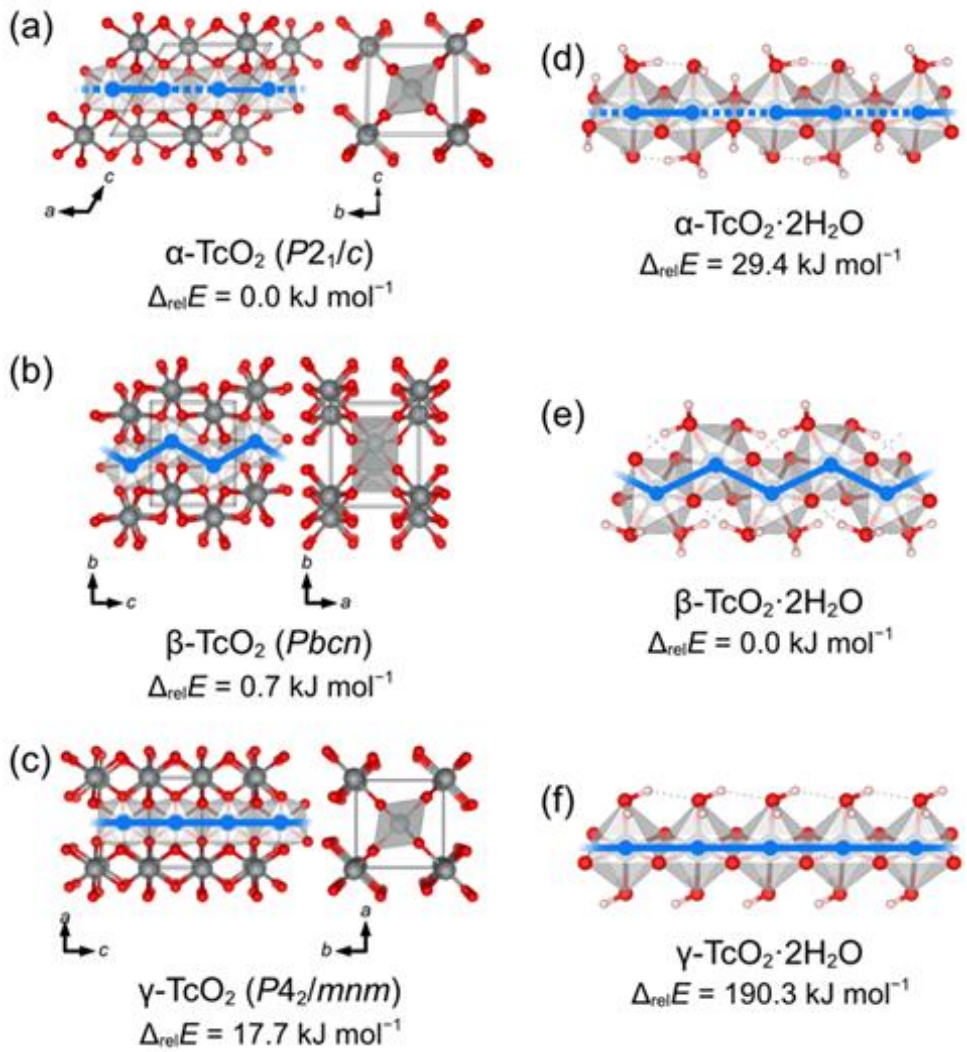

Figure 55. Optimized structures of TcO_2 crystal polymorphs and related $TcO_2 \cdot 2H_2O$ chains. Tc atoms represented as octahedra emphasize the structure of laterally interconnected chains in the TcO_2 crystals. The blue lines emphasize the linear and zigzag paths of the chains, with dashed lines indicating the longer Tc-Tc distances. During optimization of α-$TcO_2 \cdot 2H_2O$, a few H atoms migrated from H_2O groups to μ-O bridges. The $\Delta_{rel}E$ values correspond to the relative energies per formula unit.

The DFT calculations clearly show the zigzag chain – β-$TcO_2 \cdot 2H_2O$ – as the most energetically favoured (Figure 55). The Tc-O bond lengths are characteristic of the O configuration (terminal, bridged, protonated, unprotonated), while Tc-Tc distances allow to unambiguously discriminate the three chain configurations (Table 21). Indeed, simulated EXAFS spectra for α-, β-, and γ-$TcO_2 \cdot 2H_2O$ chains differ considerably from each other, with β-$TcO_2 \cdot 2H_2O$ giving the best match to the experimental spectra of the fresh and aged samples (Figure 57). Moreover, as shown in Figure 56, Tc-O and Tc-Tc distances obtained from EXAFS fittings are in excellent agreement with the optimized β-$TcO_2 \cdot 2H_2O$ chain, especially for the aged sample, for which high frequency signals (absent in the fresh sample) could be fitted to second and third Tc-Tc intrachain shells and to interchain distances compatible with the β-TcO_2 crystal. Therefore, our data suggest that small zigzag chain units form initially, which then continue to age, polymerizing by dehydration into a loose tridimensional network. Eventually, a new β-type TcO_2 polymorph may form.

Table 21. Tc coordination numbers (CN) and interatomic distances (R) from EXAFS shell fitting of fresh and aged $TcO_2 \cdot xH_2O$ samples along with the values obtained from DFT for the $TcO_2 \cdot 2H_2O$ chains and TcO_2 crystals. The CN values for the Tc-Tc interchain distances consider only one neighbouring chain.

	Exptl. EXAFS(shell fitting)				DFT calculations						DFT calculations					
	$TcO_2 \cdot xH_2O$ precipitates				**Infinite chains**						**Crystal structures**					
	Fresh[a]		**Aged[b]**		**α-$TcO_2 \cdot 2H_2O$**		**β-$TcO_2 \cdot 2H_2O$**		**γ-$TcO_2 \cdot 2H_2O$**		**α-TcO_2**		**β-TcO_2**		**γ-TcO_2**	
Shell	CN	R/Å	CN	R/Å	CN	R/Å	CN	R/Å	CN	R/Å	CN	R/Å	CN	R/Å	CN	R/Å
Tc-(μ-O)	4[f]	2.01	4[f]	2.01	2 2	1.93 2.11[d]	4	1.98	4	1.97	6	2.01	6	2.01	6	2.00
Tc-OH_2	2[f]	2.39	2[f]	2.14	1 1	2.04[e] 2.17	2	2.23	2	2.24	—	—	—	—	—	—
Tc-Tc (intrachain)	2[f]	2.55	2[f] 0.6 4.2	2.54 4.63 7.03	1 1 2	2.34 3.38 5.71	2 2 2	2.53 4.60 6.98	2 2 2	2.90 5.80 8.70	1 1 2	2.62 3.12 5.73	2 2 2	2.64 4.71 7.16	2 2 2	2.84 5.68 8.53
Tc-Tc (interchain)	—	—	0.8 1.2 2.5	3.80 5.06 6.04	—	—	—	—	—	—	2 1 1	3.68 5.24 5.44	2 2 2	3.72 5.26 6.00	2 2 2	3.68 5.46 7.88

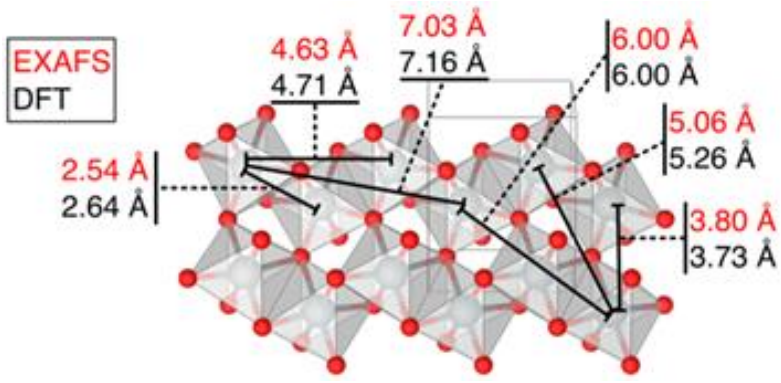

Figure 56. Tc-Tc distances for $TcO_2 \cdot xH_2O$. EXAFS values were obtained from the spectrum of the aged sample. Intra- and interchain values for DFT come from to the optimized structure of the β-$TcO_2 \cdot 2H_2O$ chain and β-TcO_2 crystal. The excellent agreement between EXAFS and DFT indicates that $TcO_2 \cdot xH_2O$ consists of zigzag chains that slowly age into longer chains, eventually forming tridimensional structures.

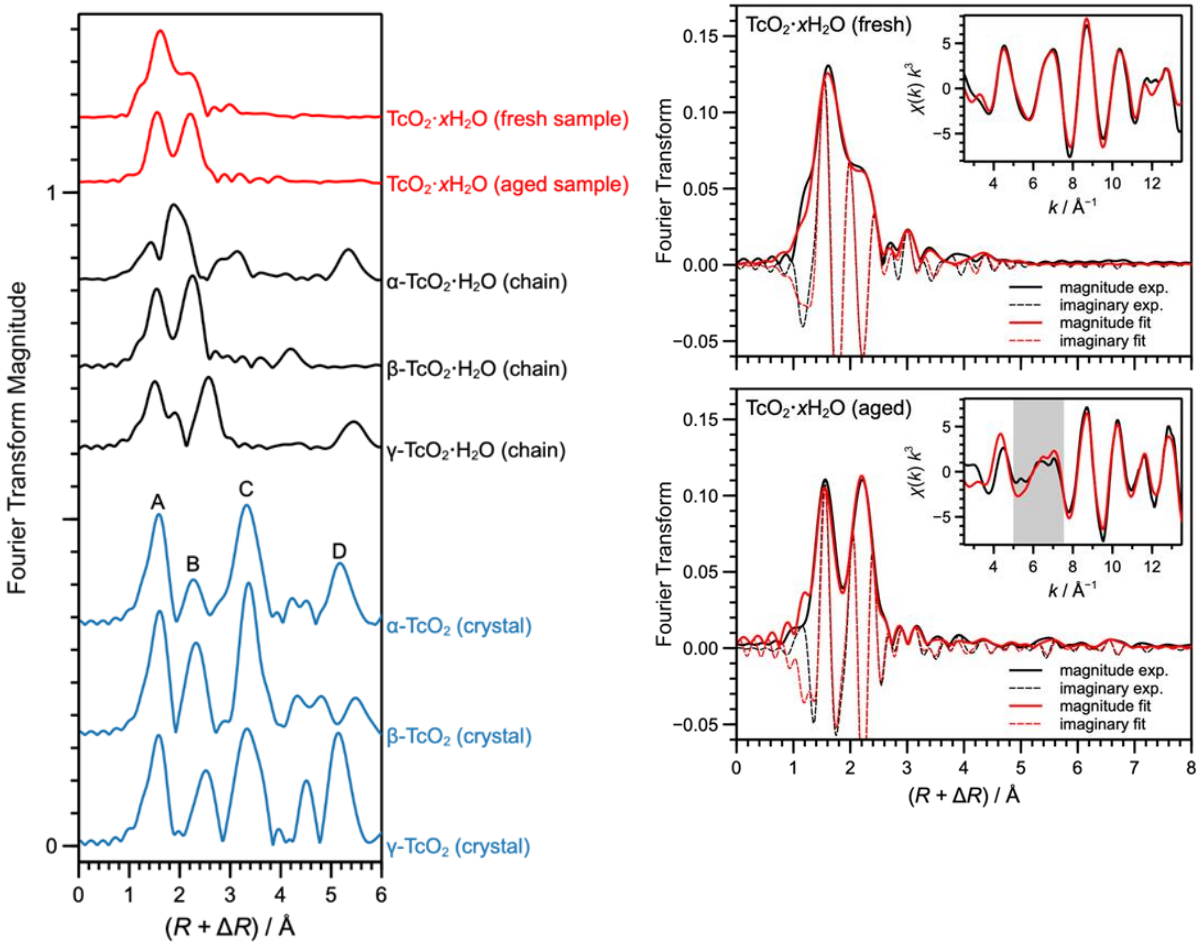

Figure 57. (left) Fourier-transform magnitudes (FTMs) from experimental EXAFS spectra of the fresh and aged $TcO_2{\cdot}xH_2O$ precipitates (red curves) and from EXAFS spectra simulated with FEFF9.6.4[17] for the $TcO_2{\cdot}H_2O$ infinite chains (black curves) and TcO_2 crystal structures (blue curves) optimized with DFT. The fresh sample was measured within a month after preparation; the aged sample was stored for four years under ambient conditions prior to the measurement. The geometry of α-$TcO_2{\cdot}H_2O$ converged to a mixed protonation state, as shown in Figure 55d. For the TcO_2 crystals, peak A is associated with the first Tc-O coordination shell, B with the nearest intrachain Tc-Tc neighbours, C with the nearest interchain Tc-Tc neighbours, and D with the second intrachain Tc-Tc neighbours. (right) Experimental EXAFS spectra of fresh (top) and aged (bottom) $TcO_2{\cdot}xH_2O$ samples (black traces) and their reproduction by shell fitting (red traces). The main plots show the Fourier transform magnitude (bold lines) and the imaginary part (thin lines); the inserts show the corresponding k^3-weighted $\chi(k)$ -spectra (the shadowed region indicates high-frequency signals absent in the fresh sample). The shell fit of the fresh sample is based on the DFT-derived structure of β-$TcO_2{\cdot}H_2O$ chain, the shell fit of the aged sample is based on the DFT-derived structure of the β-TcO_2 crystal. The fitted parameters are compiled in Table 21.

3.2.3.3 (2) Is $TcO_2{\cdot}xH_2O$, or small dimeric or trimeric clusters of it, attaching to magnetite by forming chemical bond(s) with the surface? (Bianchetti et al., 2023)

We investigated the chemistry of $Tc^{VII}O_4^-$ and Tc^{IV} species at the magnetite (001) surface through a hybrid DFT functional (HSE06) method. First, we studied a possible initiation step of the Tc^{VII} reduction process. The interaction of the $Tc^{VII}O_4^-$ ion with the magnetite surface leads to the formation of a reduced Tc^{VI} species without any change in the Tc coordination sphere, through an electron transfer that is

favoured by the magnetite surfaces with a higher Fe^{II} content. Second, we explored various model structures for the immobilized Tc^{IV} final products. Tc^{IV} can be incorporated into a subsurface octahedral site or adsorbed on the surface in the form of $Tc^{IV}O_2 \cdot xH_2O$ chains. We propose and discuss three model structures for the adsorbed $Tc^{IV}O_2 \cdot 2H_2O$ chains in terms of relative energies and simulated EXAFS spectra. Our results suggest that the periodicity of the magnetite (001) surface matches that of the $TcO_2 \cdot 2H_2O$ chains. The EXAFS analysis suggests that in experiments $TcO_2 \cdot xH_2O$ chains were probably not formed as an inner-sphere adsorption complex with the magnetite (001) surface, but rather with the magnetite (111) surface as previously shown for sorption of Pu, Sb and As (Dumas et al., 2019; Kirsch et al., 2011; Kirsch et al., 2008; Wang et al., 2021).

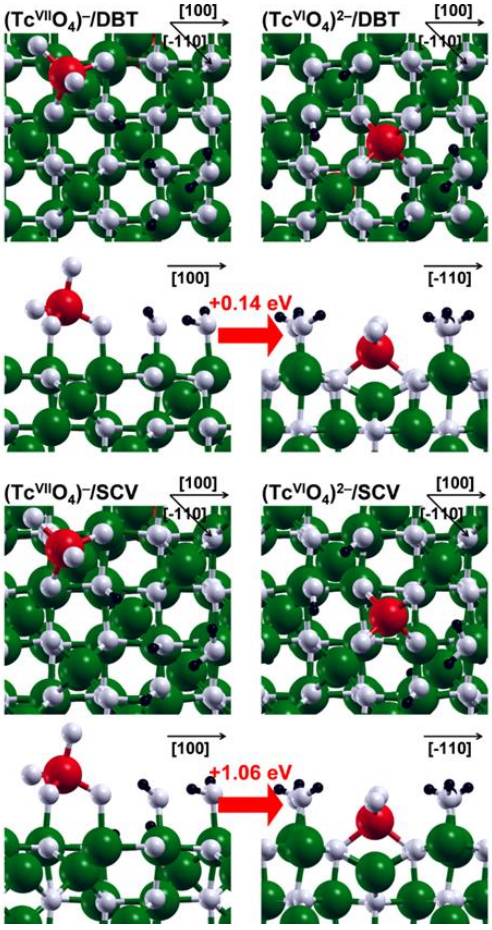

Figure 58. Top and side views of the optimized structures for the lowest-energy TcO_4^{n-} complexes adsorbed onto the Fe_3O_4(001) surfaces. DTB designates a Distorted Bulk Truncation termination (top) and SCV a subsurface Cation Vacancy Termination (bottom). The black, white, green, and red beads represent H, O, Fe, and Tc, respectively. The black arrows indicate the crystallographic directions.

In the first part of this study, we simulated the interaction of TcO_4^{n-} species with the magnetite (001) surface by considering that the ions may either just adsorb by binding to undercoordinated surface Fe ions or become involved in surface reaction/reconstruction leading to their surface embedding. For both DBT and SCV surfaces, we have selected the two lowest energy adsorption complexes, shown in Figure 58. In the models reported in the left panels (referred to as $(Tc^{VII}O_4)$–/DBT and $(Tc^{VII}O_4)$–/SCV, as discussed below), TcO_4^{n-} is adsorbed on two penta-coordinated Fe_{Oct} of the surface through two µ-O (i.e., two-fold coordinated oxygen) bridging atoms. In the models shown in the right panels (referred to as $(Tc^{VI}O4)_2$–/DBT and $(Tc^{VI}O_4)_2$–/SCV, as discussed below), TcO_4^{n-} becomes embedded in the surface through two µ4-O (i.e., four-fold coordinated oxygen) bridging atoms. This second adsorption site is the same that is generally preferred by single metal atoms adsorbed on the magnetite (001) surface, according to several recent studies (Bliem et al., 2015; Hulva et al., 2021).

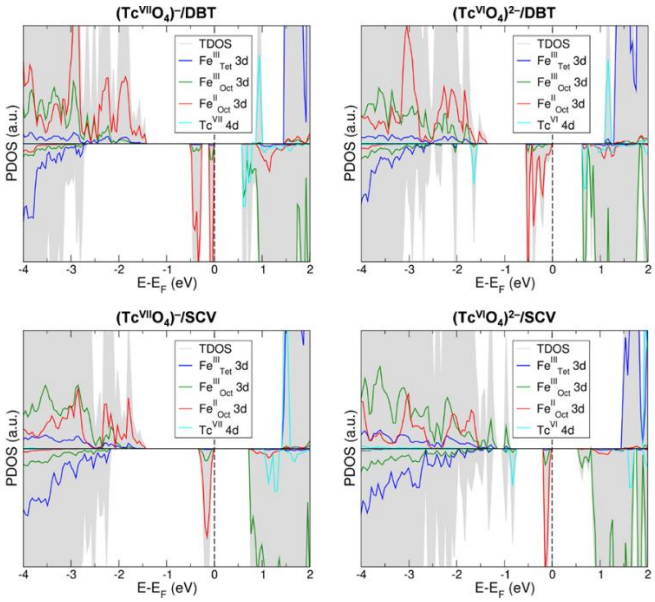

Figure 59. PDOS for the lowest-energy TcO_4^{n-} complexes adsorbed onto the DBT (on the top) and SCV (on the bottom) Fe_3O_4(001) surfaces, shown in Figure 58.

$(Tc^{VII}O_4)^-$/DBT and $(Tc^{VII}O_4)^-$/SCV models are characterized by the presence of technetium in its VII oxidation state. As we can see in the PDOS (Figure 59), there are no Tc 4d states (Figure 59, cyan curve) in the valence band. All technetium 4d orbitals are in the conduction band. Furthermore, Tc is characterized by almost null spin polarization. These findings are compatible with a Tc^{VII} species, corresponding to the electronic configuration [Kr]. On the other hand, in $(Tc^{VI}O_4)^{2-}$/DBT and $(Tc^{VI}O_4)^{2-}$/SCV models, we observe that Tc^{VII} is reduced to Tc^{VI} while two Fe^{II} in the fifth and in the seventh layer of the magnetite surface are oxidized to Fe^{III}. The reduction of Tc^{VII} to Tc^{VI} is in line with the Mulliken charge decrease of 5%, and with a new Tc 4d contribution to the valence band in the spin-down channel of the PDOS (Figure 59, cyan curve). Indeed, the Mulliken spin density value of -0.7 μ_B for Tc in both $(Tc^{VI}O_4)^{2-}$/DBT and $(Tc^{VI}O_4)^{2-}$/SCV is consistent with a Tc^{VI} species with electronic configuration $[Kr]4d^1$, i.e., with one unpaired electron. The Fe^{II} (high spin $[Ar]d^6$ configuration) oxidation to Fe^{III} (high spin $[Ar]d^5$ configuration) is confirmed by the Mulliken charge and spin density increase of 15% and from 3.7 to 4.2 μ_B, respectively. Despite the similar structural properties of the DBT and SCV adsorption complexes, the redox energies differ considerably: the reaction energy per Tc atom is 1.06 eV for $(Tc^{VII}O_4)^-$/SCV → $(Tc^{VI}O_4)^{2-}$/SCV and 0.14 eV for $(Tc^{VII}O_4)^-$/DBT → $(Tc^{VI}O_4)^{2-}$/DBT. The Tc^{VII} reduction to Tc^{VI} is more favourable on the DBT surface than on the SCV surface. This may be mainly due to two reasons: firstly, the DBT surface presents a higher content of Fe^{II} ions in comparison to the more oxidized SCV one; secondly, the electron transfer from one Fe^{II} centre to the Tc^{VII} ion implies the formation of an electrical dipole which is smaller on the DBT than on the SCV surface, since the distances between the Tc^{VII} ion and the Fe^{II} centres involved in the reduction to Tc^{VI} are found to be about 6 and 8 Å, respectively.

The reduction of Tc^{VII} to Tc^{VI} by a *simple* electron transfer (from the magnetite surface to the technetium atom) is likely the first step of a *complex* redox process, which is known to proceed rapidly, producing Tc^{IV} end-members at slightly alkaline pH. The process involves the oxidation of Fe^{II} close to the Tc adsorbate, changing the Tc geometry from tetrahedral to octahedral – similarly to what happens during the reduction of $Mn^{VII}O_4^-$ to $Mn^{IV}O_2$, passing through $Mn^{VI}O_4^{2-}$.Given the complexity of the process and the lack of more specific information regarding the chemical species involved, the simulation of the full $Tc^{VII}O_4^-$ reduction is out of the scope of this work. Therefore, we restrict our study to hypothetical final products: incorporation of Tc^{IV} in the magnetite slab and formation of $Tc^{IV}O_2{\cdot}xH_2O$ chains adsorbed on the magnetite surface.

An alternative surface reactivity discussed in the literature would lead to the formation of hydrated $Tc^{IV}O_2$ dimers or chains on the magnetite surface (Marshall et al., 2014; Wang et al., 2021; Yalçıntaş et al.,

2016). To study this possibility, we first investigated a free-standing $TcO_2 \cdot 2H_2O$ chain. The β-$TcO_2 \cdot 2H_2O$ chain was found to be the most stable chain, with Tc-Tc and Tc-O distances of ca. 2.4 and 1.9 Å, respectively. The α-$TcO_2 \cdot 2H_2O$ chain was found to be less stable by +758 meV per Tc atom (Table 22), with alternating Tc-Tc distances of ca. 2.2 and 3.3 Å. Consequently, also Tc-O distances present alternating values: 1.9 Å when O is bridging Tc-Tc at smaller distance and 2.1 Å when bridging the Tc-Tc at longer separation. The γ-$TcO_2 \cdot 2H_2O$ transformed to the α-chain during the geometry optimization.

Table 22. Relative total energies per Tc atom (in meV) of the α-$TcO_2 \cdot 2H_2O$, β-$TcO_2 \cdot 2H_2O$, and γ-$TcO_2 \cdot 2H_2O$ chains in vacuum and adsorbed onto the SCV magnetite (001) surface.

	α-$TcO_2 \cdot 2H_2O$	β-$TcO_2 \cdot 2H_2O$	γ-$TcO_2 \cdot 2H_2O$
Vacuum	+758	0	-
Adsorbed on SCV Fe_3O_4(001)	+16	+343	0

As a next step, we investigated the interaction between the $TcO_2 \cdot 2H_2O$ chains with the magnetite surface. The periodicity of the magnetite surface and, in particular, of the alternating O-O distances along the [-110] direction, matches that of the α-$TcO_2 \cdot 2H_2O$ chain. The adsorbed α-$TcO_2 \cdot 2H_2O$ chain (Figure 60, α-$TcO_2 \cdot 2H_2O$/SCV) presents only one kind of Tc (Figure 60, red beads), that is six-coordinated by four O from the chain itself (Figure 60, blue beads), one O shared with magnetite, and one O from a water molecule (Figure 60, white beads). Half of the O bridges in the chain (indicated with a yellow star in Figure 5) interacts with exposed undercoordinated Fe (Figure 60, green beads). The adsorption is driven by two types of interaction: one between Tc^{IV} and magnetite O, and the other between surface Fe^{III} and O belonging to $TcO_2 \cdot 2H_2O$ chains. α-$TcO_2 \cdot 2H_2O$/SCV presents different alternating Tc-Tc distances with respect to the free-standing chain: ca. 2.8 and 3.1 Å versus 2.2 and 3.3 Å. This significant difference is due to the periodicity of the magnetite surface and, in particular the alternating O-O distances along the [-110] direction, i.e., the direction along which the α chain is adsorbed. Perpendicularly to the [-110] direction the surface periodicity is significantly different. In particular, the periodicity of the almost constant O-O distances along the magnetite [110] direction matches that of the γ-$TcO_2 \cdot 2H_2O$ chain, which was not stable in vacuum. The adsorbed γ-$TcO_2 \cdot 2H_2O$ chain (Figure 60, γ-$TcO_2 \cdot 2H_2O$/SCV) presents only one kind of Tc, whose coordination sphere is analogue to the one in α-$TcO_2 \cdot 2H_2O$/SCV. Still in analogy to α-$TcO_2 \cdot 2H_2O$/SCV, half of the O atoms in the chain are interacting with superficial undercoordinated Fe. These structural similarities are translated into comparable energies: the total energies difference between the adsorbed γ and α chain is only 16 meV per Tc atom (as reported in Table 22), in favour of the former.

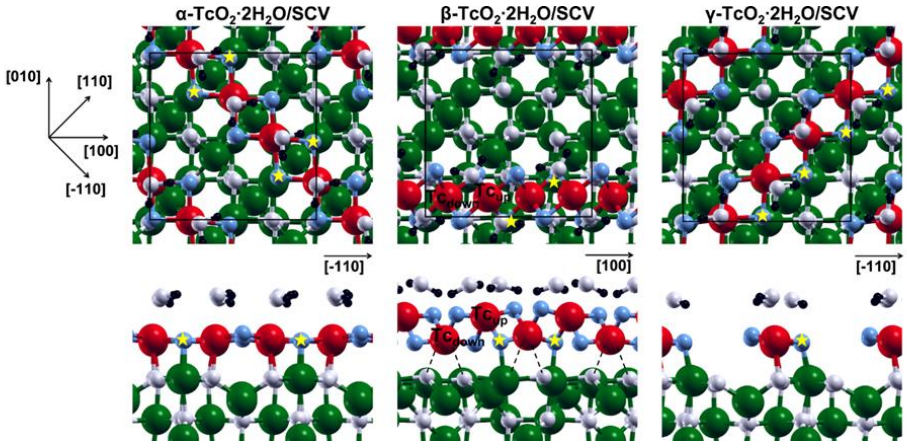

Figure 60. Top and side views of the optimized structures for the α-$TcO_2 \cdot 2H_2O$, β-$TcO_2 \cdot 2H_2O$, and γ-$TcO_2 \cdot 2H_2O$ (from left to right) chains adsorbed onto the SCV magnetite (001) surface. The axis orientation for all the top views is shown on the left of the figure, whereas for the side views it is shown in each single panel. The black, white, blue, green, and red beads represent H, O belonging to water molecules and magnetite, O belonging to TcO_2, Fe, and Tc, respectively. The yellow stars indicate O from the chains interacting with surface Fe. Black dashed lines indicate weak Tc-O interactions.

The free-standing β chain has a shorter lattice parameter than the α and γ chains due to its zigzag configuration. Consequently, it is not possible to efficiently adsorb the β-$TcO_2 \cdot 2H_2O$ along the diagonal direction of the cell as previously done for the α and γ one. Therefore, we studied the adsorption of the β-$TcO_2 \cdot 2H_2O$ along the [100] direction (Figure 60, β-$TcO_2 \cdot 2H_2O$/SCV). In this case, two different kinds of Tc are present: one farther from the surface and one closer to it, labelled as Tc_{up} and Tc_{down} in Figure 60, respectively. Both Tc_{up} and Tc_{down} species are six-coordinated. Each Tc_{up} is coordinated by four O from the chain itself and by two O from two different water molecules, whereas each Tc_{down} is coordinated by four O from the chain itself and by two O shared with magnetite (Figure 60, dashed lines). Tc-Tc distances and other structural parameters of the adsorbed chain are not significantly different from what is observed for the free-standing chain. This configuration is found to be less favoured than the α and γ one by +327 and +343 meV per Tc atom (see Table 22), respectively. This is an unexpected result, since the β-$TcO_2 \cdot 2H_2O$ chain is the most stable one in vacuum. This finding can be understood in terms of the (i) lower number (half compared to α and γ cases) of chain O atoms interacting with the magnetite surface and (ii) weaker Tc-O interactions (2.3-2.4 versus 1.9-2.0 Å for the α and γ chains) between the chain and the magnetite surface.

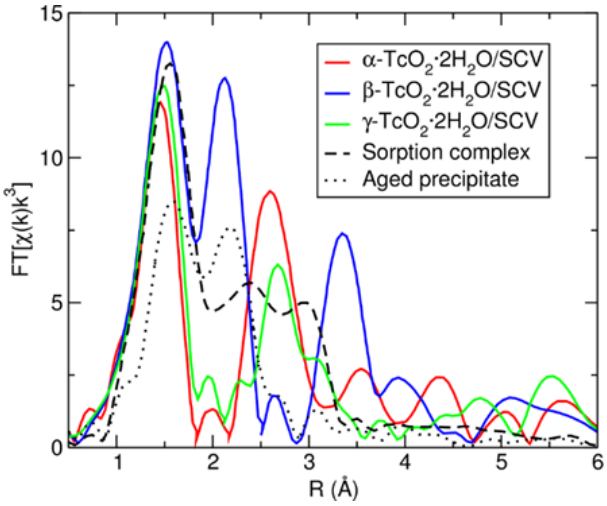

Figure 61. Experimental EXAFS spectra for the sorption complex by (Yalçıntaş et al., 2016)(black dashed line) and aged $TcO_2 \cdot xH2O$ precipitate by (Oliveira et al., 2022) (black dotted line), and simulated EXAFS spectra for the α-$TcO_2 \cdot 2H_2O$ (red line), β-$TcO_2 \cdot 2H_2O$ (blue line), and γ-$TcO_2 \cdot 2H_2O$ (green line) chains adsorbed onto the SCV magnetite (001) surface.

Finally, we compared the experimental EXAFS spectra for the sorption complex by (Yalçıntaş et al., 2016) (Figure 61, black dashed curve) and for the aged $TcO_2 \cdot xH_2O$ precipitate by (Oliveira et al., 2022)(Figure 61, black dotted curve) with the calculated EXAFS spectra obtained for the simulated $TcO_2 \cdot 2H_2O$ chains adsorbed on the magnetite (001) surface just described. Regarding the experimental sorption complex curve, there is no match with the calculated curves of the simulated $TcO_2 \cdot 2H_2O$ chains models. We also modelled a magnetite/TcO_2-dimer complex in line with what suggested by (Yalçıntaş et al., 2016). However, also in this case, the simulated EXAFS spectrum does not match the experimental one for the sorption complex. These results suggest that TcO_2 chains (or dimers) are probably not formed as an inner-shell adsorption complex with the magnetite(001) surface, at least not immediately. Regarding the aged $TcO_2 \cdot xH_2O$ precipitate curve, there are few similarities with the calculated β-$TcO_2 \cdot 2H_2O$/SCV curve (Figure 61, blue curve). In particular, the positions of the first and second peak are in fair agreement, as well as the presence of a small shoulder on the right of the second peak, but the third peak in the computed curve finds no correspondence in the experimental one. This result suggests that β-$TcO_2 \cdot 2H_2O$ chains might be formed in solution, not as an inner-shell adsorption complex with magnetite, and only afterward might precipitate and adsorb on the surface. Indeed, the formation of β-$TcO_2 \cdot 2H_2O$ chains is energetically favoured over that of the α and γ ones in vacuum, not on the Fe_3O_4(001) surface. However, the agreement between the experimental aged precipitate curve

and the computed β-$TcO_2 \cdot 2H_2O$/SCV one is not good enough to definitively sustain this hypothesis. Therefore, the comparison between the experimental and the calculated data suggests the possibility that in the experiments completely different surfaces, such as the (111), not considered in this work, might be involved, as previously shown for sorption of Pu, Sb and As (Dumas et al., 2019; Kirsch et al., 2011; Kirsch et al., 2008; Wang et al., 2021).

3.2.3.4 (3) How can Tc be rapidly incorporated by magnetite and what is controlling the extent of competing reactions?

Here we conducted a series of Tc sorption experiments as a function of pH (5, 7, 10) and time (from 1 d to 7 weeks), supplemented by Tc-magnetite coprecipitation experiments, and investigated chemical parameters of the aqueous phase (Tc, Fe, pH, Eh) as well as structural data (XANES, EXAFS, XRD, TEM) of the solid phase. We find that Tc is fully reduced to Tc(IV) under all conditions after 1 d reaction time. Tc(IV) is incorporated by magnetite already after 1 d at pH 10, while both pH 5 and 7 samples indicate that first β-$TcO_2 \cdot 2H_2O$ forms, which gradually converts into the incorporated species over time. Possible reasons for the pH-depending differences in reaction mechanism are discussed. Possible charge balance mechanisms are further evaluated by DFT calculation.

Figure 62 shows the results of the sorption experiment from pH 2 to 13 after four weeks of equilibration time. While Tc removal (blue squares in Figure 62) is close to zero for pH values below 3, it becomes higher than 98 % for pH > 5.0 (note that no value was obtained for pH 4). The transition from no to almost complete Tc uptake is accompanied by a decrease of Eh (red circles in Figure 62), which remains above the Tc^{VII}/Tc^{IV} predominance line up to pH 3, then falls below for pH 4 and higher. This suggests that no reduction of $Tc^{VII}O_4^-$ occurs at pH < 4.5 and hence, all Tc remains in solution, while $Tc^{VII}O_4^-$ reduction occurs above pH 5, with nearly all Tc^{IV} removed from solution.

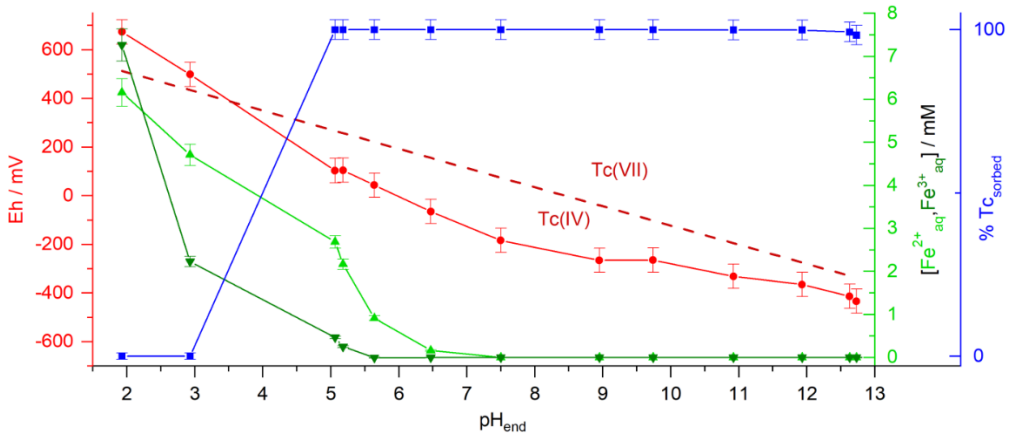

Figure 62. Tc^{VII} removal (% Tc sorbed, blue squares), redox potential (Eh, red circles), $[Fe^{2+}]_{aq}$ (green triangles) and $[Fe^{3+}]_{aq}$ (dark green triangles) as a function of pH after 4 weeks of Tc ($[Tc]_0$= 24 µmol/L / 600 ppm) sorption to magnetite suspension (4 g/l). The dashed line represents the predominance line for Tc^{VII} above and Tc^{IV} below.

Magnetite is known to leach Fe^{II} at low pH, undergoing a phase transition to maghemite ($[\square Fe_5^{III}](Fe_3^{III})O_{12}$; □ is a vacancy) at pH < 7.0, known as maghemitization (Ozdemir and Dunlop, 2010). Structural Fe^{II} can dissolve from magnetite, leaving vacancies in the solid structure to compensate the charge deficiency, leading to minor structural reordering and formation of maghemite. At pH 7 barely any and at pH 10 no maghemitization occurs, leaving all structural Fe^{II} available for the fast reduction of Tc^{VII}. This is demonstrated by the high amounts of Fe^{2+} (green triangles in Figure 62) and Fe^{3+} in solution (dark green triangles in Figure 62), the magnetite partly dissolved at pH 1.9, 2.9 and 5.0 over time with Fe^{3+} being only observed at $pH_{end} \leq 5.2$. Furthermore, the originally black suspension turned into brownish hue for pH 2.0 and 3.0, while after the final pH equilibration, barely enough solid was available for further solid analysis. Experiments set at pH_{ini} 4.0 and 5.0 resulted in similar pH_{end} and Eh, but higher

[Fe^{II}] for pH_{ini} 4.0. This is due to the higher dissolution of Fe^{II} at pH_{ini} 4.0. At pH_{ini}> 7.0, no Fe was measured in the supernatant.

The kinetics of Tc sorption experiments were investigated at pH 5.0, 7.0 and 10.0 up to 49 days of equilibration time (Figure 63). After one day, all Tc was removed from the supernatant at all pH values. Investigations of fast kinetics show more than 90 % Tc was removed after 30 min of contact. The observed shifts of the pH are like the ones from the pH series, namely a rise at pH 5.0, a decrease at pH 7.0 and no change at pH 10.0. At pH 10.0, no Fe is observed throughout the time range, while $[Fe^{2+}]_{aq}$ increases with time at pH 5.0 and 7.0, having a lower threshold at pH 7.0. Additionally, Fe^{3+} is measured in solution at pH 5.0 after four weeks. This indicates that either magnetite particles are dissolving or trace amounts of O_2 in the glovebox can oxidize dissolved Fe^{II}.

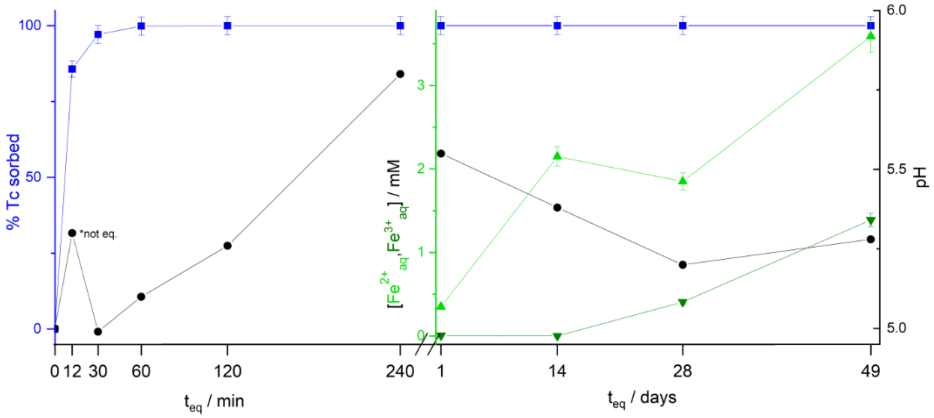

Figure 63. Tc^{VII} removal (% Tc sorbed, blue squares), pH values (black circles), $[Fe^{2+}]_{aq}$ (green triangles) and $[Fe^{3+}]_{aq}$ (dark green triangles) as a function of time in contact with Tc (t_{eq}) for samples at pH 5.0. The left side shows the short kinetics up to 4 hours ([Tc]0= 3 µM / 600 ppm; S/L=0.5 g/l) and the right side the long kinetics of 1 day up to 49 days ([Tc]0= 24 µM / 600 ppm; S/L=4 g/l).

Figure 64 compiles the XAFS spectra of Tc sorption and coprecipitation samples along with a $TcO_2{\cdot}xH_2O$ reference corresponding to the “fresh precipitate” in (Oliveira et al., 2022). Both experimental XANES and EXAFS parts (black lines) could be reconstructed by two spectral components (red lines), indicating that all sorption and coprecipitation samples contain only two, structurally (and eventually electronically) different Tc species, one of them being the β-$TcO_2{\cdot}xH_2O$ reference. While the absence of any pre-edge peak in the XANES spectra indicates that all pertechnetate has been reduced, the white line peak position is in line with Tc(IV), demonstrating the complete (≥ 95%) reduction of solid-associated Tc from (VII) to (IV). Reconstruction by two components is required to account for the splitting of the white line peak, which is absent in the β $TcO_2{\cdot}xH_2O$ reference, and mostly expressed for the high-pH sorption and coprecipitation samples.

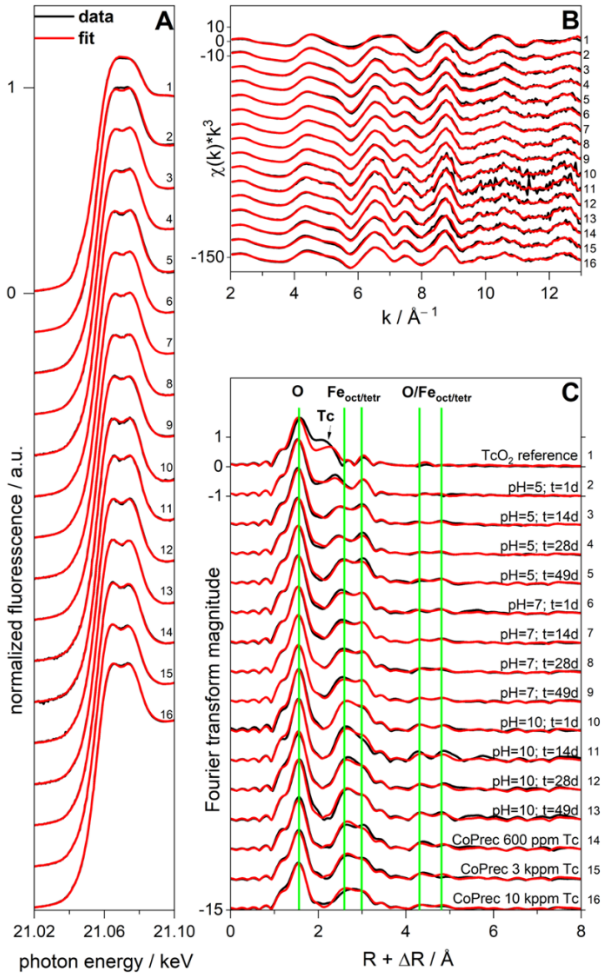

Figure 64: Tc-K-edge XAFS spectra of Tc sorption and coprecipitation samples. (A) XANES; (B) k^3 weighted EXAFS χ(k) spectra; (C) corresponding Fourier transform magnitude. Black lines represent the experimental data, the red line their reconstruction with two principal components.

Since the EXAFS spectra represent a superposition of two spectral components, one of them the $TcO_2{\cdot}xH_2O$ reference, they are difficult to analyse by shell fitting due to the EXAFS-inherent limited resolution of individual shells. Therefore, we employed the VARIMAX and iterative target test modules of the ITFA package (Rossberg et al., 2003; Yalçıntaş et al., 2016) to isolate the EXAFS spectra of the two endmember components (Figure 65).

One component shown in the right-hand part corresponds largely to the spectrum of the $TcO_2{\cdot}xH_2O$ reference, with some noise-reduction because it is extracted from the set of all 16 spectra shown in Figure 64. Its shell fit parameters are shown in Table 23. The local radial structure agrees well with a shell fit of the "fresh $TcO_2{\cdot}xH_2O$" and the DFT-derived structure of β-$TcO_2{\cdot}H_2O$ forming zigzag chains (Oliveira et al., 2022). Here, Tc is six-fold coordinated by oxygen groups, with four shorter Tc-O distances corresponding to coordinated oxygen and two longer corresponding to coordinated water groups. A short Tc-Tc distance at 2.53 Å represents the nearest cation centres of the edge-sharing distorted octahedra along the chains.

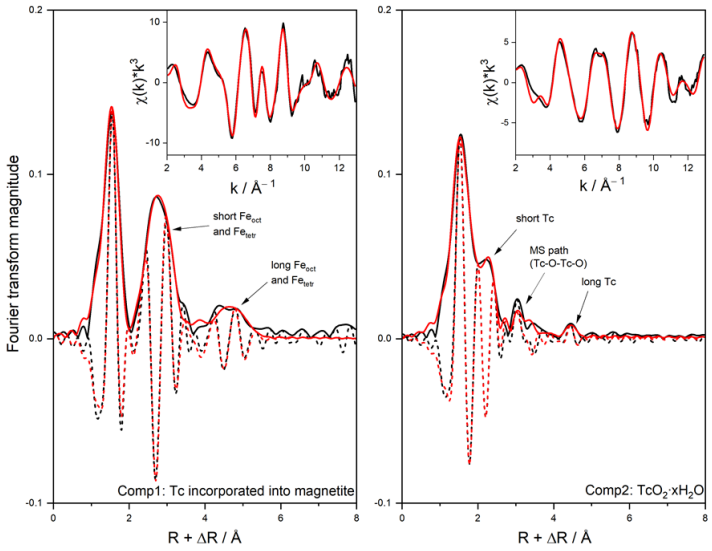

Figure 65: ITFA derived single component spectra (black lines) of the endmembers and their reproduction by shell fitting (red lines). Dashed lines represent the imaginary part. Inserts show the corresponding k^3 weighted EXAFS χ(k) spectra. Component 1 corresponds to the structurally incorporated Tc in magnetite, while component 2 represents $TcO_2 \cdot xH_2O$.

In contrast to the "fresh $TcO_2 \cdot xH_2O$"sample analysed by (Oliveira et al., 2022), where no Tc-Tc backscattering paths beyond the one at 2.5 Å could be fitted, we find here another Tc-Tc path with a distance of 4.76 Å. This distance (only 3 % longer than the one determined by DFT and the aged sample) provides an excellent confirmation for the formation of the β-$TcO_2 \cdot 2H_2O$ zigzag structure, since linear chains would have approximately twice the distance of the first Tc-Tc interaction, i.e., distances beyond 5 Å. There are no additional distances visible, which would indicate a starting polymerization into a 3D network (Oliveira et al., 2022).

Table 23: Shell fit parameters for the two ITFA-derived Tc(IV) endmembers

Component 1: Tc structurally incorporated in magnetite					**S_0^2=0.9**	**E_0=3.7 eV**
Shell	Tc-O	Tc-Fe_{oct}	Tc-Fe_{tetr}	Tc-O	Tc-Fe_{oct}	Tc-Fe_{tetr}
CN	6*	6*	6*	24*	12*	8*
R / Å	2.02	3.09	3.49	4.75	5.19	5.61
σ / Å²	0.0042	0.0101	0.0097	0.0150	0.0135	0.0147
Magnetite (pXRD)	2.06	2.97	3.48	4.71	5.14	5.45
M1 (DFT)	2.05	3.05	3.49	4.73	5.16	5.50
M2 (DFT)	2.06	3.06	3.55	4.80	5.24	5.57
M3 (DFT)	2.03	3.06	3.48	4.72	5.14	5.50

Component 2: TcO_2xH_2O				**S_0^2=0.9**	**E_0=-2.8 eV**
Shell	Tc-O	Tc-O	Tc-Tc	Tc-Tc	MS(Tc-O-Tc-O)
CN	4*	2*	2*	2*	8*
R / Å	1.99	2.43	2.53	4.76	3.99
σ / Å²	0.0022	0.0054	0.0025	0.0116	0.0011
β-$TcO_2 \cdot 2H_2O$ (Oliveira et al., 2022)	1.98	2.23	2.53	4.60	3.96
$TcO_2 \cdot xH_2O$ fresh (Oliveira et al., 2022)	2.01	2.39	2.55	---	4.02

The spectrum of the second component (Comp1) is shown on the left side of Figure 65. Th spectral features as well as the distances determined by shell fitting correspond to Tc residing in an octahedral Fe site of magnetite. This is demonstrated by the six-fold coordination and the distance of 2.02 Å (2.06 Å for the Fe site in magnetite). The distance to the nearest Fe_{oct} shell is with 3.09 Å slightly larger than in magnetite (2.97 Å), indicative of local distortions, most likely due to the required charge compensation mechanism by replacing Fe(II) or Fe(III) by Tc(IV) (see below), while the next-nearest Tc-Fe distance to tetrahedrally coordinated Fe at 3.49 Å is not affected. These observations are in agreement with previous studies (Kobayashi et al., 2013; Yalçıntaş et al., 2016). For the first time we have been able here to also fit three additional shells, constituting the longer-range order of magnetite up to 5.6 Å (Table 23). A stable fit was obtained by fixing the coordination numbers of these paths to their crystallographic values, indicating that Tc is structurally incorporated to a depth of at least 5.6 Å from the magnetite surface, and this not only for the coprecipitation, but also for the sorption samples.

After having determined the structural identity of the two Tc species, we determined their fractions in the sorption and coprecipitation samples by using the ITT procedure of ITFA (Table 24). Note that the fractions are not normalized to unity. At pH 10 and independent of reaction time, Tc^{IV} for Fe substitution in magnetite is the prevalent reaction mechanism. In contrast at pH 5, there is a significant amount of β-$TcO_2 \cdot 2H_2O$ in addition to the substitution species, which decreases with time. Therefore, at this low pH, β-$TcO_2 \cdot 2H_2O$ seems to precipitate first, which then converts into the magnetite substitution species with time. The situation at pH 7 is somewhat intermediate insofar as the amount of the substitution species is higher for the shortest reaction time of 1 d, while it reaches the same amount after the longest time of 49 d.

Table 24: Experimental details from the Tc batch experiments of the kinetic series. pH_{ini} and pH_{end} are the initial and final pH values respectively, after given equilibration time (t_{eq}). [Fe] was measured according to the ferrozine essay (see section liquid analysis) in combination with ICP-MS. Component contributions of extracted EXAFS components (Comp 1 and Comp 2) were determined by ITFA-analysis pf the Tc-K edge EXAFS spectra.

No.	Sample (pH_{ini}, t_{eq})	pH_{end}	Eh (mV)	t_{eq} (days)	$[Fe^{2+}]_{aq}$ (mM)	$[Fe_{tot}]_{aq}$ (mM)	%Comp 1 (Magn.)	%Comp2 (β-$TcO_2 2H_2O$)
1	$TcO_2 \cdot xH_2O$ fresh						0*	100*
2	pH 5, 1 d	5.6	112	1	0.35	0.35	32	80
3	pH 5, 14 d	5.4	98	14	2.15	2.15	58	51
4	pH 5, 28 d	5.2	103	28	1.85	2.26	53	57
5	pH 5, 49 d	5.3	95	49	3.59	4.98	78	34
6	pH 7, 1 d	6.9	-128	1	0.04	0.04	68	43
7	pH 7, 14 d	6.9	-83	14	0.01	0.01	69	40
8	pH 7, 28 d	6.6	-71	28	0.14	0.14	73	38
9	pH 7, 49 d	6.7	-141	49	0.44	0.44	75	35
10	pH 10, 1 d	9.8	-348	1	b.d.l.	b.d.l.	100	15
11	pH 10, 14 d	10.0	-273	14	b.d.l.	b.d.l.	100	0
12	pH 10, 28 d	10.0	-225	28	b.d.l.	b.d.l.	100	0
13	pH 10, 49 d	10.0	-391	49	b.d.l.	b.d.l.	100	0
14	CoPrec 600 ppm Tc	8.7	-357	7	b.d.l.	b.d.l.	100*	0*
15	CoPrec 3000 ppm Tc	9.2	-351	7	b.d.l.	b.d.l.	83	0
16	CoPrec 10000 ppm Tc	9.7	-338	7	b.d.l.	b.d.l.	69	17

b.d.l. - below detection limit

To further investigate possible structures of Tc^{IV} incorporated into magnetite and especially the associated charge compensation mechanism required for replacing Fe with a formal oxidation state of 2.5 with Tc with oxidation state of 4, we conducted atomistic simulations using the PBE functional implemented in AMS/BAND 2022, with full optimization of atomic coordinates and lattice parameters. For the finite structures, solvent effects were included with COSMO. We tested the three charge-

compensation mechanisms postulated by (Smith et al., 2016), which are referred here as M1, M2, and M3:

$$[Fe^{II}_3Fe^{III}_3](Fe^{III}_3)O_{12} + Tc^{IV} + Fe^{2+} \rightarrow [Tc^{IV}Fe^{II}_4Fe^{III}](Fe^{III}_3)O_{12} + 2Fe^{3+} \quad \text{M1}$$

$$3[Fe^{II}_3Fe^{III}_3](Fe^{III}_3)O_{12} + 3Tc^{IV} \rightarrow 3\left[Tc^{IV}\square_{1/3}Fe^{II}_3Fe^{III}_{5/3}\right](Fe^{III}_3)O_{12} + 4Fe^{3+} \quad \text{M2}$$

$$[Fe^{II}_3Fe^{III}_3](Fe^{III}_3)O_{12} + Tc^{IV} \rightarrow [Tc^{IV}\square Fe^{II}Fe^{III}_3](Fe^{III}_3)O_{12} + 2Fe^{2+} \quad \text{M3}$$

In M1, a Tc^{IV} atom and an Fe^{II} atom substitute two Fe^{III} atoms, nominally Tc^{IV} replacing Fe^{III} with another Fe^{III} being reduced to Fe^{II}. In M2, three Tc^{IV} atoms substitute four Fe^{III} atoms, creating a vacancy. Finally, in M3, a Tc^{IV} atom substitutes for two Fe^{II} atoms, creating a vacancy. It should be noted that only the Tc^{IV} incorporation is included in these mechanisms, not the reduction process of $Tc^{VII}O_4^-$.

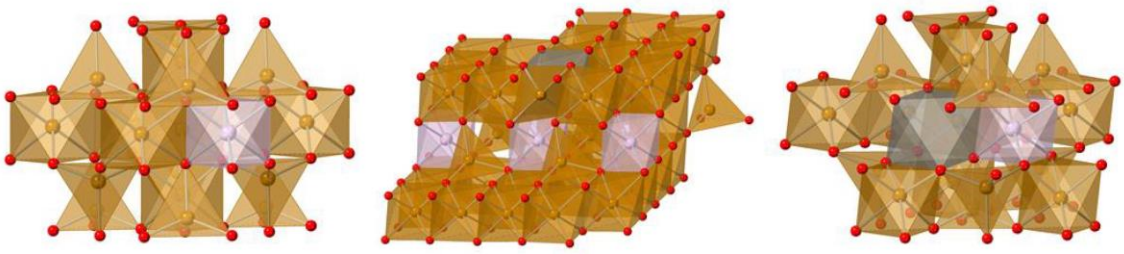

Figure 66. Tc(IV) substitution in magnetite corresponding to mechanisms M1 (left), M2 (center), and M3 (right). Shown structures have been refined by DFT.

The fully DFT-optimized structures are shown in Figure 66, their interatomic distances are shown in Table 24, along with the distances obtained from the EXAFS shell. The calculated incorporation energies and comparison of the Tc coordination structure with experimental EXAFS data indicate that Tc incorporation is most likely to occur either by substitution of two octahedral Fe^{III} sites with a Tc^{IV}/Fe^{II} pair (Figure 66 left, M1), or by substitution of two Fe^{II} sites with a single Tc^{IV}, thus forming a vacancy (Figure 66, right, M3). Mechanism M2, where three Tc^{IV} replace four octahedral Fe^{III} (centre), could be excluded.

3.2.3.5 Conclusions

Based on these results we can now try to answer our starting questions, namely (1) what is the exact structure of the TcO_2 xH_2O precipitate, (2) is TcO_2 xH_2O, or small dimeric or trimeric clusters of it, attaching to magnetite by forming chemical bond(s) with the surface? (3) How can a sorbate (Tc) be so rapidly (within days) incorporated by a rather insoluble sorbent (magnetite) and what is controlling the extent of the competing reaction, namely the precipitation of TcO_2 xH_2O?

(1) What is the exact structure of the $TcO_2 \cdot xH_2O$ precipitate?

Our DFT calculations demonstrate that the $TcO_2 \cdot xH_2O$ structure does not consist of linear chains as suggested by (Lukens et al., 2002), but rather of zigzag chains based on the structural motif of β-TcO_2. While the fresh precipitate can be best described as β-$TcO_2 \cdot 2H_2O$ chains as confirmed by both the DFT calculations as well as the experimental EXAFS structure Figure 57, Figure 65, Table 21, Table 23), the chains seem to polymerize with time by condensation (water loss) into a 3d network (Oliveira et al., 2022).

(2) Is $TcO_2 \cdot xH_2O$, or small dimeric or trimeric clusters of it, attaching to magnetite by forming chemical bond(s) with the surface?

DFT calculations demonstrate that β-TcO_2 $2H_2O$ chains may sorb to the magnetite(001) surface. A comparison with our experimental EXAFS data confirms, however, that this (001) surface does not seem to prevail for environmental magnetite nanoparticles. Furthermore, our extensive EXAFS study in the

Tc/magnetite system shows that only two species occur, i.e. independent β-$TcO_2 \cdot 2H_2O$ chains and Tc incorporated by magnetite, but not the previously identified dimeric or trimeric chains sorbed to the magnetite surface (Yalçıntaş et al., 2016). This latter (miss-)conclusion may have resulted from an incomplete separation of the spectra of β-$TcO_2 \cdot 2H_2O$ chains and that of Tc incorporated by magnetite.

(3) How can a sorbate (Tc) be so rapidly (within days) incorporated by a rather insoluble sorbent (magnetite) and what is controlling the extent of the competing reaction, namely the precipitation of $TcO_2 \cdot xH_2O$?

In terms of the Tc incorporation, which we could demonstrate to be not only a surface-near process, but to proceed to greater distances (> 5.6 Å from the surface as indicated by fully coordinated paths at this length), we need to exclude lattice diffusion, since this process would be extremely slow even at temperatures above 1000°C (Van Orman and Crispin, 2010). We therefore discard such a process, even though redox reactions and cation vacancies frequently observed in nanoparticles might somewhat accelerate this process, but certainly not to the extent that full incorporation at RT and within one day might be possible through lattice diffusion (Roshchin and Roshchin, 2019).

According to our previous hypothesis (Yalçıntaş et al., 2016), incorporation might happen through a dissolution/reprecipitation process at the magnetite surface, driven by a higher magnetite solubility at lower pH. We now need to discard this hypothesis, since we observe that incorporation is highest at pH 10, and lowest at pH 5, where magnetite solubility should be highest.

Incorporation might also happen through dissolution/reprecipitation driven by redox processes, where magnetite would act as a battery (conveyor belt model of Scherer, e.g., (Handler et al., 2009; Williams and Scherer, 2004)). They observed that Fe^{2+} reacted Fe oxides sorbed and oxidized this Fe^{2+}, thereby neoforming/ extending the Fe oxide at the site of the original Fe^{2+} sorption, while another Fe^{2+} is formed from structural Fe(III) at a different site, and subsequently released into solution. This way, they observed a rather fast incorporation of ^{57}Fe, with which they had spiked the solution. This mechanism would in fact be in line with a fast, redox-driven incorporation of Tc into magnetite, which would be favoured by sorbed Fe^{2+}, i.e., a higher pH.

At low pH, we observe a substantial release of Fe^{2+} from magnetite (3-6 times higher than release of Fe^{3+}, see Figure 62), a process previously described as maghemitization of the magnetite surface, i.e. leaving behind a fully oxidized surface with vacancies). While magnetite has a rather low bandgap (0.5 eV), it easily acts as battery, providing electrons from deep inside the structure, in line with fast incorporation at higher pH. This process is, however, blocked through the maghemitization of the surfaces. Therefore, only Fe^{2+} re-adsorbed at the surface can reduce pertechnetate (or less likely aqueous Fe^{2+} in a homogenous redox reaction, which is a much slower process), and since incorporation is less likely because of the lacking conveyor belt/battery effect, reduced Tc(IV) precipitates at least partially as β-$TcO_2 \cdot 2H_2O$.

3.2.4 Re interaction with iron oxides, and implications for Tc/Re analogy [ISTErre]

Re(VII) occurs in oxic solution as monovalent anionic species ReO_4^-(aq) and in suboxic waters as the $ReO(OH)_2^0$(aq) neutral aqueous species and $ReO(OH)_3^-$ species (Figure 67). These Re(VII) and Re(IV) species would be expected to be poorly electrostatically adsorbed on iron oxides above their point of zero charge (PZC), i.e., on a negatively charged surface.

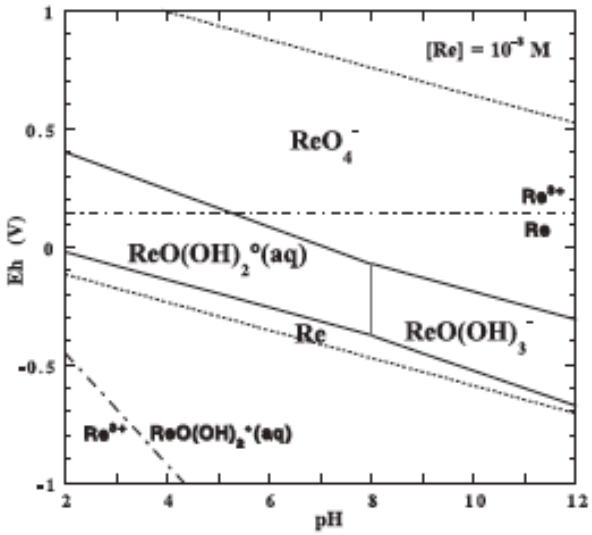

Figure 67. Eh-pH redox diagram for Re in aqueous system (Kim and Boulègue, 2003).

3.2.4.1 Single ion adsorption experiments

Single ion adsorption experiments were conducted with 10 g/L of magnetite and an initial aqueous concentration of 160 ppm Re, enough to cover the surface sites of magnetite. Macroscopic results (Table 25) show:

- No adsorption below pH 7 (No adsorption on magnetite at pH 5, where half magnetite is transformed to maghemite, Figure 1; very limited adsorption at pH 7)
- Maximum adsorption (about 5000 ppm Re in solid) at pH 7 and 8
- Limited adsorption above pH 8

Table 25. Single ion perrhenate sorption experiment on magnetite (10 g/L of magnetite and an initial aqueous concentration of 160 ppm Re): macroscopic results.

pH initial	Fe initial (ppm)	Fe after Re sorption (ppm)	Fe removed (ppm)	Re initial (ppm)	Re final in solution	Re removed from the solution (ppm)	Calculated uptake based on solution difference (mg/kg)	Re on solid after dilution 1 g/L	Calculated Re uptake based on solid dissolution (mg/kg)
10	0.002	0.049	-0.046	160	145.04	14.96	1496.3	3.024	3024.4
9	0.031	0.018	0.013	160	128.57	31.43	3143.4	4.258	4258.2
8	0.94	0.246	0.695	160	113.94	46.06	4606	5.746	5746.2
7	3.74	1.284	2.456	160	113.49	46.5	4650.4	7.633	7633.1
6	138.39	162.671	-24.277	160	165.52			0.915	914.6
5	1344.7	1117.06	227.641	160	165.83			0.288	288.2
4	1412	1209.74	202.26	160	167.12			0.278	278.2
3	1977.74	1772.35	205.386	160	173.23			0.312	311.8

Another experiment conducted at higher total Re concentration (3.2 mM, i.e. in excess to the 0.72 mM surface site concentration in a 2g/L solid concentration suspension), showed only 2% and 5% of Re(VII) adsorbed at pH 5 and pH 7, respectively.

As in our case the total concentration was several times higher than in Yalçintas series, an additional experiment with the analogous loadings (400-900 ppm) and pH conditions was prepared (data not shown here). Once again, the Re(VII) sorption was negligible ($c_0 \approx c_e$ within ICP-AES error) and the corresponding XANES analysis did not reveal Re(IV) presence, but only hardly detectable not reduced Re(VII).

3.2.4.2 Competitive adsorption experiments

Re(VII), a non-radioactive chemical analogue of Tc(VII) (Kim and Boulègue, 2003) was introduced in the two Se(VI) sorption experiments (pH 5 and pH 7) in its soluble form ($Re(VII)O_4^-$), to test a possible sorption competition with Se(VI) (Table 26). Motivation for this experiment were adsorption studies of Tc on magnetite (Yalçıntaş et al., 2016), which showed that complete reduction of Tc(VII) to Tc(IV) took place on the iron oxide, and that loading (400-900 ppm) and pH influenced the incorporation mechanism due to magnetite solubility and recrystallization process.

Table 26. Experimental conditions for Re batch sorption experiments on nanomagnerite.

	Magnetite conc. [g/L]	pH	Initial RN conc. (M)	Initial Se(VI) conc. [mg/L]	Initial Re(VII) conc.[mg/L]	Max possible loading [µM/m^2]
Se(VI)/Re(VII)	10	5	8.6E-03	340	800	13.23
Se(VI)/Re(VII)	10	7	8.6E-03	340	800	13.23

* average magnetite surface area from BET = 65 g/m^2

In our competitive Se(VI)/Re(VII) studies, rhenium concentration (Figure 68) in solution remained remarkably stable at both tested pH during 5 months of the reaction. Only very little sorption was observed during the first day: 0.16 molecule/nm^2 at pH 5 and 0.38 molecule/nm^2 at pH 7, but the final values stabilized at around 0.05 molecule/nm^2 (pH 5) and 0.1 molecule/nm^2 (pH 7).

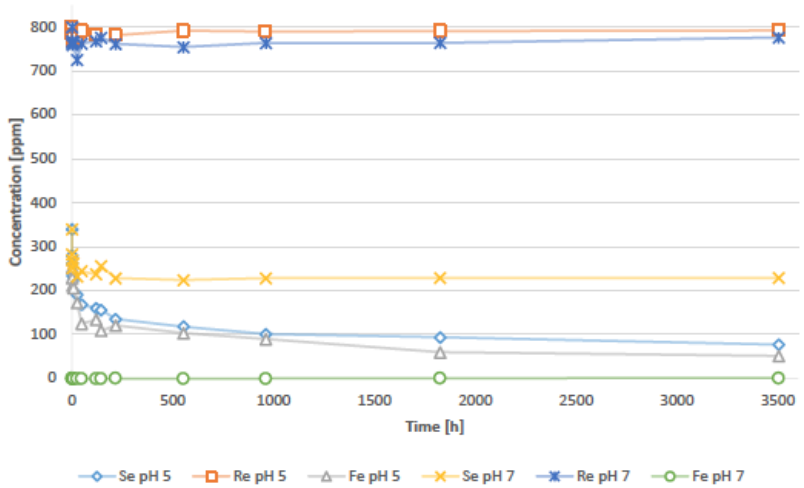

Figure 68. Se, Re and Fe aqueous concentrations in competitive Se(VI)+Re(VII) sorption on magnetite experiments. Blue diamonds: Se at pH 5; red squares: Re at pH 5; grey triangles: Fe at pH 5; yellow x: Se at pH 7; blue crossed x: Fe at pH 7; green circles: Fe at pH 7.

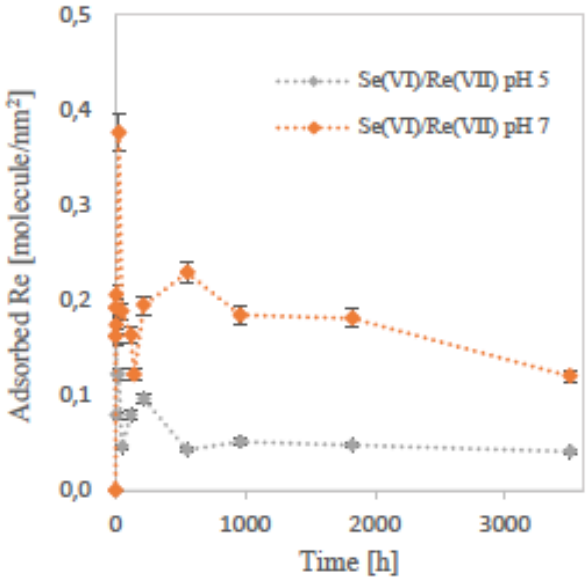

Figure 69. Sorption kinetics of Re(VII) observed in the combined Se(VI)/Re(VII) sorption experiment.

The small adsorption observed in Figure 68 may be attributed to the $ReO(OH)_2^0(aq)$ neutral aqueous species formation (Figure 67), which is not attracted by mineral surfaces. In presence of divalent selenate ions, i.e., in competitive Se(VI)+Re(VII) experiments, the Se(VI) adsorption and reductive precipitation by Fe^{2+} as Se(0) nanowire outcompetes Re(VII) monovalent oxyanion for adsorption onto nanomagnetite.

The obtained results agree rather with Heald et al. (2012) who studied perrhenate (Re(VII)) and pertechnetate (Tc(VII)) uptake on corroded steel coupons. The authors showed that different mechanism-controlled oxyanions sorption: while most of the Tc(VII) was reduced to Tc(IV) and strongly bounded to the corrosion products, only 5-10 % of Re(VII) got reduced to Re(IV) and the reduced form was easily detachable from corrosion product by the X-ray beam.

In principle, the negatively charged monovalent $Re(VII)O_4^-$ oxyanion could have been weakly electrostatically attracted on the neutral or slightly positively charged iron oxide surface, competing with the divalent Se(VI). However, only little sorption was detected in the absence of competitor in the additional experimental series (pH range 3-10, data not shown here), with the highest sorption at pH 7-8, similar to Re(VII) - Zero Valent Iron (ZVI) system studies (Lenell and Arai, 2017). Another possibility could be formation of insoluble neutral species like $Re(IV)O(OH)^0_{aq}$ (Kim and Boulègue, 2003) , which indeed were not attracted on the surface of the positively charged mineral, but the Mössbauer spectroscopy results did not show increase in maghemite to magnetite ratio, so there was no electron transfer between iron oxide and dissolved Re(VII).

Due to negligible Re(VII) uptake on magnetite and not detectable reduction in solution, we consider that the Se(VI) adsorption kinetics dominates the two mixed batch sorption experiments, and the further consideration will focus only on selenite oxyanion. Additional ongoing studies with Re(VII) will be published elsewhere.

In the combined Se(VI)/Re(VII) series at pH 7, 5-11 % of magnetite to maghemite conversion was reached at 6 hours, based on 300 K data Mössbauer modelling, but 0 % according to Mössbauer spectra recorded at 77 K. It this case at 1% of mineral oxidation corresponds to max 7.1 ppm Se removal (at 6 h, taking 11 % conversion rate) and further conversion until 76 days gives roughly 1% of mineral oxidation for each 1 ppm of Se removal.

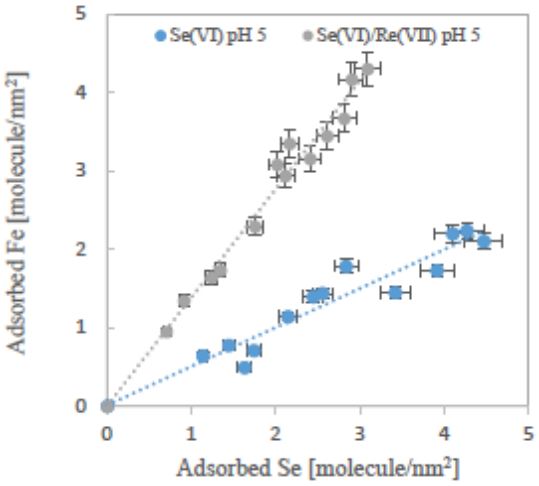

Figure 70. Linear dependence between Se(VI) and Fe(II) sorption found in experiments at pH 5. As the Fe(II) first measurement was done at 10 min, concentration at time 0 was estimated by interpolation of the linear fitting. Error bars represent 5 % error of the ICP-AES measurements.

A large difference in aquatic Fe concentration is observed after 10 minute equilibration (104 ppm Fe for the Se(VI) alone experiment vs. 253 ppm Fe for the combined Se(VI)/Re(VII) experiment) (Figure 70) and faster consumption at higher selenium solid content confirmed the thesis of a rapid interaction between selenate ions during/before Se(0) nanowire crystallization process.

XANES data showed no reduction of Re(VII) in any experiment (Re(VII) alone or combined Se(VI)/Re(VII) experiment.

3.2.4.3 Revisited “analogy Re-Tc”

Little Re(VII) monovalent oxyanion adsorption occurs at low pH, when the surface should be positively charged. Adsorption on magnetite occurs only in alkaline conditions (pH 7-10), as reported for perrhenate sorption on zero-valent iron (ZVI) where the highest adsorption was observed at neutral pH and was lower in acidic and basic conditions (Lenell and Arai, 2017). This contrast with Tc adsorption levels (near 100% adsorption, at much lower total concentration; (Yalçıntaş et al., 2016)). This may question the Tc/Re analogy, though additional sorption experiments should be conducted at Re concentrations equal to that used with Tc by Yalçıntaş et al. (2016).

3.2.5 Summary concerning Tc/Re reactivity

This section aimed at investigating Tc/Re reactivity towards Fe-containing solids. In the case of phyllosilicates, Tc(VIII) retention is low when pristine nontronite samples, containing mainly Fe(III), is used as an adsorbent and, in this case, nontronite reactivity is outcompeted by Fe(0) in mineral mixtures. When Fe(II) is increasingly introduced in nontronite structure by submitting the pristine nontronite to chemical reduction procedures of increasing strength, Tc(VII) is increasingly sorbed, suggesting interation of Tc(VII) of Fe(II). This is supported by the observation that Tc(VII) is reduced to Tc(IV), as $TcO_2.nH_2O$. This compound was investigated by DFT, and significant insights could be gained regarding its mineralogy. In particular, a typical “zig-zag” structure could be proposed. When Tc(VIII) is interacted with magnetite, a significant pH effect is observed, with Fe(II) being preferentially released to the solution upon contact with Tc(VII), possibly due to maghemitization of the surface. This Fe(II) then has redox interaction with Tc(VII), certainly at the mineral surface, to produce β-$Tc(IV)O_2{\cdot}2H_2O$. In the case of Re, a pH effect could also be evidence, and sorption kinetics could be investigated. However, some differences between Tc and Re behaviours at magnetite surface could be evidenced, and it then recommended to perform additional studies before the Tc/Re analogy can be validated.

3.3 Np reactivity towards phyllosillicates [KIT]

This study combines different experimental approaches to study the role of Fe in the illite structure on the Np retention in sorption and diffusion experiments performed in an anaerobic or aerobic environment. Fe K-edge XANES spectroscopy, ^{57}Fe Mössbauer spectroscopy, transmission electron microscopy (TEM), and fluorescence microscopy were applied for comprehensive characterization of Fe in IdP. Batch sorption data of Np on clay minerals with different Fe content were compared. Electronic structure, bonding properties, and local atomic environment of selected IdP samples were probed using Np M_5-edge HR-XANES and L_3-edge EXAFS spectroscopy. Complementary to the spectroscopic studies, solvent extraction (Bertrand and Choppin, 1982) was carried out to determine fractions of Np(IV) and Np(V) sorbed on IdP as a function of pH and contact time (t_c). Similarly, Np was characterized in IdP segments as a function of diffusion depth after a 3-year diffusion experiment. The results and experimental details can be found in (Schacherl et al., 2023; Schacherl et al., 2022a).

The comparison of the Fe K-edge XANES spectra inflection points of nontronite (Fe(III)-rich smectite) and olivine (Fe(II) neosilicate) with IdP A (Figure 71A) showed that Fe is predominantly present as Fe(III) with a minor fraction of Fe(II) in IdP A. Fe K-edge EXAFS spectroscopy (Figure 71B**,** Schacherl et al. (2023)) allocated Fe as predominantly present in the octahedral sheets of IdP A. Both, EXAFS and TEM-energy-dispersive X-ray spectroscopy (EDX) (Figure 71B and Schacherl et al. (2023) Figure SI 6) identified a homogenous distribution of Fe across the clay sample and the absence of Fe oxide nanoparticles. Furthermore, crystallites of a Ca-phase were found in IdP A by TEM and EELS. Bradbury and Baeyens (2009a) removed the Ca-silicate phase in their illite purification procedure, applied in the present study to purify IdP B. To examine if this phase influences Np sorption, illite batches with (IdP A) and without (IdP B) this phase was investigated in Np batch sorption experiments in this study. ^{57}Fe Mössbauer spectroscopy (Schacherl et al., 2023) found approximately (34.0 ± 0.5) at.% Fe(III) in octahedral sheets, (58.0 ± 0.5) at.% Fe(III) in tetrahedral sheets, (6.0 ± 0.5) at.% Fe(II) in octahedral sheets, and (2.0 ± 0.5) at.% Fe(II) in tetrahedral sheets of IdP A. The exact quantification of the actual redox-active Fe is not trivial (Gorski et al., 2012a; Huang et al., 2021), however, the fact that Fe(II) exists in IdP in a low percentage is of relevance for the present study. Fluorescence microscopy with live-death staining (Schacherl et al., 2023) confirmed no living or dead organic matter in the clay. The results of all the various analysis methods combined excluded the presence of microorganisms and Fe oxide nanoparticles in the IdP A batch and hence, confirmed that the only redox couple present in IdP A is structural Fe(II)/Fe(III). The presence of structural Fe(II) in the IdP despite purification under aerobic conditions is surprising and needs further investigation.

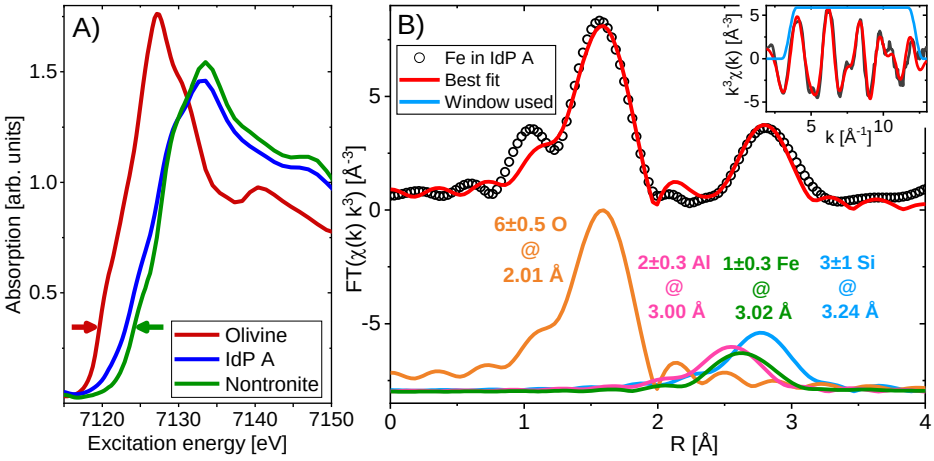

Figure 71**:** A) Fe K-edge XANES spectra of olivine (red), IdP A (blue), and nontronite (green). The first inflection point of nontronite and olivine are marked with an arrow. B) EXAFS spectrum in *R*-space of Fe in IdP A (black circles) and the best fit (red line). The contributions of each path are shown vertically shifted. The k^3-weighted $\chi(k)$ (black line), the used window (blue line), and the best fit (red line) are in the embedded figure (top right) (Schacherl et al., 2023).

3.3.1 Sorption and solvent extraction results

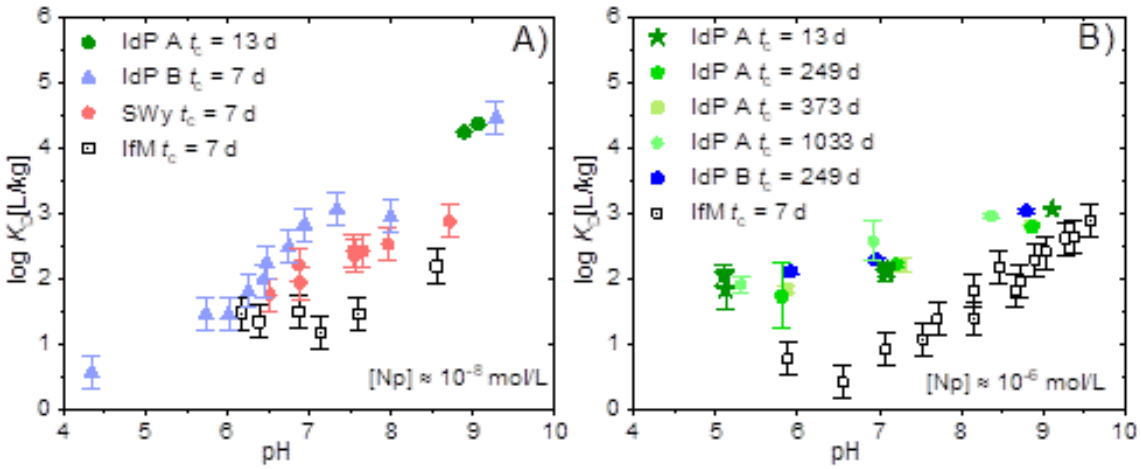

Figure 72. Distribution coefficients (log K_D) of Np(V) on clay minerals A) as a function of pH at c_0(Np(V)) = 1×10^{-8} mol/L; B) log K_D of Np(V) as a function of pH and contact time (t_c) at c_0(Np(V)) = 1×10^{-6} mol/L; Illite du Puy (IdP A – green signs, IdP B – blue signs) (Asaad et al., 2022), Wyoming smectite (SWy – red circles) {, #238}, Fe-free montmorillonite (IfM – empty black squares) (Reinholdt et al., 2001). The error bars refer to ±0.25 log K_D units on the single sorption experiments and to 95 % confidence interval of the quadruplicate sorption experiments (Schacherl et al., 2023).

3.3.1.1 Sorption of Np on IdP A, IdP B, SWy, and IfM.

Np(V) sorption was studied for three different clay minerals (Figure 72**,** Schacherl et al. (2023)). Although the structural Fe in IdP A was thoroughly characterized and the presence of Fe oxide nanoparticles and microorganisms excluded, in the case of IdP B, SWy, and IfM, no such detailed characterization was performed. However, the materials were characterized previously (Baeyens and Bradbury, 1997; Bradbury and Baeyens, 2009b; Soltermann et al., 2013). Consequently, the presence of Fe oxide nanoparticles in the clay suspensions can be excluded for all clays studied. In comparison to SWy, IdP A, and IdP B, Np(V) exhibited the lowest log K_D onto IfM above pH 7 (Figure 72A and B). A slightly increased log K_D was noticeable for Np(V) sorbed on SWy. The highest log $K_D$was found for Np(V) onto IdP A and IdP B. The latter minerals contain about 3.7 wt.% Fe_2O_3 (SWy) and 6.94 wt.%Fe_2O_3 (IdP A/B), respectively.

In literature, differing sorption affinities are sometimes related to differing surface areas of the studied sorbent (Payne et al., 2011). However, in this study, the N_2-BET surface areas of IdP B (97 m^2/g) (Bradbury and Baeyens, 2009b), SWy (35 m^2/g) (Baeyens and Bradbury, 1997), and IfM (123 m^2/g) (Soltermann et al., 2013) could not account for the differences in sorption. The total amount of sorbed Np increased in all cases with increasing pH due to increasing clay edge site deprotonation (Soltermann et al., 2013). The contact time beyond 13 days did not seem to influence the total amount of sorbed Np on IdP (Figure 72B). This is in accordance with the findings of Marsac et al. (2015). The comparison of the sorption data of illite treated with different purification procedures, namely IdP A and IdP B (Figure 72), did also not show a significant difference in the overall Np sorption. Since there is no difference between IdP A and B, the Ca-phase crystallites detected in IdP A by TEM (Schacherl et al. (2023)) probably did not play a major role in the sorption of Np. K_D values for both initial Np concentrations (c_0(Np(V)) = 1×10^{-8} mol/L and 1×10^{-6} mol/L) are congruent to those found by Marsac et al. (2015). Note, the lower log(K_D) values for the IdP samples at higher Np(V) concentrations cannot be attributed to a strong/weak site complexation effect, because the Np loading at 1×10^{-6} mol/L Np is still significantly below the available amount of strong sites at pH 7 and 9 (2×10^{-6} mol/g × 2 g/L = 4×10^{-6} mol/L) (Bradbury and Baeyens, 2005). Consequently, the strong sites should not be saturated with Np in this pH range. Np(V) sorption onto IdP under aerobic conditions and published by Bradbury and Baeyens (2009b) showed a similarly low sorption as obtained in this study for IfM. Marsac et al. (2015) explained the differences in Np(V) sorption on IdP performed in their experiments under anaerobic conditions and

those of Bradbury and Baeyens (2009b) conducted under aerobic conditions by a surface-induced reduction of Np(V) to Np(IV). Since Np(IV) exhibits stronger sorption onto surfaces than Np(V), this indicates that more Np(IV) is formed under anaerobic conditions. A higher Np(IV) ratio at lower total Np loading also explains the increased log K_D at a low initial Np concentration.

3.3.1.2 Solvent extraction of Np sorbed on IdP A.

In order to verify the assumption of Np(V) reduction at IdP surfaces, solvent extraction experiments were carried out with Np batch sorption samples of contact times up to t_c = 1033 d (Schacherl et al., 2023). The amount of Np left on the clay after solvent extraction was determined by total acid digestion of some samples, since mass balance calculations revealed that a certain fraction of Np did not desorb. Surface-sorbed Np(V) should be very easily desorbable. The strong binding of Np to clay even under acidic conditions is, thus, explained by reduction of Np(V) to strongly binding Np(IV) species. In Table 27,this fraction is assigned as “Np(IV) clay digestion” and added to the Np(IV) fraction determined by solvent extraction (before digestion “Np(IV) desorbed”; after digestion “total Np(IV) on illite” Table 27). Even then, mass balance calculations revealed that a part of Np (≈ 6 to 18 % of the initially added Np in the majority of samples) could not be recovered. Consequently, the Np(IV) fraction in Table 27 can be considered as lower limit. The non-retrievable fraction could be Np lost by wall sorption during the various processing steps.

The fraction of total Np(IV) on illite detectable by solvent extraction and clay digestion increased with decreasing pH. The fraction of total Np(IV) was very small at pH 9 – between 2 and 10 %. At these low amounts, the uncertainties become significant. At pH 7, the relative amount of Np(IV) ranged from 6 to 15 % (Table 21). At pH 5, the corresponding digestion and solvent extraction yielded a Np(IV) fraction of 11 to 24 %.

Table 27: Sorption, extraction, and digestion results for single samples in ppm = µg(Np)/g(clay). The total Np(IV) on illite is calculated as (Np(IV) desorbed + Np(IV) clay digestion)/(Np(IV) desorbed + Np(IV) clay digestion + Np(V) desorbed). “Np not retrieved” is the difference between Np theoretically sorbed and the amount of Np experimentally desorbed and found after total clay digestion. The errors represent propagated systematic errors including the extraction error (2 % (Bertrand and Choppin, 1982)), pH error: ±0.05 (Schacherl et al., 2023).

illite	t_c / d	pH	Np sorbed / ppm	solvent extraction		Np(IV) clay digestion / ppm	total Np(IV) on illite / %	Np not retrieved in % of total Np
				Np(V) desorbed / ppm	Np(IV) desorbed / ppm			
IdP-A	13	5.1	31±4	1.33±0.03	0.13±0.03	0.04±0.01	11±2	18±2
IdP-A	249	5.81	12±4	2.39±0.07	0.64±0.05	0.123±0.001	24±2	6±3
IdP-A	1033	5.41	20±3	2.37±0.08	0.31±0.06	0.245±0.005	19±2	11±2
IdP-B	249	5.87	29±4	2.62±0.06	0.13±0.06	0.366 ±0.006	16±2	17±2
IdP-A	13	7.08	32±4	16.0±0.4	0.7±0.3	0.360 ±0.007	6±2	9±2
IdP-A	1033	6.95	120±5	16±0.5	2.0±0.4	0.90±0.03	15±2	51±3
IdP-A	13	9.11	116±2	87±2	0.8±1.8	1.40 ±0.03	2±2	16±2
IdP-A	249	8.89	84±3	56±1	2±1	1.67 ±0.03	5±2	17±3
IdP-A	1033	8.33	177±7	165±5	5±3	4.0±0.1	5±2	1±3
IdP-B	249	8.81	102±3	62±2	3±1	3.72 ±0.06	10±2	17±2

To rationalize this observation, one may have another look to (Figure 72B). Sorption data reveal that at near-neutral pH, the extent of Np(V) sorption onto IdP is significantly increased relative to the sorption on IfM. Assuming surface-mediated reduction taking place as proposed in the literature, this is the consequence of the much stronger sorption of Np(IV) than of Np(V) notably at low pH. The difference in distribution coefficient, K_D, values clearly decrease at high pH, indicating that the thermodynamic driving force for Np(V) reduction to Np(IV) is higher at low pH than at high pH. The experimentally observed increase of Np(IV) with decreasing pH is compatible with the variation in sorption and thermodynamic considerations.

In a further test, the Np sorption onto IdP A at aerobic and anaerobic conditions at pH 5 was compared. NpO_2^+(aq) is dominating the solution speciation in both systems. IdP A contains, also under aerobic conditions, structural Fe(II). The average distribution coefficient after t_c = 11 d amounted to log K_D = (1.27 ± 0.19) L/kg under aerobic conditions and log K_D = (1.9 ± 0.1) L/kg under anaerobic conditions. In the aerobic samples, the redox potential, E_h, is controlled by dissolved oxygen, which caused a decreased amount of sorbed Np(IV) resulting in a lower amount of total sorbed Np. E_h values in the anaerobic sorption sample were significantly lower as compared to the aerobic experiment and controlled by the Fe(II)/Fe(III) couple of IdP A. However, E_h measurements in systems with low concentrations of redox pairs are difficult.

While the general trend of experimental redox speciation data is compatible with the assumed surface-mediated reduction concept, the presented results are in some disagreement with respect to the quantity of reduced Np as compared to the data reported by Marsac et al. (2015). They found (41±10) % reduction of sorbed Np to Np(IV) for the extraction of one sample at pH 7, which is higher than the 6–15 % measured in the present study. However, Marsac et al. (2015) proposed for their L_3-edge XANES analysis samples only 14 % Np(IV) contribution at pH 7.4 and 5 % Np(IV) at pH 9.6.[23]

The origin of the analytical deviations for Np(IV) are presently unclear. Differences in the outcome of solvent extraction experiments might be due to different experimental boundary conditions (extracting agents, contact times) or re-oxidation during the extraction. In the case of Np-237 quantification by LSC as described in Marsac et al. (2015), matrix effects may have interfered the α/ß-discrimination, resulting in incomplete separation of the high energetic ß⁻-radiation of Pa-233 from the α-radiation of Np-237. Both artifact types can result in under- and overestimation of Np(IV) fractions, respectively. For this reason, ICP–MS was used as Np-237 detection method in the batch sorption experiments in the present study. In addition, special care was taken to purify the solvents from oxygen impurities before use in the experiments.

3.3.1.3 Solvent extraction of Np in diffusion samples.

A diffusion experiment with compacted IdP A and Np(V) was conducted at pH 5 for 1050 days to study the clay-induced Np(V) reduction at a higher S/L ratio and under dynamic conditions (Van Loon et al., 2003). The Np diffusion profile was determined by acid and solvent extraction for six segments representing diffusion depths ranging from 0.6 mm to 9.6 mm. Np(IV) and Np(V) contents above the detection limit (2 ppm) were detected in every clay segment extracted. The Np(IV) content ranged from (7 ± 2) % to (33 ± 5) % of extracted Np with strong scattering throughout the diffusion sample (Figure 73). Detailed results of this diffusion experiment are reported in (Beck et al., 2020). It is however interesting to note that modelling results of the in- and out-diffusion data during the first 230 days (referred to as Np-2 in (Beck et al., 2020)) resulted in a relatively high log K_D = (1.78 ± 0.04) L/kg, which resembles the K_d value measured in the anaerobic sorption samples (Schacherl et al., 2023). Such a high K_d value is incompatible with sorption of Np(V) to IdP (see discussion above) and can be explained with a much lower oxygen abundance in the pore system as compared to the aerobic conditions in the reservoirs, which results in the partial reduction of the Np(V) on the clay.

The Np(IV) fraction ranging from 7 to 33 % measured in the clay in this study, is lower than 63 % Np(IV) found onto bentonite by Xia et al. (2005). In contrast to the here analysed experiment with a E_h (source reservoir solution) of about 350–500 mV, Xia et al. (2005) added $Na_2S_2O_4$ to the source reservoir solution which lead to an E_h of about -200 to -400 mV. E_h values in the pore volume are difficult to measure, so that further analysis of the diffusion profile by reactive transport modelling could help to clarify the distinct contributions of Np sorption and reduction processes on diffusive transport. Reich et al. (2016) found (80 ± 5)% Np(IV) at 450 µm and (26 ± 5)% at 525 µm diffusion distance by Np L_3-edge XANES spectroscopy for the Np diffusion through Opalinus Clay. They attributed it to the presence of accessory Fe(II)-mineral phases such as pyrite, which were detected but not quantified as a function of depth. Invasive speciation techniques such as extractions, where chemical conditions are significantly varied during the analysis, can be subject to systematic errors to some extent. For this reason, the segments were also analysed spectroscopically.

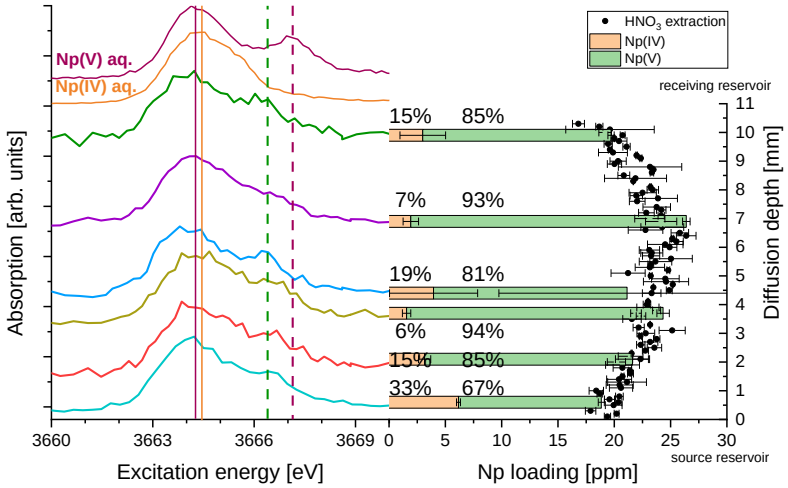

Figure 73. (Left) Vertically shifted Np M_5-edge HR-XANES spectra of selected diffusion segments and aqueous Np(IV) and Np(V) reference solutions. (Right) Amounts of Np(IV) in orange and Np(V) in green found by solvent extraction in the desorbable fraction of Np from the IdP A segments between 0.6 mm and 9.6 mm diffusion depth. Black dots indicate the amount of Np desorbed by oxidative acid extraction (Schacherl et al., 2023).

3.3.2 Spectroscopic findings

3.3.2.1 Np M_5-edge HR-XANES spectroscopy of Np sorbed on IdP A.

The spectra of Np(V) and Np(IV) aqueous reference solutions (*c*(Np) = 20 mmol/L) and of three batch sorption samples (pH 5 and 9) are depicted in Figure 74. The different features are described in detail in Schacherl et al. (2022b). Briefly, the spectrum of $Np(V)_{aq}$ shows a strong peak at 3664.1 eV (*A*) and a distinct shoulder at 3667.14 eV (*B*). Feature *B* can be correlated with the 3d transition to the unoccupied σ* orbital of the axial Np-O bond (Schacherl et al., 2022b; Vitova et al., 2017; Vitova et al., 2020). The spectrum of $Np(IV)_{aq}$ exhibits a relatively broad white line (WL) with its maximum (*A*) trending to slightly higher excitation energies compared to *A* of $Np(V)_{aq}$, but descends quickly hereafter. The spectrum of Np sorbed on IdP A at pH 9 shows a feature *B'* shifted to lower energies compared to feature *B* in the spectrum of $Np(V)_{aq}$, pointing to a decreased bond covalency of Np-O_{ax}. The energy position of the first intense peak *A* is similar for $Np(V)_{aq}$ and Np sorbed onto IdP A. This observation indicates a similar electron density on the central Np atom despite decreased Np-O_{ax} bond covalency. This suggests stronger covalent interaction between the Np(V) sorbed and O_{eq} of the clay binding site compared to $Np(V)_{aq}$. Similar empirical observations have been made for U(V) complexes (compounds 2 and 7) (Vitova et al., 2022). Lower U-O_{ax} bond covalency was found for 2, but the electronic density on U remained similar as result of differences in the U-equatorial ligand interaction. Additionally, the intensity of the shoulder *B'* is decreased in comparison to shoulder *B*, indicating that a fraction of Np(IV) might also be present.

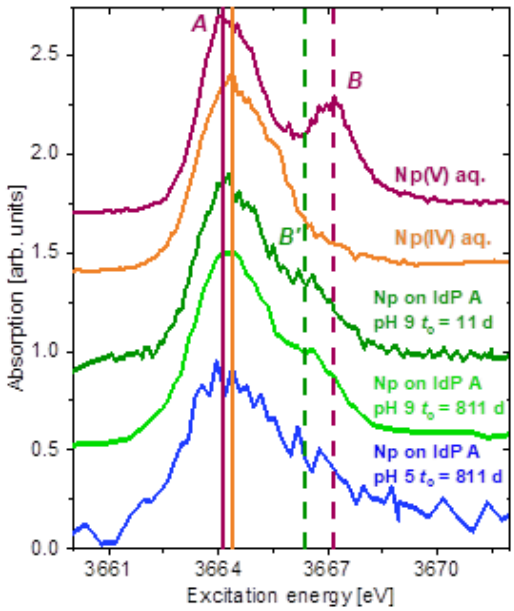

Figure 74. Np M_5-edge HR-XANES spectra of Np(V) and Np(IV) in aqueous solution and Np sorbed on IdP A at pH 9 after 11 and 811 d of contact time as well as Np sorbed on IdP A at pH 5 after 811 d of contact time. For easier comparison, the spectra were vertically shifted (Schacherl et al., 2023).

The sample at pH 9 was studied after t_c = 11 days and after t_c = 811 days. A clear improvement in signal-to-noise ratio despite shorter acquisition time is visible (Figure 74), which was achieved due to improvements in the experimental setup at the beamline (Schacherl et al., 2022a; Schacherl et al., 2022b). Nevertheless, the spectral features remained the same, an indication that no significant changes in the Np(IV)/Np(V) ratio on the IdP A at pH 9 occurred even after longer contact times.

The HR-XANES spectrum of the pH 5 batch sorption sample after 811 d is also displayed in Figure 74. A high noise level is preventing a detailed examination. However, the trend of a broader WL feature *A* and a decreased intensity of feature *B'* than in the pH 9 sample seems to progress, thus resembling slightly more the $Np(IV)_{aq}$ spectrum. This hints at a substantial Np(IV) amount in the batch sorption sample at pH 5. The fraction of 11 to 24 % Np(IV) found by solvent extraction seems to agree with this finding. The lack of appropriate Np reference compounds hindered the quantification of the Np(IV)/(V) ratio from the HR-XANES spectral data. An appropriate Np reference system would consist of an experiment, where redox conditions are controlled to make sure that clay adsorbed Np is either pentavalent or tetravalent. Batch sorption and spectroscopy studies appear to support the interpretation of Marsac et al. (2015) of surface-mediated reduction. Note, the amounts of Np(IV) found here were lower than postulated by Marsac et al. (2015). The respective mechanistic discussion listed structural Fe(II) as a possible reductant, inducing a relatively low redox potential. Furthermore, Ma et al. (2019) listed Fe(II)-containing minerals including clay minerals with structural Fe(II) as main electron donor for the retention mechanisms of redox-sensitive radionuclides.

3.3.2.2 Speciation of Np diffused through illite.

The same diffusion segments as investigated by leaching and solvent extraction with Np contents down to (18 ± 1) ppm were selected for further spectroscopic analysis. For the first time, these kinds of samples were studied by Np M_5-edge HR-XANES spectroscopy (Figure 73). As for the batch sorption samples, all spectra showed feature *B'* with variable intensity and a broader feature *A*, which implied the presence of Np(V) and Np(IV) in all segments. This indicated that a partial reduction of Np(V) to Np(IV) took place by IdP A during the diffusion process. The energy difference between feature *A* and *B'* was similar to the energy shift detected in the batch sorption samples (Figure 74), suggesting a similar Np(V) species on the IdP A surface. In conclusion, also in this case, a reduction reaction controlled by structural Fe(II) in IdP A seemed to have occurred. This supports the findings of the extraction studies:

While aerobic conditions prevail in the reservoirs, structural Fe(II) in the clay plug is capable to buffer the E_h in the pore space and to establish a more reducing environment.

3.3.2.3 Np L_3-edge EXAFS spectroscopy of Np sorbed on IdP A.

Np(V) reduction by structural Fe(II) requires close interaction of Np(V) with Fe to allow for electron transition. To examine the Np coordination environment, the EXAFS spectrum (Figure 75) of an IdP A batch sorption sample at pH 9 was analysed. The analysis confirmed the presence of solely sorbed mononuclear Np species, since the spectrum did not reveal any Np-O-Np coordination characteristic for NpO_2 precipitates, in contrast to studies using higher initial Np concentrations such as Kumar et al. (2022). The EXAFS analysis (Schacherl et al., 2023), Table SI 7) yielded two O atoms at a relatively short Np-O distance of (1.86 ± 0.01) Å, which were attributed to the axial O atoms of the NpO_2^+ ion (O_{ax}). The O_{ax} distances reported in literature for $Np(V)_{aq}$ range from (1.80 ± 0.02) Å (Antonio et al., 2001a) to (1.84 ± 0.01) Å (Ikeda-Ohno et al., 2008). For sorbed Np(V) species, slightly longer Np-O_{ax} distances of (1.840 ± 0.006) Å on gibbsite at pH 7.5 (Gückel et al., 2013), (1.86 ± 0.002) Å on corundum at pH 9 (Elo et al., 2017), or (1.887 ± 0.006) Å for Np(V) carbonate on hematite at pH 8.81 (Arai et al., 2007) were reported. The Np-O_{ax} distance found for Np on IdP A is comparable to literature data reported for surface-sorbed Np(V) species. In addition, a Np-O distance of (2.41 ± 0.01) Å with a coordination number of N = 4.0 ± 0.3 was detected for Np on IdP A at pH 9. This could be assigned to water molecules and illite hydroxyl groups in the equatorial plane of NpO_2^+ (O_{eq}). This distance is not only shorter than the Np-O_{eq} in $Np(V)_{aq}$ (2.484 to 2.49 Å) (Antonio et al., 2001a; Ikeda-Ohno et al., 2008), but also shorter than found for Np(V) sorbed onto corundum and gibbsite (Gückel et al., 2013) (2.45 to 2.50 Å). This hints at a stronger chemical bonding in the equatorial plane for Np on IdP A. This might also be the consequence of a partial reduction of Np(V) to Np(IV), since Np-O distances for sorbed Np(IV) were found to lie for the first shell between 2.24 Å and 2.27 Å and for the second shell between 2.41 Å and 2.44 Å (Denecke et al., 2002).

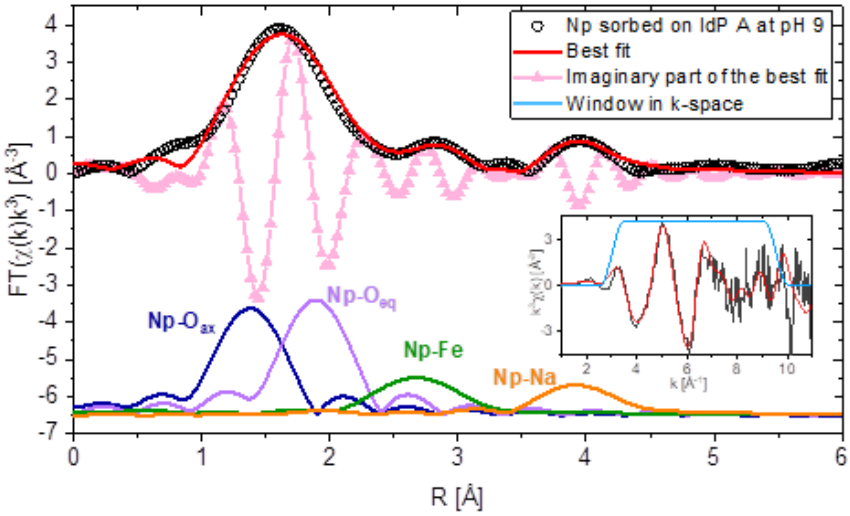

Figure 75. Fourier-transformed EXAFS spectrum in R-space of Np sorbed on IdP A at pH 9 (black circles), the imaginary part (rose triangles) and the best fit (red line). The contributions of each path are shown vertically shifted. Embedded is the k^3-weighted $\chi(k)$ (black line), the used window (blue line), and the best fit (red line) (Schacherl et al., 2023).

A Np-Fe coordination shell was found at (3.05 ± 0.02) Å suggesting that Np surface species were near Fe (N(Fe) = 1.0 ± 0.3) in IdP A. Al and Si, potentially present in the second coordination sphere of Np on the IdP A surface, were tested during the modelling of the EXAFS spectrum, too. However, a reasonably good fit (goodness of fit = 0.013 χ^2) was only obtained considering Fe. An additional contribution of Al to the second peak was not excluded, however this mixed model would be oversampling the data, since the fit did not significantly improve with the addition of this path. In addition, an Np-Na coordination was postulated at 4.34 ± 0.03 Å. This scattering path is reasonable since Na ions are present in the electrolyte solution and are coordinated at the basal surfaces and at the clay edges

around the surface sorbed Np for charge compensation. Other potentially present cations, such as Np, Al, Si, Mg, or K, were not appropriate to model this feature. The absence of a Np-Np scattering path verifies that Np is present as a solely sorbed species on the clay surface and no Np solid phases have formed. The results suggest that Np(V) sorbed onto IdP A is coordinated to the partially deprotonated hydroxyl groups surrounding the Fe atoms on the clay surface. The finding that Np is coordinated to Fe, in combination with the results of solvent extraction and HR-XANES spectroscopy, point to Fe-O entities as a strong complexation partner. Coordination of Cm(III) to Fe-OH entities of IdP was also discussed by Rabung et al. (2005) in a time-resolved laser-induced fluorescence study. Due to a strong decrease in fluorescence intensity because of static quenching, they concluded that a part of surface-complexed Cm(III) must be directly coordinated to Fe-OH groups. The presence of surficial Fe-OH ligands at clay edges is likely due to the Fe/Al ratio of 0.3 in IdP (Schacherl et al., 2023).

3.4 U reactivity towards phyllosilicates [CIEMAT]

Natural materials are heterogeneous, and a tiny proportion of accessory minerals can condition contaminant retention, which can be enhanced if new selective sorption sites are provided or by other processes. When simplified models are applied to natural environments, uranium retention may be over- or under-estimated, because simplified models are developed for purified materials and purification procedures usually remove the soluble salts and naturally present accessory minerals, so that their contribution is excluded. To verify the role of accessory Fe-phases on uranium retention, comparative sorption experiments on raw and Fe-oxide-free clays fractions were carried out.

3.4.1 Towards Fe-oxide-free phyllosilicate [CIEMAT]

[CIEMAT] carried out comparative ^{233}U(VI) sorption experiments on raw and *Fe-oxide-free* NAu-1 and FEBEX clay fractions, in which a dithionite treatment eliminated the accessory Fe-oxides naturally present in the clay. Results showed that U retention on nontronite was very similar to that observed in smectite and that, under the experimental conditions analysed, neither the natural content of Fe-oxides (< 5%) nor the amount of dissolved Fe(II)/Fe(III) played an important role on the overall U retention in the clays. Nevertheless, higher amount of iron oxides would improve uranium retention in smectite. More details on these results are described in (Alonso et al., In preparation).

3.4.2 Towards mixtures of smectite and Fe-phases [CIEMAT]

To elucidate the role of accessory Fe and to evaluate possible kinetic effects on ^{233}U(VI) retention, complementary sorption tests were performed in NAu-1 suspended in $NaClO_4$ 0.1 M at pH 8, including the presence of 5% in weight of different Fe sources: commercial metallic Fe(0) shavings, commercial hematite (Fe_2O_3) and laboratory synthetized magnetite (Fe_3O_4). For sorption experiments, contact times varied from 7 up to 200 days. The pH and Eh of samples was periodically measured.

The maximum sorption is reached at pH 7, with a maximum distribution coefficient of log Kd = 4.2 ± 0.2 mL/g. The retention of U(VI) by cation exchange mechanisms was limited and the competition of dissolved Fe^{2+} and Fe^{3+} was found to be minimal.

3.5 U, Se and Tc transport in compacted systems [CIEMAT]

Radionuclide transport/retention studies are carried out in solid compacted systems with the objective of verifying the up-scaling of radionuclide retention form simplified (batch) systems to more realistic conditions. Diffusion experiments in smectite and different Fe-oxides mixtures were carried out with ^{75}Se(IV), ^{233}U(VI) and ^{99}Tc(VII). The experimental cell designed to carry out radionuclide in-diffusion experiments with compacted bentonite is shown in Figure 76.

Figure 76. Experimental cell designed to carry out radionuclide in-diffusion experiments in compacted smectite samples mixed with known proportions of different Fe oxides and phases.

Results showed that the addition of Fe-oxides to bentonite reduce Se diffusivity due to enhanced retention, in agreement to what was observed in batch experiments. The experiments performed with Fe(0) shavings showed very limited diffusion due to strong selenium precipitation. When comparing experiments carried out with powder material or suspensions with diffusion / retention in smectite solid compacted state, it is evidenced that redox kinetic is not the same as in batch.

4. Interaction between redox-sensitive elements and clay-rocks

The previous section describes case-studies on the interactions between redox-sensitive elements and model clay minerals. The data provided through EURAD project especially highlights the role of Fe(II) and in various mineralogical compartments and the role of its accessibility regarding sorbates. The present section focuses on natural samples, namely COx and Romanian clay rocks. In comparison with model minerals, the preconditioning of natural samples by oxidation or reduction is difficult as it may cause significant perturbations to the mineralogical assemblage. It was decided to evaluate migration parameters in relevant conditions with the following questions of interest:

(1) What is the retention of U, Se Tc in natural samples and are these data comparable with those measured on model minerals?
(2) Is the reduction occurring in natural samples, with or without help of reducing agents / buffers, and if so, at what rate?
(3) What is the migration of redox-sensitive radionuclides (e.g., Se(-II), U(VI)), and does retention corroborate observations in crushed samples?

4.1 Mobility of elements in COx clay rock [CEA]

4.1.1 Migration of Uranium in COx clay rock

Sorption in batch experiments were performed with U(VI) at initial concentration ~10^{-7} mol/L higher than U *in situ* solubility. Retention was measured on raw (COx) and reduced samples (COx*), with or without a reductive agent (N_2H_4). One aim was to measure the meta-stability of U(VI) in natural system, and to confirm the retention of U(IV) and U(VI) under redox state and kinetics representative to *in situ* conditions. Results are illustrated in the Figure 77 show retention as a function of concentration measured after t = 24h. The adsorption of U(VI) was quantified to Rd(U(VI)/COx) = 3.9 ± 1.5 L/kg, in good agreement with data from literature Rd(U(VI)/COx) = 7.5 ± 1.6 L/kg in Fralova et al. (2021) and Rd(U(VI)/COx) = [3.6 – 8] L/kg in Montavon et al. (2022). The good agreement of these results is particularly remarkable regarding the high sensitivity of U(VI) retention to concentration of carbonates and pH. The use of a strong reductive compound leads to a fast increase of Rd(U) indicating combined contributions of both reduced U(IV) and U(VI) to U adsorption. The corresponding measurement is in the range Rd(U(red.)/COx) = 91.7 ± 1.6 L/kg in agreement with interpretation of labile fraction measured *in natural* conditions: Rd(U(VI)/COx) = [72-323] L/kg in Montavon et al. (2022). Still, the reduction of U(VI) into U(IV) as expected from *in situ* observations, was neither observed in absence of strongly reducing compound, nor in solid sample within 1 year (except in presence of bacterial activity). This slow reduction kinetics traduces a meta-stability of U(VI) in COx clay rock, probably linked to uranyl speciation

driven by calcium-carbonate ternary complexes (Shang et al., 2023). Data obtained on reduced samples displayed almost no retention, indicating a strong perturbation of solid samples. This highlights the fact that treatment used on purified clay samples might not be applicable to natural rocks and decarbonated samples.

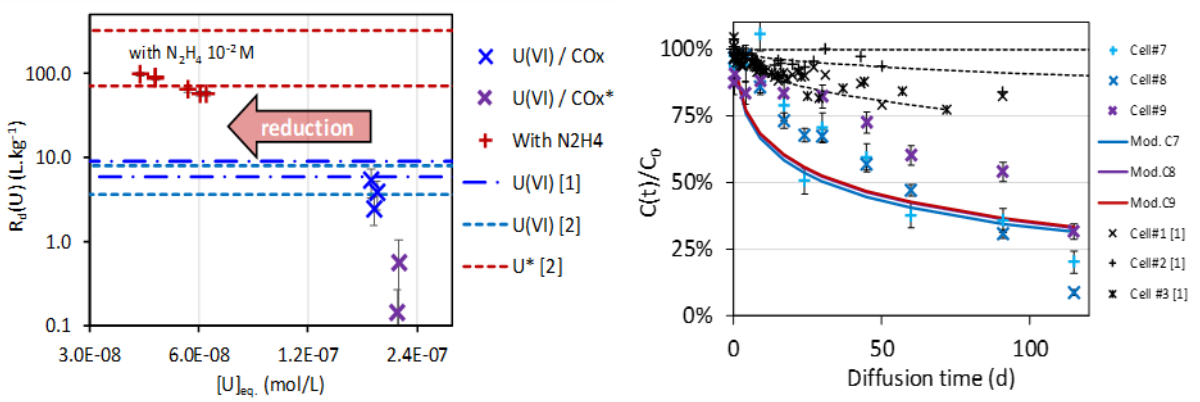

Figure 77. (Left) Adsorption data measured on U(VI) and U on COx, reduced samples (COx*) and in presence of reducing agent (tADS ~ 24h). Comparison with data from [1] (Fralova et al., 2021) and [2] (Montavon et al., 2022). (Right) Data from liquid monitoring during in-diffusion of U(VI) in COx; L:S ~ 0.7 L/kg. Comparison with previous data with L:S ~ 3 L/kg (Fralova et al., 2021).

Some results from the three in-diffusion cells are illustrated in the previous figure (Figure 77, right). The gathered experimental data include liquid monitoring of diffusion cells, out-diffusion experiment, and eventual desorption experiments on solid samples from abrasive peeling (diffusion profile). Compared to previous data available, the diffusion experiments aimed to minimize solution volume (i.e., high solid/ liquid ratios), in order to optimize the decrease of tracer concentration and favour reducing conditions imposed by clay rock buffering minerals. Diffusing parameters and retardation factors are obtained from the simultaneous parametric adjustment of all experimental data (in-diffusion, out-diffusion & diffusion profiles). Diffusive retardation factor leads to an estimate Rd(U(VI)/COx) = 8.7 L/kg, in good agreement with previous estimate Rd(U(VI)/COx) = 5.4 L/kg (Fralova, 2021) at higher L:S ratio. A slight difference between experimental data and shape of modelled curve is observed. Still, no clear reduction effect was observed within solid samples after 1 year of diffusion. This behaviour slightly differs from the reduction of Se(IV) observed in similar samples (Savoye et al., 2021). Such “meta-stability” of U(VI) was also confirmed by out-diffusion and desorption experiment. Finally, the low effective diffusion of uranyl De(U(VI)/COx) ~ 0.1 × De(HTO) traduces the strong size exclusion of diffusing solutes. This agrees with predicted major species: $Ca_2UO_2(CO_3)_3$& $Ca/MgUO_2(CO_3)_3^{2-}$ and exclusion estimated for this size of diffusing solutes (Dagnelie et al., 2018). The available studies and overall results on Cox clay rock and analogous samples provide a comprehensive view of speciation, retention and diffusion of Uranium in clay rocks (Montavon et al., 2022; Dagnelie et al., in prep.). Still, reduction kinetics of Uranyl complexes, U(VI) into U(V) and U(IV) strongly differs depending on materials (clay & NOM content, CO_3^{2-} activity), experimental conditions (biotic, abiotic), and the way reducing conditions are imposed. Further studies on this specific reduction kinetics would be especially interesting with a focus on natural systems.

4.1.2 Retention of Selenium in COx clay rock.

Retention of Selenium was measured using a purified ^{75}Se source (Figure 78). Purification was achieved by separation on ionic chromatography, to isolate Se(IV) from Se(VI). Purified Se(IV) was then reduced for 15 days using activated $H_{2(g)}$ under basic conditions, to limit Se(0) precipitation. The amount of reduced Se was quantified by ionic chromatography and gamma counting of eluted fractions. Corresponding results are illustrated in the following figure. Purification of ^{75}Se led to less than 1% of Se(VI). The yield of reduction was close Se(red.) ~68 ± 3% and Se(IV) ~31 ± 3% in the “spiking” solution. Small modifications of speciation were observed on reduced form of selenium during experiments with clay. Still corresponding species, e.g., Se(-II / 0) polymers, are yet to characterize as a function of pore water composition. Elution fractions measured by chromatography quantify the stability of reduced

selenium, in COx porewater, in absence of clay. An overall oxidation of Se was observed, with 43 ± 9% of the initial reduced form mostly oxidized into Se(IV). Such oxidation was mainly observed in presence of raw COx clay and in absence of N_2H_4.

Reduced Se spiking solution was furtherly used for adsorption experiments. Solid samples were similar to those previously discussed on uranium section (see section 4.1.1). Experiments 1-6 involve raw Cox samples without (1-3) or with (4-6) use of reductive compound, i.e., N_2H_4. Experiments 7-12 involve decarbonated and reduced Cox, also without (7-9) or with use of reductive compound N_2H_4 (9-12). Raw results are illustrated in the following figures. Measurement of ^{75}Se by gamma counting provided total adsorption of the element (black signs). For each system, 5 replicates are available including adsorption at 24h, 4 days and desorption experiments. Average measurements R_d(Se(red)/Cox) ~ 16 to 18 ± 9 L/kg are significantly below R_d(Se(IV)/COx) ~ 150-200 L/kg (Savoye et al., 2021). This difference comes from the lower retention of reduced Se and Se(VI) compared to Se(IV). Results obtained on reduced clay rock show similar trends to that on raw COx. This possibly indicates a retention mechanism linked to adsorption, independently of oxidative precipitation. Experimental results in more reductive media with N_2H_4 strongly differed. Corresponding R_d values are higher than R_d(Se(IV)), indicating a possible precipitation of selenium species or a perturbation cause by the reducing compound. This result shows some limitations to such experimental procedures to represent *in situ* conditions / equilibria within natural samples, despite similar Eh values (-200mV Vs SHE). Complementary chromatographic analysis on supernatant solutions helped to estimate adsorption of Se(Red.), Se(IV) and Se(VI). As expected, no retention could be observed for Se(VI). Concentration of Se(VI) at equilibrium, slightly higher than initial concentrations, mostly evidenced oxidation process. Retention of Se(IV) was close to expected data, except in presence of N_2H_4 and possible co-precipitation. Finally, a low but significant retention was also evidenced for reduced species, Se(red.) (e.g., Se(-II)). Further experiments would be interesting, to quantify more accurately both the speciation and the retention of the corresponding Se(-II) species under stabilized reducing conditions.

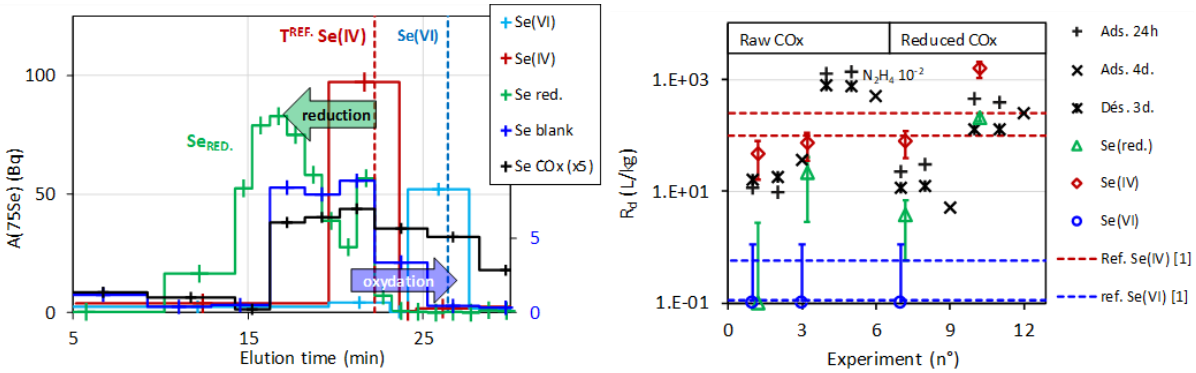

Figure 78. Reduction of Selenium and retention on COx clay rock. (Left) Chromatogram of Selenium source before / after purification and reduction and modification in COx porewater with or without clay rock. (Right) Se retention data on COx clay rock and reduced sample with or without N_2H_4. Raw Se adsorption (black) and contribution of species Se(red.), Se(IV) and Se(VI). Data compared to reference (Savoye et al., 2021).

4.2 Tc/Re sorption studies on local Romanian clay samples in oxidic/anoxic condition, with /without addition of reducing reagent: [RATEN]

Clay is one of the potential host rocks for the future Romanian geological repository, but also it is one of the main natural barrier for the near-surface disposal facility to be in operation in 2028. As Tc is one of the safety relevant radionuclides both for near-surface disposal facility and for the future geological repository, the sorption study performed by RATEN on pure clay mineral (Na-Montmorillonite) was extended to a natural clay rock from Saligny (the preferred site for hosting the near-surface repository). The investigations performed by RATEN in the frame of EURAD-FUTURE was focused on assessing

the Tc sorption on Romanian clay rock, both in oxidic conditions (relevant for near-surface disposal) and in anoxic conditions (relevant for geological disposal) to obtain experimental evidence needed to improve the modelling of this radionuclide migration.

4.2.1 Normal conditions – without DT addition

Initially, the Re sorption kinetics tests were performed under normal conditions (Figure 79), for a period of 90 days, with sampling intervals of 1, 2, 5, 7, 15, 28, 56 and 90 days. In the first part of the sorption kinetics test, the obtained results generally indicated higher Re concentrations in the aqueous phase compared to the initial Re concentration, which may suggest that Re concentrates in the aqueous phase most likely due to the anion exclusion phenomenon. The percentage of Re sorbed on clay increased up to 5% after 14 days of contacting and decreased to around 3% after ~30 days and kept almost constant until 90 days of testing.

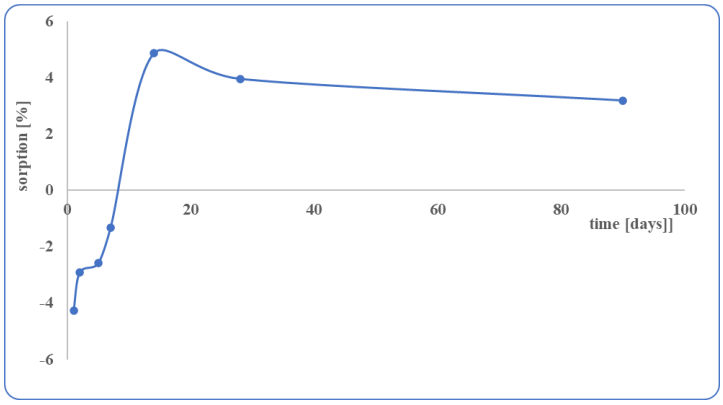

Figure 79. Re sorption kinetics under normal conditions on Saligny clay rocks.

These sorption data are correlated with the measured Eh values (Figure 80), which are characteristic for the oxidant conditions in which Re is found as ReO_4^-, species that is highly mobile with a negligible sorption on clay.

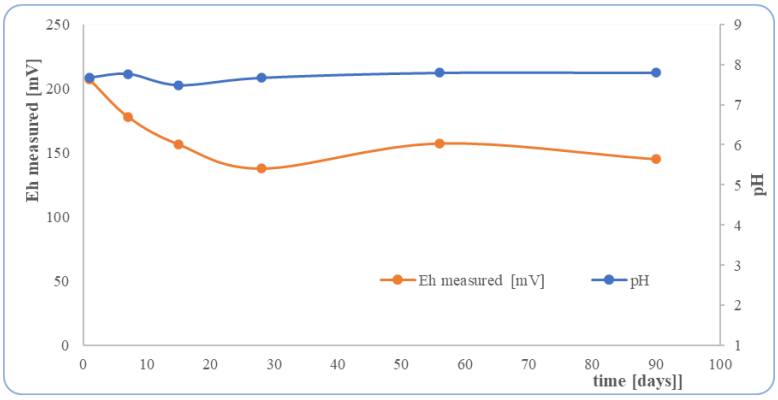

Figure 80. Evolution of Eh and pH as a function of time, during Re sorption in normal conditions on Saligny clay rock.

As from the sorption kinetics test it can be assumed that after 50 days the sorption equilibrium is attained, the aliquots from the test tubes prepared for the isotherm study, where sampled for Re measurement in aqueous phase. The experimental data can be reasonably well fitted with a linear sorption model (with a regression coefficient of 0.974 - Figure 81) and the distribution coefficient derived from the slope of the linear isotherm is 0.0013 L/g.

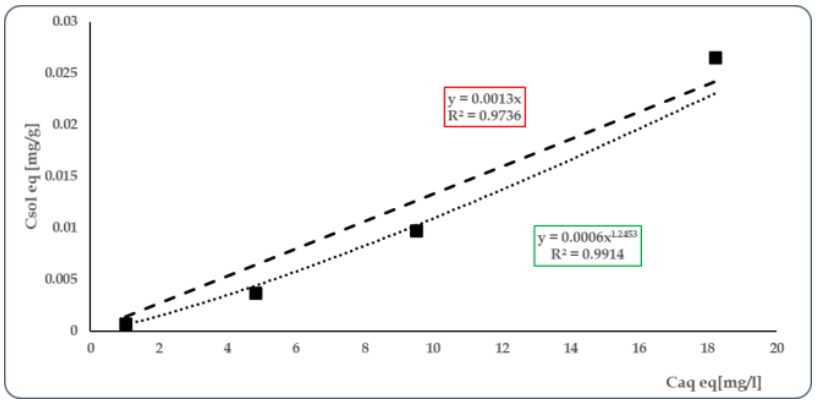

Figure 81. Linear modelling (lines) of Re adsorbed on Saligny clay rock as a function of aqueous Re.

By fitting the experimental data with a power-type function (R^2 =0.9915), representative for a Freundlich isotherm, the dimensionless parameter (N) is higher than 1 indicating that Re retention on clay under studied conditions is most likely through mechanisms involving precipitation/co-precipitation or surface complexation.

4.2.2 Normal conditions – with DT addition

By adding the reducing agent in the system, for a limited period a reducing environment is created allowing, according to the pH-Eh state diagram for Re, the conversion of Re(VII) to Re(IV), the form that is more easily retained on the clay. A ratio of 2:1 dithionite: clay develops a reducing environment with a measured redox potential of about -560mV (Figure 82).

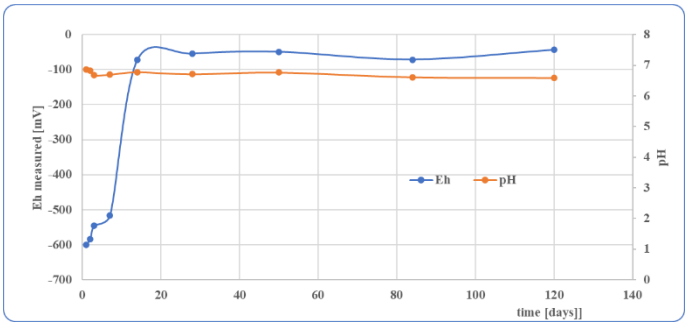

Figure 82. Evolution of Eh and pH as a function of time, under normal conditions, with DT addition.

From the sorption kinetics tests of Re sorption on Romanian clay sample under normal conditions with reducing addition agent a significant retention of Re on the clay (~50% from the initial Re in aqueous solution) is observed for the first 14 days of sorption test in which the redox potential was in the range of reducing conditions by the added sodium dithionite. After this period, the sorption percentage decreased to ~30% due to the alteration of redox conditions. A correlation is observed between the increases in Re concentration in the aqueous phase (equivalent to a lower sorption percentage) with the decreases in Fe concentration in the aqueous phase, which could imply that Fe is retained on the accessible exchange positions, while Re is oxidized to Re(VII) and desorbed from the clay surface, but these assumptions must be confirmed by microelectronic spectroscopy and X-ray spectrometry studies.

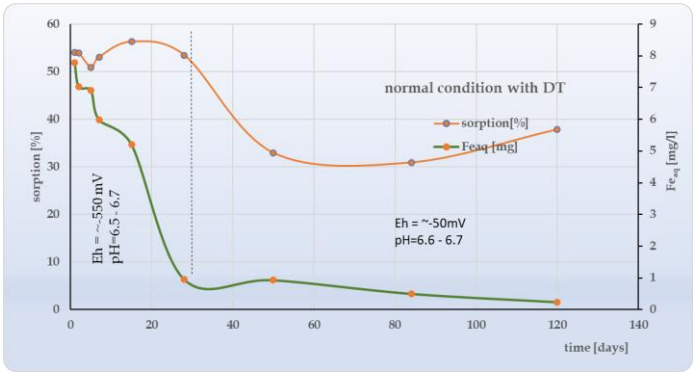

Figure 83. Re sorption (orange solid line) and Eh (green solid line) as a function of time, in normal condition with DT.

As the addition of reducing agent does not ensure a constant redox condition to be able to achieve the sorption equilibrium, and the sorption isotherm was not derived.

4.2.3 Anoxic conditions – without DT addition

The sorption kinetics tests carried out under anoxic conditions (inside glove bags with O_2 content less than 0.1%) do not indicate a better sorption of Re on clayey rock, most probably because the redox potential measured is in oxidizing range (measured Eh=143-150 mV) which favours the presence of Re in the form of ReO_4^-. In the first part of the testing interval, the experimental data indicated a similar sorption percentage with the tests performed in normal conditions, with a maximum of ~5% after 7 days, after which an increase in the Re concentration values in the aqueous phase is observed (Figure 84).

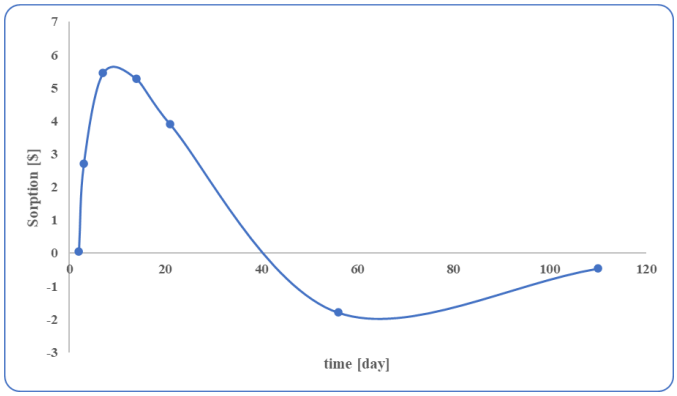

Figure 84. Re sorption kinetics under anoxic conditions, without DT addition.

4.2.4 Anoxic conditions – with DT addition

The addition of sodium dithionite as a reducing agent in the oxygen-free atmosphere allowed leads maintaining for more than 7 days of a reducing environment favourable to the reduction of Re (VII) to Re(IV), according to the pH-Eh state diagram. The reduction to the oxidation state +4 is highlighted by the higher sorption (~50%) obtained after 14 days of test (Figure 85).

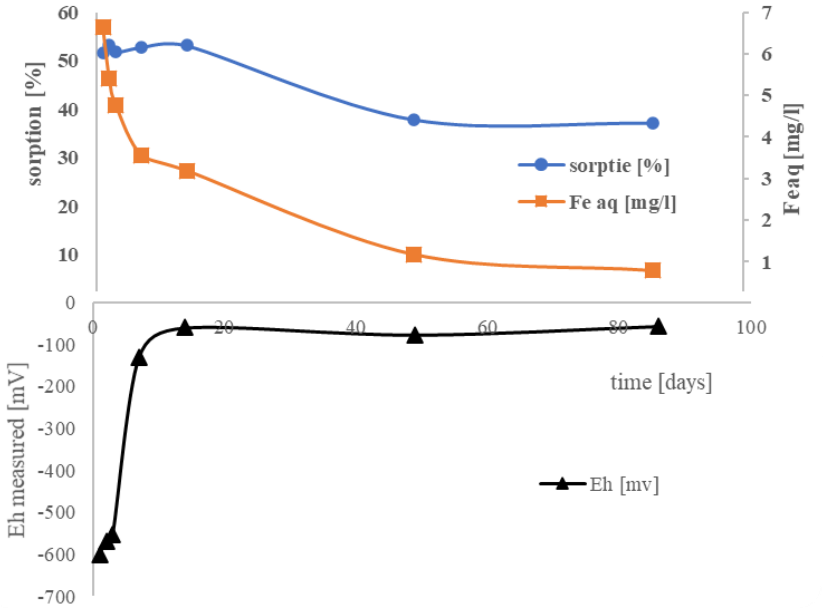

Figure 85. Top: sorption percentage (blue solid line) and Fe concentration in solution (orange solid line) as a function of time. Bottom: evolution of the Eh value as a function of time.

With the increase of the redox potential, an increase in the concentration of Re in the aqueous phase is observed, but also a decrease in the concentration of Fe in the solution - a behaviour similar as those observe in tests carried out in the normal atmosphere with the addition of a reducing agent. After 86 days of analysis, the sorption stabilizes at a value of ~35%.

As the higher sorption was observed during first days of testing, Re distribution ratio was computed for 7 and 14 days, for Re initial concentration in aqueous phase ranging between 10^{-6} mol/L and 10^{-4} mol/L (Table 28). For this period in which the Eh values were in the reducing conditions Re sorption is low, with a distribution ratio of around 0.004 L/g.

Table 28. Initial, equilibrium, and sorbed Re concentration in the different experiments, and related individual and average Rd, and experiment time.

Re initial [mg/L]	**Re_{aq} [mg/l]**	**Re_{sorbed} [mg/g]**	**Rd, L/g**	**time**
5.37E-6	0.8648	0.0027	0.0031	7 days
2.68E-5	3.6269	0.0275	0.0076	
5.36E-5	8.8523	0.0302	0.0034	
1.00E-4	17.7094	0.0554	0.0031	
average Rd: ~ **0.004 L/g**				
5.37E-6	0.7396	0.005209	0.0070	14 days
2.68E-5	4.25442	0.014912	0.0035	
5.36E-5	8.76666	0.024667	0.0028	
1.00E-4	16.6446	0.0671	0.0040	
average Rd: ~ **0.004 L/g**				

5. Conclusions and knowledge gaps [All groups]

5.1 General conclusion

The excellent and state-of-the-art work carried out by the partners within the Redox task allowed to improve the understanding of the interaction mechanisms between Fe-bearing minerals and several radionuclides (or their stable analogues) relevant to the deep geological storage of radioactive waste. This was achieved by combining several techniques, ranging from laboratory chemical measurements and mineralogical analyses to speciation measurement, using various complementary techniques (e.g., Mossbauer spectrometry, XPS, synchrotron XAS), and ab-initio simulations. New insights could also be gained thanks to development of analytical infrastructure at synchrotron beamlines.

This short conclusive section does not aim at summarizing all results obtained in this task, which are extensively described in the previous sections of this document. Rather, a few examples are presented to illustrate the complementarity of the results obtained by the different partners and the new insights gained.

Se behaviour:

It could be demonstrated that selenite is reduced by clays containing redox-active Fe(II). However, a "poisoning" effect is observed when the phyllosilicate Fe(II) content is too high. Indeed, reduction of selenite was observed to be inhibited in nontronites with Fe(II)/Fe(III) ratio 0.3 and higher. Independently of the concentrations of Se(IV) used, the observed reaction product is always Se(0). The crystallographic form of Se(0), however, was found to depend on the reaction kinetics, and was either grey or red Se(0). Red Se(0) was observed in experiments that lasted 7d, and grey Se(0) in experiments lasting for 3 months. Kinetics were also observed for the reduction process itself. In Se(IV) sorption experiments performed with SWy-1 and STx-1, the proportion of reduced Se increased with reaction time. The role of the solution chemistry was also evidenced on "low-reduced" nontronite (i.e., Fe(II)/Fe(III) of ~0.2/0.8) for instance. At pH7 Se reduction was observed whereas at pH 8.5 no reduction was observed. Chemical condition also influenced sorption kinetics, with a higher sorption kinetics by nontronite was observed at pH 5 than a pH 8, under anoxic conditions.

The interaction of oxidized selenium (Se(VI) with other Fe-containing solids was also found to be controlled by redox reactions and could be quantified thanks to state-of-the-art analytical techniques. When Se(VI) was contacted with magnetite, sorption was observed. This sorption was higher at pH 5 than pH 7, hence again highlighting the importance of a sound chemical characterization of the system to improve our understanding of reaction mechanisms. Se(VI) sorption was accompanied by Fe co-sorption, and lead to the reduction of Se(VI) to both Se(IV) and Se(0), and to the transformation of the external surfaces of magnetite to maghemite. Se(0) was observed to have nanowires morphology. A quite similar mechanism was observed in the case of Se(VI) interaction with green rust containing interlayer Cl, where Se(VI) was reduced to Se(0) in a two-steps process, with Se(VI) being first reduced to Se(IV) before being adsorbed in green rust interlayer, and finally reduced to Se(0) under the form of nanoparticles having sizes smaller than 20 nm.

Tc and Re behaviour

Tc(VII) and Re(VII) (used as a chemical analogue) like Se, appear to have fast sorption kinetics. For Re, log(Rd) values on phyllosilicates of ~1 under oxic conditions were measured, while log(Rd) increased up to 1.5 under anoxic conditions was observed, highlighting again the importance of controlling the chemical conditions. Re(VII) sorption kinetics was also fast in presence of nontronite, with sorption being higher of about an order of magnitude in Rd units at pH 8 than 5. Rd was also highly influenced by the structural Fe(II) content of the phyllosilicate, with the log(Tc sorbed) being apparently linearly related to log(Fe(II)). In addition, in was also shown that Fe(II) adsorbed on the clay mineral, bounded, also considerably increased Tc sorption. This sorption phenomenon however does not behave linearly, due to Tc reduction by phyllosilicates and subsequent formation of $Tc(IV)O_2 \cdot xH_2O$ nano-sized clusters, as evidenced by XAS spectroscopy.

Up to now the structure of Tc(IV)$O_2 \cdot xH_2O$ was unclear and debated. The DFT study performed within the redox subtask on the structure of Tc(IV)$O_2 \cdot xH_2O$ lead to the conclusion that this precipitate has zig-zag chains that are prone to combine at long reaction times (years) and form longer chains and cross-linked structures. Upon subsequent dehydration, this is possibly a mechanism of beta-TcO_2 formation.

When contacted with magnetite, Re(VII) was also reduced to Re(IV), but the sorption under the investigated chemical conditions (pH 5-8, 10 g/L, 4.3 mM) was much lower than that of Tc (40 %). Re sorption on crushed clay rock was also limited. As for the other redox-sensitive elements investigated in this task, the importance of carrying out the sorption experiments on well characterized materials and under well-defined and controlled chemical conditions (pH, eh, I, …) is crucial to be able to interpret the data. Indeed, under anoxic but oxidizing conditions, the sorption is very low (1 % for an initial Re concentration of 5.3 10^{-5} M), but when the system is then turned to reducing conditions, sorption increases (up to 50 %), and decreases again when the system is returned to oxidizing conditions.

Np and U behaviour:

Np(V) retention on Illite du Puy (IdP) was investigated essential for understanding the migration behaviour of Np in argillaceous environments. Presence of structural Fe(III) and Fe(II) in IdP was confirmed by Fe K-edge X-ray absorption near-edge structure (XANES) and ^{57}Fe Mössbauer spectroscopy. In batch sorption experiments, a higher Np sorption affinity to IdP was found than to Wyoming smectite or iron-free synthetic montmorillonite. An increase of the relative Np(IV) ratio sorbed onto IdP with decreasing pH was observed by solvent extraction (up to 24±2 % at pH 5, c_0(Np) = 10^{-6} mol/L). Furthermore, up to 33±5 % Np(IV) could be detected in IdP diffusion samples at pH 5. Respective Np M_5-edge high-energy resolution (HR-)XANES spectra suggested the presence of Np(IV/V) mixtures and weakened axial bond covalency of the NpO_2^+ species sorbed onto IdP. Np L_3-edge extended X-ray absorption fine structure (EXAFS) analysis showed that significant fractions of Np were coordinated to Fe-O entities at pH 9. This highlights the potential role of Fe(II/III) clay edge sites as a strong Np(V) surface complex partner and points to the partial reduction of sorbed Np(V) to Np(IV) via structural Fe(II).

Finally, the importance of a detailed knowledge about aqueous chemistry, but also having an exhaustive thermodynamic database, including well-documented kinetics, was illustrated with U(VI) diffusion through a compacted clay rock. The Rd coefficient measured was about 8.7 L/kg and, very importantly, the influence of U-carbonates complexes on the mobility and reduction susceptibility of U was observed and supports the already existing knowledge. U(VI) stayed unreduced over the whole duration of the experiment (~600 d), even if conditions were anoxic, and if the clay rock contained Fe(II), for example as pyrite.

In the essence, this task has illustrated the necessity to adopt a multi-scale and multi-technique approach in characterizing the heterogeneous redox reactions of relevance for radioactive waste storage. It could be demonstrated that the reactivity towards Fe(II)-containing solids is generally high, and leads to changes in redox state, hence decreasing the mobility of the elements and making the Kd approach unable to reproduce, and hence predict, the interaction between the studied elements and the Fe-containing minerals studied in this task.

5.2 Developments of analytical infrastructure and synchrotron-based characterisation techniques

Exceptional progress in the state-of-the-art molecular scale characterisation of the retention mechanism achieved in this project would not be possible without development of advanced analytical techniques and pushing further the detection limits of synchrotron based instrumental infrastructure. Particularly relevant to redox sensitive element is the ability conduct fast measurement for preserving the pristine state of the measured species and minimising potential damage of samples by X-ray beam.

ROBL developed HERFD-XANES, extending the energy range down to 3 keV to be able to also measure actinide M-edges, thereby offering superior resolution of oxidation states.

Five years after its initial commissioning, the ACT-station at the CAT-ACT wiggler beamline has been developed into a unique X-ray spectroscopy station for the investigation of various radionuclide materials with state of the art speciation techniques – strongly focusing on 'flux-hungry' photon-in / photon-out techniques (Schacherl et al., 2022b). For the first time, Np M5-edge HR-XANES spectroscopy on Np sorbed on illite was performed. Notably, M5-edge HR-XANES spectra for this system were recorded down to 1.24 ± 0.04 ppm of Np. Apparently, the chemical environment of adsorbed Np has a significant impact on the spectral shape. Therefore, the unequivocal discrimination of Np redox states requires further investigations using appropriate reference samples. Detailed study and elimination of beam-induced changes of the Np on clay samples is mandatory as illustrated in this study. It was shown that such beam-induced Np oxidation state changes for the present photon flux densities ($(5.2 \pm 0.2) \times 10^{10}$ ph/(s mm^2) at 3664 eV) at the CAT- ACT beamline could be excluded by cooling the samples down to 141.2 ± 1.5 K. With further experimental optimisation, a higher S/N and thus Np speciation at 1 ppm or even lower Np loadings should be achievable. These findings demonstrate that it is possible to perform in parallel HR-XANES and batch sorption experiments over a range of Np concentrations down to trace level. Note, based on the instrumental improvements, the detection limit achieved is valid for NpM_5-edge HR-XANES spectroscopy. It is expected to be similar for all An $M_{4,5}$ and most $M_{1\text{-}3}$ absorption edges from U to Cm. High diffraction order for the used analyser crystals and an as close as possible to 90° Bragg angle are required for low detection limits. In the case of EXAFS spectroscopy, one of the described technical improvements, i.e., cooling down the sample to cryogenic temperatures, will reduce beam-induced oxidation state changes. However, different experimental improvements are required to achieve lower detection limits for EXAFS spectroscopy, which will be the focus of future work. The described technique provides Np speciation information for a large range of analyte concentrations, which allows for a consistent understanding and modelling of molecular scale spectroscopic data and macroscopic batch sorption data. Spectroscopic methods optimised towards highest sensitivity will allow as well for the direct examination of An oxidation states at low loadings, which are very often observed in contaminated sites and which are typical for the expected An behaviour in repository systems.

6. References

Abràmoff, M.D., Magalhães, P.J., Ram, S.J., 2004. Image Processing with ImageJ. Biophotonics International 11, 36-42.

Alonso , U., Missana, T., Fernandez, A.M., Garcia-Gutierrez, M., In preparation. Role of Fe on U(VI) retention in clayey rocks: Fe in the clay structure, in accessory minerals or aqueous phase.

Amidani, L., Plakhova, T.V., Romanchuk, A.Y., Gerber, E., Weiss, S., Efimenko, A., Sahle, C.J., Butorin, S.M., Kalmykov, S.N., Kvashnina, K.O., 2019. Understanding the size effects on the electronic structure of ThO2 nanoparticles. Physical Chemistry Chemical Physics 21, 10635-10643.

Amonette, J.E., Charles Templeton, J., 1998. Improvements to the quantitative assay of nonrefractory minerals for Fe(II) and total Fe using 1,10-phenanthroline. Clays and Clay Minerals 46, 51-62.

Antonio, M.R., Soderholm, L., Williams, C.W., Blaudeau, J.-P.P., Bursten, B.E., 2001a. Neptunium redox speciation. Radiochimica Acta 89, 17-25.

Antonio, R., Soderholm, L., Williams, C.W., Blaudeau, J.-P., Bursten, B.E., 2001b. Neptunium redox speciation. Radiochimica Acta 89, 17-26.

Arai, Y., Moran, P.B., Honeyman, B.D., Davis, J.A., 2007. In Situ spectroscopic Evidence for Neptunium(V)-Carbonate Inner-Sphere and Outer-Sphere Ternary Surface Complexes on Hematite Surfaces. Environmental Science & Technology 41, 3940-3944.

Asaad, A., Hubert, F., Dazas, B., Razafitianamaharavo, A., Brunet, J., Glaus, M.A., Savoye, S., Ferrage, E., Tertre, E., 2022. A baseline study of mineralogical and morphological properties of different size fractions of illite du Puy. Applied Clay Science 224, 106517-106517.

Baeyens, B., Bradbury, M.H., 1997. A mechanistic description of Ni and Zn sorption on Na-

montmorillonite Part I: Titration and sorption measurements. Journal of Contaminant Hydrology 27, 199-222.

Barton, C.D., Karathanasis, A.D., 2002. Clay Minerals. In: Lal, R., Ed., Encyclopedia of Soil Science, Marcel Dekker, New York, USA, 187-192.

Beck, A., Bohnert, E., Fellhauer, D., Hardock, K., Joseph, C., Krepper, V., Marquardt, C., Rieder, F., Rothe, J., Schacherl, B., Vitova, T., 2020. Chapter 5.2 Diffusion, in: Geckeis, H., Altmaier, M., Fanghänel, S. (Eds.). KIT scientific publishing, Karlsruhe, pp. 33-35.

Bertrand, P.A., Choppin, G.R., 1982. Separation of actinides in different oxidation states by solvent extraction. Radiochimica Acta 31, 135-137.

Bianchetti, E., Di Valentin, C., 2022. Mechanism of spin ordering in Fe3O4 nanoparticles by surface coating with organic acids. Materials Today Nano 17.

Bianchetti, E., Oliveira, A.F., Scheinost, A.C., Valentin, C.D., Seifert, G., 2023. Chemistry of the interaction and retention of Tc^{VII} and Tc^{IV} species at the Fe_3O_4(001) surface. Journal of Physical Chemistry C 127, 7674–7682.

Bliem, R., Pavelec, J., Gamba, O., McDermott, E., Wang, Z., Gerhold, S., Wagner, M., Osiecki, J., Schulte, K., Schmid, M., Blaha, P., Diebold, U., Parkinson, G.S., 2015. Adsorption and incorporation of transition metals at the magnetite Fe3O4(001) surface. Physical Review B 92.

Blum, V., Gehrke, R., Hanke, F., Havu, P., Havu, V., Ren, X., Reuter, K., Scheffler, M., 2009. Ab initio molecular simulations with numeric atom-centered orbitals. Computer Physics Communications 180, 2175-2196.

Bots, P., Shaw, S., Law, G.T.W., Marshall, T.A., Mosselmans, J.F.W., Morris, K., 2016. Controls on the fate and speciation of Np(V) during iron (oxyhydr)oxide crystallization. Environmental Science & Technology 50, 3382-3390.

Bradbury, M.H., Baeyens, B., 2005. Experimental and modelling investigations on Na-illite: Acid-base behaviour and the sorption of strontium, nickel, europium and uranyl; PSI 05-02, pp. 88-88.

Bradbury, M.H., Baeyens, B., 2009a. Sorption modelling on illite Part I: Titration measurements and the sorption of Ni, Co, Eu and Sn. Geochimica Et Cosmochimica Acta 73, 990-1003.

Bradbury, M.H., Baeyens, B., 2009b. Sorption modelling on illite. Part II: Actinide sorption and linear free energy relationships. Geochimica Et Cosmochimica Acta 73, 1004-1013.

Brendebach, B., Banik, N.L., Marquardt, C.M., Rothe, J., Denecke, M., Geckeis, H., 2009. X-ray absorption spectroscopic study of trivalent and tetravalent actinides in solution at varying pH values. Radiochimica Acta 97, 701-708.

Brunauer, S., Emmett, P.H., Teller, E., 1938. Adsorption of Gases in Multimolecular Layers. Journal of the American Chemical Society 60, 309-319.

Charlet, L., Scheinost, A.C., Tournassat, C., Greneche, J.-M., Géhin, A., Fernandez-Martinez, A., Coudert, S., Tisserand, D., Brendle, J., 2007a. Electron transfer at the mineral/water interface: Selenium reduction by ferrous iron sorbed on clay. Geochimica et Cosmochimica Acta 71, 5731–5749.

Charlet, L., Scheinost, A.C., Tournassat, C., Greneche, J.-M., Géhin, A., Fernández-Martínez, A., Coudert, S., Tisserand, D., Brendle, J., 2007b. Electron transfer at the mineral/water interface: Selenium reduction by ferrous iron sorbed on clay. Geochimica et Cosmochimica Acta 71, 5731-5749.

Charlet, L., Tournassat, C., Grenèche, J.-M., Wersin, P., Géhin, A., Hadi, J., 2023. Mössbauer spectrometry insights into the redox reactivity of Fe-bearing phases in the environment. Journal of Materials Research 38, 958-973.

Combes, J.M., Chisholm-Brause, C.J., Brown, G.E., Parks, G.A., Conradson, S.D., Eller, P.G., Triay, I.R., Hobart, D.E., Miejer, A., 1992. EXAFS spectroscopic study of neptunium(V) sorption at the α-FeOOH/Water interface. Environmental Science & Technology 26, 376-382.

Cornell, R.M., Schwertmann, U., 2003. The Iron Oxides: Structure, Properties, Reactions, Occurences and Uses. WILEY-VCH Verlag GmbH & Co., KGaA, Weinheim, 659.

Cuttler, A.H., Man, V., Cranshaw, T.E., Longworth, G., 1990. A Mössbauer study of green rust precipitates. 1. Preparations form sulfate-solutions. . Clay Minerals 25, 289-301.

Dagnelie, R.V.H., Rasamimanana, S., Blin, V., Radwan, J., Thory, E., Robinet, J.C., Lefèvre, G., 2018. Diffusion of organic anions in clay-rich media: Retardation and effect of anion exclusion. Chemosphere 213, 472-480.

Decarreau, A., Petit, S., Martin, F., Farges, F., Vieillard, P., Joussein, E., 2008. Hydrothermal synthesis, between 75 and 150°C, of high-charge, ferric nontronites. Clays and Clay Minerals 56, 322-337.

Denecke, M.A., 2006. Actinide speciation using X-ray absorption fine structure spectroscopy. Coordination Chemistry Reviews 250, 730-754.

Denecke, M.A., Marquardt, C.M., Rothe, J., Dardenne, K., Jensen, M.P., 2002. XAFS study of actinide coordination structure in Np(IV)-fulvates. Journal of Nuclear Science and Technology 39, 410-413.

Dovesi, R., Erba, A., Orlando, R., Zicovich-Wilson, C.M., Civalleri, B., Maschio, L., Rerat, M., Casassa, S., Baima, J., Salustro, S., Kirtman, B., 2018. Quantum-mechanical condensed matter simulations with CRYSTAL. Wiley Interdisciplinary Reviews-Computational Molecular Science 8.

Dumas, T., Fellhauer, D., Schild, D., Gaona, X., Altmaier, M., Scheinost, A.C., 2019. Plutonium retention mechanisms by magnetite under anoxic conditions: Entrapment versus sorption. ACS Earth and Space Chemistry 3, 2197-2206.

Elo, O., Müller, K., Ikeda-Ohno, A., Bok, F., Scheinost, A.C., Hölttä, P., Huittinen, N., 2017. Batch sorption and spectroscopic speciation studies of neptunium uptake by montmorillonite and corundum. Geochimica et Cosmochimica Acta 198, 168-181.

F. Courchesne, F., Turmel, M.-C., Chapter 26: Extractable Al, Fe, Mn, and Si, in: Carter, M.R., Gregorich, E.G. (Eds.), Soil Sampling and Methods of Analysis. Canadian Society of Soil Science.

Fernández, A.M., Villar, M.V., 2010. Geochemical behaviour of a bentonite barrier in the laboratory after up to 8 years of heating and hydration. Applied Geochemistry 25, 809-824.

Ferreira, F.F., Correa, H.P.S., Orlando, M.T.D., Passamai, J.L., Jr., Orlando, C.G.P., Cavalcante, I.P., Garcia, F., Tamura, E., Martinez, L.G., Rossi, J.L., de Melo, F.C.L., 2009. Pressure study of monoclinic ReO2 up to 1.2 GPa using X-ray absorption spectroscopy and X-ray diffraction. Journal of Synchrotron Radiation 16, 48-56.

Fralova, L., 2021. Transport diffusif de l'uranium dans la roche argileuse du Callovo-Oxfordien, mécanismes et sensibilité aux perturbations chimiques, Thèse de Doctorat, ED388, Université PSL, 14 décembre 2020.

Fralova, L., Lefèvre, G., Madé, B., Marsac, R., Thory, E., Dagnelie, R.V.H., 2021. Effect of organic compounds on the retention of radionuclides in clay rocks: Mechanisms and specificities of Eu(III), Th(IV), and U(VI). Applied Geochemistry 127, 104859.

Fröhlich, D.R., Amayri, S., Drebert, J., Grolimund, D., Huth, J., Kaplan, U., Krause, J., Reich, T., 2012. Speciation of Np(V) uptake by Opalinus Clay using synchrotron microbeam techniques. Analytical and Bioanalytical Chemistry 404, 2151-2162.

Gaona, X., Tits, J., Dardenne, K., Liu, X., Rothe, J., Denecke, M.A., Wieland, E., Altmaier, M., 2012. Spectroscopic investigations of Np(V/VI) redox speciation in hyperalkaline TMA-(OH, Cl) solutions.

Radiochimica Acta 100, 759-770.

Gaona, X., Wieland, E., Tits, J., Scheinost, A.C., Dähn, R., 2013. Np(V/VI) redox chemistry in cementitious systems: XAFS investigations on the speciation under anoxic and oxidizing conditions. Applied Geochemistry 28, 109-118.

Glatzel, P., Bergmann, U., 2005. High resolution 1s core hole X-ray spectroscopy in 3d transition metal complexes—electronic and structural information. Coordination Chemistry Reviews 249, 65-95.

Gorski, C.A., Aeschbacher, M., Soltermann, D., Voegelin, A., Baeyens, B., Marques Fernandes, M., Hofstetter, T.B., Sander, M., 2012a. Redox Properties of Structural Fe in Clay Minerals. 1. Electrochemical Quantification of Electron-Donating and -Accepting Capacities of Smectites. Environmental Science & Technology 46, 9360-9368.

Gorski, C.A., Klüpfel, L., Voegelin, A., Sander, M., Hofstetter, T.B., 2012b. Redox Properties of Structural Fe in Clay Minerals. 2. Electrochemical and Spectroscopic Characterization of Electron Transfer Irreversibility in Ferruginous Smectite, SWa-1. Environmental Science & Technology 46, 9369-9377.

Gorski, C.A., Klüpfel, L.E., Voegelin, A., Sander, M., Hofstetter, T.B., 2013. Redox Properties of Structural Fe in Clay Minerals: 3. Relationships between Smectite Redox and Structural Properties. Environmental Science & Technology 47, 13477-13485.

Göttlicher, J., Steininger, R., Mangold, S., Spangenberg, T., Veselska, V., Eiche, E., Schneider, M., Neumann, T., Penkert, G., Penkert, P., 2018. Application of X-ray absorption spectroscopy in earth and environmental sciences.

Gregg, S., Sing, K., 1982. Adsorption, Surface Area and Porosity.

Grimme, S., Antony, J., Ehrlich, S., Krieg, H., 2010. A consistent and accurate ab initio parametrization of density functional dispersion correction (DFT-D) for the 94 elements H-Pu. Journal of Chemical Physics 132.

Gückel, K., Rossberg, A., Müller, K., Brendler, V., Bernhard, G., Foerstendorf, H., 2013. Spectroscopic identification of binary and ternary surface complexes of Np(V) on gibbsite. Environmental Science & Technology 47, 14418-14425.

Hadi, J., Grangeon, S., Warmont, F., Seron, A., Greneche, J.-M., 2014. A novel and easy chemical-clock synthesis of nanocrystalline iron–cobalt bearing layered double hydroxides. Journal of Colloid and Interface Science 434, 130-140.

Handler, R.M., Beard, B.L., Johnson, C.M., Rosso, K.M., Scherer, M.M., 2009. Kinetics of atom exchange between aqueous Fe(II) and goethite. Abstracts of Papers of the American Chemical Society 237.

Heald, S.M., Krupka, K.M., Brown, C.F., 2012. Incorporation of pertechnetate and perrhenate into corroded steel surfaces studied by X-ray absorption fine structure spectroscopy. Radiochimica Acta 100, 243-253.

Heberling, F., Brendebach, B., Bosbach, D., 2008. Neptunium(V) adsorption to calcite. Journal of Contaminant Hydrology 102, 246-252.

Heberling, F., Scheinost, A.C., Bosbach, D., 2011. Formation of a ternary neptunyl(V) biscarbonato inner-sphere sorption complex inhibits calcite growth rate. Journal of Contaminant Hydrology 124, 50-56.

Heyd, J., Scuseria, G.E., Ernzerhof, M., 2003. Hybrid functionals based on a screened Coulomb potential. Journal of Chemical Physics 118, 8207-8215.

Heyd, J., Scuseria, G.E., Ernzerhof, M., 2006. Hybrid functionals based on a screened Coulomb

potential (vol 118, pg 8207, 2003). Journal of Chemical Physics 124.

Huang, J., Jones, A., Waite, T.D., Chen, Y., Huang, X., Rosso, K.M., Kappler, A., Mansor, M., Tratnyek, P.G., Zhang, H., 2021. Fe(II) Redox Chemistry in the Environment. Chem. Rev. 121, 8161-8233.

Huertas, F., Fuentes-Santillana, J.L., Jullien, F., Rivas, P., Linares, J., Fariña, P., Ghoreychi, M., Jockwer, N., Kickmaier, W., Martínez, M.A., Samper, J., Alonso, E., Elorza, F.J., 2000. Full scale engineered barriers experiment for a deep geological repository for high-level radioactive waste in crystalline host rock. EC Final REPORT EUR 19147.

Hulva, J., Meier, M., Bliem, R., Jakub, Z., Kraushofer, F., Schmid, M., Diebold, U., Franchini, C., Parkinson, G.S., 2021. Unraveling CO adsorption on model single-atom catalysts. Science 371, 375-+.

Ikeda-Ohno, A., Hennig, C., Rossberg, A., Funke, H., Scheinost, A.C., Bernhard, G., Yaita, T., 2008. Electrochemical and Complexation Behavior of Neptunium in Aqueous Perchlorate and Nitrate Solutions. Inorg. Chem. 47, 8294-8305.

Ivanovskii, A.L., Chupakhina, T.I., Zubkov, V.G., Tyutyunnik, A.P., Krasilnikov, V.N., Bazuev, G.V., Okatov, S.V., Lichtenstein, A.I., 2005. Structure and electronic properties of new rutile-like rhenium (IV) dioxide ReO2. Physics Letters A 348, 66-70.

Jackson, M.L., 2005. Soil chemical analysis-advanced course: Advanced Course : a Manual of Methods Useful for Instruction and Research in Soil Chemistry, Physical Chemistry of Soils, Soil Fertility, and Soil Genesis. . Parallel Press.

Jolivet, J.P., Belleville, P., Tronc, E., Livage, J., 1992. Influence of Fe(II) on the Formation of the Spinel Iron Oxide in Alkaline Medium. Clays and Clay Minerals 40, 531-539.

Keeling, P.S., Kirby, E.C., Robertson, R.H.S., 1980. Moisture adsoprtion and specific surface area. Transactions and Journal of the British Ceramic Society 79, 36-40.

Kieffer, J., Karkoulis, D., 2013. PyFAI, a versatile library for azimuthal regrouping. Journal of Physics: Conference Series 425, 202012.

Kim, E., Boulègue, J., 2003. Chemistry of rhenium as an analogue of technetium: Experimental studies of the dissolution of rhenium oxides in aqueous solutions. Radiochimica Acta 91, 211-216.

Kirsch, R., Fellhauer, D., Altmaier, M., Neck, V., Rossberg, A., Fanghänel, T., Charlet, L., Scheinost, A.C., 2011. Oxidation state and local structure of plutonium reacted with magnetite, mackinawite and chukanovite. Environmental Science & Technology 45, 7267–7274.

Kirsch, R., Scheinost, A.C., Rossberg, A., Banerjee, D., Charlet, L., 2008. Reduction of antimony by nano-particulate magnetite and mackinawite. Mineral Mag 72, 185-189.

Kleymenov, E., Van Bokhoven, J.A., David, C., Glatzel, P., Janousch, M., Alonso-Mori, R., Studer, M., Willimann, M., Bergamaschi, A., Henrich, B., Nachtegaal, M., 2011. Five-element Johann-type X-ray emission spectrometer with a single-photon-counting pixel detector. Review of Scientific Instruments 82, 1-7.

Kobayashi, T., Scheinost, A.C., Fellhauer, D., Gaona, X., Altmaier, M., 2013. Redox behavior of Tc(VII)/Tc(IV) under various reducing conditions in 0.1 M NaCl solutions. Radiochimica Acta 101, 323-332.

Krukau, A.V., Vydrov, O.A., Izmaylov, A.F., Scuseria, G.E., 2006. Influence of the exchange screening parameter on the performance of screened hybrid functionals. Journal of Chemical Physics 125.

Kumar, S., Rothe, J., Finck, N., Vitova, T., Dardenne, K., Beck, A., Schild, D., Geckeis, H., 2022. Effect of manganese on the speciation of neptunium(V) on manganese doped magnetites. Colloids and Surfaces A: Physicochemical and Engineering Aspects 635, 128105-128105.

Kvashnina, K.O., Scheinost, A.C., 2016. A Johann-type X-ray emission spectrometer at the Rossendorf beamline. Journal of Synchrotron Radiation 23, 836-841.

Lenell, B.A., Arai, Y., 2017. Perrhenate sorption kinetics in zerovalent iron in high pH and nitrate media. Journal of Hazardous Materials 321, 335-343.

Lenz, M., Hullebusch, E.D.v., Farges, F., Nikitenko, S., Borca, C.N., Grolimund, D., Lens, P.N.L., 2008. Selenium Speciation Assessed by X-Ray Absorption Spectroscopy of Sequentially Extracted Anaerobic Biofilms. Environmental Science & Technology 42, 7587-7593.

Liu, H., Di Valentin, C., 2017. Band Gap in Magnetite above Verwey Temperature Induced by Symmetry Breaking. Journal of Physical Chemistry C 121, 25736-25742.

Liu, H., Di Valentin, C., 2018. Bulk-terminated or reconstructed Fe3O4(001) surface: water makes a difference. Nanoscale 10, 11021-11027.

Liu, H., Di Valentin, C., 2019. Shaping Magnetite Nanoparticles from First Principles. Physical Review Letters 123.

López de Arroyabe Loyo, R., Nikitenko, S.I., Scheinost, A.C., Simonoff, M., 2008. Immobilization of Selenite on Fe3O4 and Fe/Fe3C Ultrasmall Particles. Environmental Science & Technology 42, 2451-2456.

Lukens, W.W., Bucher, J.J., Edelstein, N.M., Shuh, D.K., 2002. Products of pertechnetate radiolysis in highly alkaline solution: Structure of TcO2 center dot xH(2)O. Environmental Science & Technology 36, 1124-1129.

Ma, B., Charlet, L., Fernandez-Martinez, A., Kang, M., Madé, B., 2019. A review of the retention mechanisms of redox-sensitive radionuclides in multi-barrier systems. Applied Geochemistry 100, 414-431.

Maes, N., Glaus, M.A., Rainer, D., Churakov, S., 2023. Final technical report on radionuclide mobility in compacted clay systems and reversibility of sorption. Final version as of 15.12.2023 of deliverable D5.4&D5.6 of the HORIZON 2020 project EURAD. EC Grant agreement no: 847593.

Magneli, A., 1957. Studies on rhenium oxides. Acta Chemica Scandinavica 11, 28-33.

Marsac, R., Banik, N.l., Lützenkirchen, J., Marquardt, C.M., Dardenne, K., Schild, D., Rothe, J., Diascorn, A., Kupcik, T., Schäfer, T., Geckeis, H., 2015. Neptunium redox speciation at the illite surface. Geochimica et Cosmochimica Acta 152, 39-51.

Marshall, T.A., Morris, K., Law, G.T.W., Mosselmans, J.F.W., Bots, P., Parry, S.A., Shaw, S., 2014. Incorporation and Retention of 99-Tc(IV) in Magnetite under High pH Conditions. Environmental Science & Technology 48, 11853-11862.

Matz, W., Schell, N., Bernhard, G., Prokert, F., Reich, T., Claußner, J., Oehme, W., Schlenk, R., Dienel, S., Funke, H., Eichhorn, F., Betzl, M., Pröhl, D., Strauch, U., Hüttig, G., Krug, H., Neumann, W., Brendler, V., Reichel, P., Denecke, M.A., Nitsche, H., 1999. ROBL - A CRG beamline for radiochemistry and materials research at the ESRF. Journal of Synchrotron Radiation 6, 1076-1085.

Mehra, P., Jackson, M.L., 1958. Iron oxide removal form soils and clays by a dithionite -cirrate system buffered with sodium bicarbonate. . Clays and Clay Minerals: Proceedings of the Seventh National Conference on Clays and Clay Minerals (English Edition) . Pergamon Ed.

Missana, T., Alonso, U., García-Gutiérrez, M., 2009a. Experimental study and modelling of selenite sorption onto illite and smectite clays. Journal of Colloid and Interface Science 334, 132-138.

Missana, T., Alonso, U., García-Gutiérrez, M., 2021. Evaluation of component additive modelling approach for europium adsorption on 2:1 clays: Experimental, thermodynamic databases, and models. Chemosphere 272.

Missana, T., Alonso, U., Garcia-Gutierrez, M., Albarran, N., Lopez, T., 2009b. Experimental Study and Modeling of Uranium (VI) Sorption Onto a Spanish Smectite, Scientific Basis for Nuclear Waste Management Xxxii, pp. 561-566.

Missana, T., Alonso, U., Mayordomo, N., García-Gutiérrez, M., 2023. Analysis of Cadmium Retention Mechanisms by a Smectite Clay in the Presence of Carbonates. Toxics 11.

Missana, T., Alonso, U., Scheinost, A.C., Granizo, N., García-Gutiérrez, M., 2009c. Selenite retention by nanocrystalline magnetite: Role of adsorption, reduction and dissolution/co-precipitation processes. Geochimica Et Cosmochimica Acta 73, 6205-6217.

Missana, T., García-Gutiérrez, M., Maffiotte, C., 2003a. Experimental and modeling study of the uranium (VI) sorption on goethite. Journal of Colloid and Interface Science 260, 291-301.

Missana, T., Maffiotte, U., García-Gutiérrez, M., 2003b. Surface reactions kinetics between nanocrystalline magnetite and uranyl. Journal of Colloid and Interface Science 261, 154-160.

Monkhorst, H.J., Pack, J.D., 1976. Special points for Brillouin-zone integrations. Physical Review B 13, 5188-5192.

Montavon, G., Ribet, S., Loni, Y.H., Maia, F., Bailly, C., David, K., Lerouge, C., Madé, B., Robinet, J.C., Grambow, B., 2022. Uranium retention in a Callovo-Oxfordian clay rock formation: From laboratory-based models to in natura conditions. Chemosphere 299, 134307.

Montoya, V., Baeyens, B., Glaus, M.A., Kupcik, T., Marques Fernandes, M., Van Laer, L., Bruggeman, C., Maes, N., Schäfer, T., 2018. Sorption of Sr, Co and Zn on illite: Batch experiments and modelling including Co in-diffusion measurements on compacted samples. Geochimica et Cosmochimica Acta 223, 1-20.

Müller, K., Gröschel, A., Rossberg, A., Bok, F., Franzen, C., Brendler, V., Foerstendorf, H., 2015. In situ spectroscopic identification of neptunium(V) inner-sphere complexes on the hematite-water interface. Environmental Science and Technology 49, 2560-2567.

Myneni, S.C.B., Tokunaga, T.K., Brown, G.E., 1997. Abiotic Selenium Redox Transformations in the Presence of Fe(II,III) Oxides. Science 278, 1106-1109.

Nitsche, H., 1995. Synchrotron X-ray absorption spectroscopy: a new tool for actinide and lanthanide speciation in solids and solution. Journal of Alloys and Compounds 223, 274-279.

Oliveira, A.F., Kuc, A., Heine, T., Abram, U., Scheinost, A.C., 2022. Shedding light on the enigmatic TcO2·xH2O structure with density functional theory and EXAFS spectroscopy. Chemistry - A European Journal 28, e202202235.

Ozdemir, O., Dunlop, D.J., 2010. Hallmarks of maghemitization in low-temperature remanence cycling of partially oxidized magnetite nanoparticles. Journal of Geophysical Research-Solid Earth 115.

Payne, T.E., Brendler, V., Comarmond, M.J., Nebelung, C., 2011. Assessment of surface area normalisation for interpreting distribution coefficients (Kd) for uranium sorption. Journal of Environmental Radioactivity 102, 888-895.

Perdew, J.P., Burke, K., Ernzerhof, M., 1996. Generalized gradient approximation made simple. Physical Review Letters 77, 3865-3868.

Philipsen, P.H.T., 2020. BAND Manual - Amsterdam Modeling Suite 2020, Amsterdam.

Philipsen, P.H.T., vanLenthe, E., Snijders, J.G., Baerends, E.J., 1997. Relativistic calculations on the adsorption of CO on the (111) surfaces of Ni, Pd, and Pt within the zeroth-order regular approximation. Physical Review B 56, 13556-13562.

Poulain, A., Fernandez-Martinez, A., Greneche, J.-M., Prieur, D., Scheinost, A.C., Menguy, N., Bureau,

S., Magnin, V., Findling, N., Drnec, J., Martens, I., Mirolo, M., Charlet, L., 2022. Selenium Nanowire Formation by Reacting Selenate with Magnetite. Environmental Science & Technology 56, 14817-14827.

Qian, Y., Scheinost, A.C., Grangeon, S., Greneche, J.-M., Hoving, A., Bourhis, E., Maubec, N., Churakov, S.V., Fernandes, M.M., 2023. Oxidation State and Structure of Fe in Nontronite: From Oxidizing to Reducing Conditions. ACS Earth and Space Chemistry 7, 1868-1881.

Rabung, T., Pierret, M.C., Bauer, A., Geckeis, H., Bradbury, M.H., Baeyens, B., 2005. Sorption of Eu(III)/Cm(III) on Ca-montmorillonite and Na-illite. Part 1: Batch sorption and time-resolved laser fluorescence spectroscopy experiments. Geochimica et Cosmochimica Acta 69, 5393-5402.

Rasamimanana, S., Lefèvre, G., Dagnelie, R.V.H., 2017. Adsorption of polar organic molecules on sediments: Case-study on Callovian-Oxfordian claystone. Chemosphere 181, 296-303.

Reich, T., Amayri, S., Börner, P.J.B., Drebert, J., Fröhlich, D.R., Grolimund, D., Kaplan, U., 2016. Speciation of neptunium during sorption and diffusion in natural clay. Journal of Physics: Conference Series 712, 1-4.

Reich, T., Bernhard, G., Geipel, G., Funke, H., Hennig, C., Rossberg, A., Matz, W., Schell, N., Nitsche, H., Reich, T., Nitsche, H., 2000. The Rossendorf Beam Line ROBL — a dedicated experimental station for XAFS measurements of actinides and other radionuclides. Radiochimica Acta 88, 633-637.

Reinholdt, M., Miehe-Brendle, J., Delmotte, L., Tuilier, M.H., le Dred, R., Cortes, R., Flank, A.M., 2001. Fluorine route synthesis of montmorillonites containing Mg or Zn and characterization by XRD, thermal analysis, MAS NMR, and EXAFS spectroscopy. European Journal of Inorganic Chemistry, 2831.

Roberts, H.E., Morris, K., Mosselmans, J.F.W., Law, G.T.W., Shaw, S., 2019. Neptunium reactivity during co-precipitation and oxidation of Fe(II)/Fe(III) (oxyhydr)oxides. Geosciences (Switzerland) 9, 1-10.

Rodriguez-Carvajal, J., 2000. FULLPROF-A program for Rietveld, profile matching and integrated intensities refinement of X-ray and/or neutron data. Laboratoire Leon Brillouin: CEA-Saclay, France.

Roshchin, V.E., Roshchin, A.V., 2019. Electron mechanism of reduction processes in blast and ferroalloy furnaces. Cis Iron and Steel Review 17, 14-24.

Rossberg, A., Reich, T., Bernhard, G., 2003. Complexation of uranium(VI) with protocatechuic acid - application of iterative transformation factor analysis to EXAFS spectroscopy. Analytical and bioanalytical chemistry 376, 631-638.

Rovezzi, M., Lapras, C., Manceau, A., Glatzel, P., Verbeni, R., 2017. High energy-resolution x-ray spectroscopy at ultra-high dilution with spherically bent crystal analyzers of 0.5 m radius. Review of Scientific Instruments 88, 13108-13108.

Savoye, S., Schlegel, M.L., Frasca, B., 2021. Mobility of selenium oxyanions in clay-rich media: A combined batch and diffusion experiments and synchrotron-based spectroscopic investigation. Applied Geochemistry 128, 104932.

Schacherl, B., Joseph, C., Beck, A., Lavrova, P., Schnurr, A., Dardenne, K., Geyer, F., Cherkezova-Zheleva, Z., Göttlicher, J., Geckeis, H., Vitova, T., 2023. Np(V) Retention at the Illite du Puy Surface. Environmental Science & Technology 57, 11185-11194.

Schacherl, B., Joseph, C., Lavrova, P., Beck, A., Reitz, C., Pruessmann, T., Fellhauer, D., Lee, J.-Y., Dardenne, K., Rothe, J., Geckeis, H., Vitova, T., 2022a. Paving the way for examination of coupled redox/solid-liquid interface reactions: 1 ppm Np adsorbed on clay studied by Np M5-edge HR-XANES spectroscopy. Analytica Chimica Acta 1202, 339636.

Schacherl, B., Prüssmann, T., Dardenne, K., Hardock, K., Krepper, V., Rothe, J., Vitova, T., Geckeis, H., 2022b. Implementation of cryogenic tender X-ray HR-XANES spectroscopy at the ACT station of the

CAT-ACT beamline at the KIT Light Source. Journal of Synchrotron Radiation 29, 80-88.

Scheinost, A.C., Charlet, L., 2008. Selenite reduction by mackinawite, magnetite and siderite: XAS characterization of nanosized redox products. Environmental science & technology 42, 1984-1989.

Scheinost, A.C., Claussner, J., Exner, J., Feig, M., Findeisen, S., Hennig, C., Kvashnina, K.O., Naudet, D., Prieur, D., Rossberg, A., Schmidt, M., Qiu, C., Colomp, P., Cohen, C., Dettona, E., Dyadkin, V., Stumpf, T., 2021. ROBL-II at ESRF: A synchrotron toolbox for actinide research. Journal of Synchrotron Radiation 28, 333-349.

Scheinost, A.C., Kirsch, R., Banerjee, D., Fernandez-Martinez, A., Zaenker, H., Funke, H., Charlet, L., 2008. X-ray absorption and photoelectron spectroscopy investigation of selenite reduction by FeII-bearing minerals. Journal of Contaminant Hydrology 102, 228-245.

Scheinost, A.C., Steudtner, R., Hübner, R., Weiss, S., Bok, F., 2016. Neptunium(V) retention by siderite under anoxic conditions: Precipitation of NpO2-like nanoparticles and of Np(IV) pentacarbonate. Environmental Science and Technology 50, 10413-10420.

Schweitzer, G.K., Pesterfield, L.L., 2010. The Aqueous Chemistry of the Elements. American Chemical Society.

Shang, C., Coreau, N., Macé, N., Descostes, M., Reiller, P.E., 2023. Implications of recently derived thermodynamic data and specific ionic interaction theory parameters for (Mg/Ca)nUO2(CO3)3(4-2n)-complexes on the predominance of the Mg2+–Ca2+–UO22+–OH−–CO32− systems, and application to natural and legacy-mine waters. Science of The Total Environment 858, 159927.

Smith, F.N., Um, W., Taylor, C.D., Kim, D.-S., Schweiger, M.J., Kruger, A.A., 2016. Computational Investigation of Technetium(IV) Incorporation into Inverse Spinels: Magnetite (Fe3O4) and Trevorite (NiFe2O4). Environmental Science & Technology 50, 5216-5224.

Smith, K.F., Bryan, N.D., Law, G.T.W., Hibberd, R., Shaw, S., Livens, F.R., Parry, S.A., Mosselmans, J.F.W., Morris, K., 2018. Np(V) sorption and solubility in high pH calcite systems. Chemical Geology 493, 396-404.

Soderholm, L., Antonio, M.R., Williams, C., Wasserman, S.R., 1999. XANES spectroelectrochemistry: A new method for determining formal potentials. Analytical Chemistry 71, 4622-4628.

Sokaras, D., Weng, T.C., Nordlund, D., Alonso-Mori, R., Velikov, P., Wenger, D., Garachtchenko, A., George, M., Borzenets, V., Johnson, B., Rabedeau, T., Bergmann, U., 2013. A seven-crystal Johann-type hard x-ray spectrometer at the Stanford Synchrotron Radiation Lightsource. Review of Scientific Instruments 84, 53102-53102.

Soltermann, D., Fernandes, M.M., Baeyens, B., Dähn, R., Miehé-Brendlé, J., Wehrli, B., Bradbury, M.H., 2013. Fe(II) sorption on a synthetic montmorillonite. A combined macroscopic and spectroscopic study. Environmental Science & Technology 47, 6978-6986.

Steininger, R., Göttlicher, J., Mangold, S., Veselska, V., 2018. Irradiation effect studies on a Cr(VI) model system.

Stojanovic, N., Stanford Synchrotron Radiation Lightsource: Experimental Station 4-1.

Stookey, L.L., 1970. Ferrozine-a new spectrophotometric reagent for iron. Analytical Chemistry 42, 779-&.

Stucki, J.W., Golden, D.C., Roth, C.B., 1984. Preparation and handling of dithionite-reduced smectite suspensions. Clays Clay Miner. 32, 191-197.

Tarafder, P.K., Thakur, R., 2013. An Optimised 1,10-Phenanthroline Method for the Determination of Ferrous and Ferric Oxides in Silicate Rocks, Soils and Minerals. Geostandards and Geoanalytical Research 37, 155-168.

te Velde, G., Bickelhaupt, F.M., Baerends, E.J., Guerra, C.F., Van Gisbergen, S.J.A., Snijders, J.G., Ziegler, T., 2001. Chemistry with ADF. Journal of Computational Chemistry 22, 931-967.

Teillet, J.V., F. MOSFIT program; Université Le Mans: Le Mans, France.

Tkatchenko, A., Scheffler, M., 2009. Accurate Molecular Van Der Waals Interactions from Ground-State Electron Density and Free-Atom Reference Data. Physical Review Letters 102.

Van Loon, L.R., Soler, J.M., Bradbury, M.H., 2003. Diffusion of HTO, 36Cl and 125I in Opalinus Clay samples from Mont Terri: Effect of confining pressure. Journal of Contaminant Hydrology 61, 73-83.

Van Orman, J.A., Crispin, K.L., 2010. Diffusion in Oxides, in: Zhang, Y.X., Cherniak, D.J. (Eds.), Diffusion in Minerals and Melts, pp. 757-825.

van Schooneveld, M.M., DeBeer, S., 2015. A close look at dose: Toward L-edge XAS spectral uniformity, dose quantification and prediction of metal ion photoreduction. Journal of Electron Spectroscopy and Related Phenomena 198, 31-56.

Virtanen, S., Bok, F., Ikeda-Ohno, A., Rossberg, A., Lützenkirchen, J., Rabung, T., Lehto, J., Huittinen, N., 2016. The specific sorption of Np(V) on the corundum (α-Al2O3) surface in the presence of trivalent lanthanides Eu(III) and Gd(III): A batch sorption and XAS study. J Colloid Interface Sci 483, 334-342.

Vitova, T., Faizova, R., Amaro-Estrada, J.I., Maron, L., Pruessmann, T., Neill, T., Beck, A., Schacherl, B., Tirani, F.F., Mazzanti, M., 2022. The mechanism of Fe induced bond stability of uranyl(V). Chemical Science 13, 11038-11047.

Vitova, T., Green, J.C., Denning, R.G., Löble, M., Kvashnina, K., Kas, J.J., Jorissen, K., Rehr, J.J., Malcherek, T., Denecke, M.A., 2015. Polarization dependent high energy-resolution X-ray absorption study of dicesium uranyl tetrachloride. Inorganic Chemistry 54, 174-182.

Vitova, T., Pidchenko, I., Biswas, S., Beridze, G., Dunne, P.W., Schild, D., Wang, Z., Kowalski, P.M., Baker, R.J., 2018. Dehydration of the uranyl peroxide studtite, [UO2(η2-O2)(H2O)2·2H2O, affords a drastic change in the electronic structure: A combined X-ray spectroscopic and theoretical analysis. Inorganic Chemistry 57, 1735-1743.

Vitova, T., Pidchenko, I., Fellhauer, D., Bagus, P.S., Joly, Y., Prüßmann, T., Bahl, S., Gonzalez-Robles, E., Rothe, J., Altmaier, M., Denecke, M.A., Geckeis, H., Pruessmann, T., Bahl, S., Gonzalez-Robles, E., Rothe, J., Altmaier, M., Denecke, M.A., Geckeis, H., 2017. The role of the 5f valence orbitals of early actinides in chemical bonding. Nature Communications 8, 16053-16053.

Vitova, T., Pidchenko, I., Schild, D., Prüßmann, T., Montoya, V., Fellhauer, D., Gaona, X., Bohnert, E., Rothe, J., Baker, R.J., Geckeis, H., 2020. Competitive reaction of neptunium(V) and uranium(VI) in potassium–sodium carbonate-rich aqueous media: Speciation study with a focus on high-resolution X-ray spectroscopy. Inorganic Chemistry 59, 8-22.

Wang, G.H., Olszta, M.J., Saslow, S.A., Kim, D.S., Bowden, M.E., Um, W., Wang, J., Kruger, A.A., 2021. A Focused Ion Beam-Scanning Transmission Electron Microscopy with Energy-Dispersive X-ray Spectroscopy Study on Technetium Incorporation within Iron Oxides through Fe(OH)(2)(s) Mineral Transformation. Acs Earth and Space Chemistry 5, 525-534.

Wilk, P.A., Shaughnessy, D.A., Wilson, R.E., Nitsche, H., 2005. Interfacial interactions between Np(V) and manganese oxide minerals manganite and hausmannite. Environ Sci Technol 39, 2608-2615.

Williams, A.G.B., Scherer, M.M., 2004. Spectroscopic evidence for Fe(II)-Fe(III) electron transfer at the iron oxide-water interface. Environmental Science & Technology 38, 4782-4790.

Xia, X., Idemitsu, K., Arima, T., Inagaki, Y., Ishidera, T., Kurosawa, S., Iijima, K., Sato, H., 2005. Corrosion of carbon steel in compacted bentonite and its effect on neptunium diffusion under reducing condition. Applied Clay Science 28, 89-100.

Yalçıntaş, E., Gaona, X., Scheinost, A.C., Kobayashi, T., Altmaier, M., Geckeis, H., 2015. Redox chemistry of Tc(VII)/Tc(IV) in dilute to concentrated NaCl and $MgCl_2$ solutions. Radiochimica Acta 103, 57-72.

Yalçıntaş, E., Scheinost, A.C., Gaona, X., Altmaier, M., 2016. Systematic XAS study on the reduction and uptake of Tc by magnetite and mackinawite. Dalton Transactions 45, 17874-17885.

Yang, C., Powell, B.A., Zhang, S., Rao, L., Yang, C., Zhang, S., Rao, L., 2015. Surface complexation modeling of neptunium(V) sorption to lepidocrocite (γ-FeOOH). Radiochimica Acta 103, 707-717.